Experimental Evaluation and Modeling of Photocatalytic Oxidation Air Cleaners

Lexuan Zhong

A Thesis

in

The Department

of

Building, Civil and Environmental Engineering

Presented in Partial Fulfillment of the Requirements

For the Degree of Doctor of Philosophy at

Concordia University

Montreal, Quebec, Canada

January 2013

CONCORDIA UNIVERSITY
SCHOOL OF GRADUATE STUDIES

This is to certify that the Ph.D. thesis prepared

By: **Lexuan Zhong**

Entitled: **Experimental Evaluation and Modeling of Photocatalytic Oxidation Air Cleaners**

and submitted in partial fulfillment of the requirements for the degree of

Doctor of Philosophy

complies with the regulations of this University and meets the accepted standards with respect to originality and quality.

Signed by the final examining committee:

_____ Dr. I. Hassan (Chair)

_____ Dr. Y. Zhang (External Examiner)

_____ Dr. G. Vatistas (External to Program)

_____ Dr. C. Mulligan (Examiner)

_____ Dr. Z. Chen (Examiner)

_____ Dr. F. Haghighat (Thesis Supervisor)

Approved by_____
Chair of Department or Graduate Program Director

_____2013_____
Dean, Faculty of Engineering and Computer Science

ABSTRACT

Experimental Evaluation and Modeling of Photocatalytic Oxidation Air Cleaners

Lexuan Zhong, Ph.D.
Concordia University, 2013

Heterogeneous ultraviolet photocatalytic oxidation (UV-PCO), as a promising advanced oxidation technology, has been suggested as an alternative and energy efficient method to improve indoor air quality (IAQ) through the photocatalytic degradation of indoor air pollutants. However, the complicated PCO reaction mechanisms and unexpected intermediates still need to be further explored in order for this technology to be successfully applied in mechanically ventilated buildings.

Two main objectives of this study include the development of methodologies to evaluate the performance of PCO systems and the development of a reliable mathematical model to fully simulate the performance of these systems.

A pilot four-parallel duct system was set-up to equitably and thoroughly evaluate the performance of UV-PCO air cleaners under the conditions relevant to the actual applications for a wide range of indoor air pollutants. This study investigated the UV-PCO removal efficiency of two types of air filters (fiberglass fibers coated with TiO_2 (TiO_2/FGFs) and carbon cloth fibers loaded with TiO_2 (TiO_2/CCFs)) under ultraviolet C (UVC) and vacuum ultraviolet (VUV) illumination. A systematic parametric evaluation of the effects of various kinetic parameters, such as types of pollutants, inlet concentration, airflow rate, light intensity, and relative humidity that

influence the PCO performance, was conducted. In addition, gas-phase ozonation with a variety of chemical compounds was first examined when ozone was produced by VUV. Moreover, the formation of by-products generated from incomplete conversion was investigated to evaluate its impact on IAQ.

A time-dependent model was proposed for predicting the performance of an in-duct PCO air cleaner under the conditions relevant to the actual applications. A comprehensive model was developed by integrating light scattering model, reaction kinetic model, mass balance as well as optional ozonation model. The UV-PCO model and the UV-PCO ozonation integrated model were validated with experimental results; there was a good agreement between the model prediction and the experiment result. The relative rate-limiting process between physical interactions and photochemical interactions was fully investigated through simulation analysis. Depending on the physical properties of the catalyst, reactor geometries, operation conditions, as well as environmental conditions, the photochemical reaction occurring on the fixed active sites at the catalyst surface is the dominating process for this PCO system.

ACKNOWLEDGEMENTS

First of all, I would like to express my sincere gratitude to my supervisor, Dr. Fariborz Haghighat, for his valuable guidance and continuous support throughout my PhD study and research. From him, I have learned not only the professional knowledge but also the strict attitude towards research and life. I benefit greatly from his scientific attitude, creative thinking, as well as hard working, which are indispensable for my future career development and will benefit me for my whole life.

Besides my supervisor, I would like to thank the rest of my thesis committee: Dr. G. Vatistas, Dr. C. Mulligan, Dr. Z. Chen, and Dr. Y. Zhang for their encouragement, insightful comments, and valuable suggestions to my research and dissertation.

I would like to express my gratitude to Circul-Aire, Inc. for providing the support for the design and construction of the experimental set-up which provided a unique and excellent research facility. My sincere thanks also go to Dr. Chang-Seo Lee, for her careful mentoring, fruitful discussions, and precious comments on writing of papers. Electron microscopy research group of McGill University is acknowledged for the help of SEM analysis. I also thank Dr. Raymond Le Van Mao and Dr. Hai Tao Yan for technical assistance of BET analysis.

I gratefully acknowledge the generous financial supports from the Natural Science and Engineering Research Council Canada (NSERC) Postgraduate Scholarship (PGS), the Concordia Merit Scholarship, the Concordia University Graduate Fellowship, and ASHRAE Grant-in-Aid Scholarship.

Many thanks go to my labmates in Energy and Environment Research Group, especially Donya Farhanian, Mitra Bahri, and Alireza Aghighi, for their warm assistances and encouragements. Special acknowledgements go to Mr. Joseph Hrib, Mr. Luc Demers and Ms. Claire Therrien for their technical help and safety concerns. I also thank my other colleagues in the same research group: Dr. Zhun Yu, Dr. Omid Ashrafi, Arash Bastani, Arash Soleimani Karimabad, Ali Khazraei Vizhemehr, and Mohammmad Reza Nabavi Tabatabay, for all the fun we had during these years.

Last but not the least, I would like to express utmost gratitude to my family: my parents, my husband, my daughter and an unborn baby for their endless love and spiritual support throughout my life. Special appreciations go to my mother who is taking a responsibility of a mother instead of me to take care of my Sophia these years, and I owe her too much. I love you all forever!

TABLE OF CONTENTS

LIST OF FIGURES

LIST OF TABLES

LIST OF ABBREVIATIONS

ASHRAE	American society of heating, refrigerating and air conditioning engineers
BET	"BET" consists of the first initials of Stephen Brunauer, Paul Hugh Emmett, and Edward Teller
BL	boundary layer
BRI	building related illness
BTEX	benzene, toluene, ethylbenzene, and xylenes
CB	conduction band
cfm	cubic feet per minute
CO_2	carbon dioxide
2,4-DNPH	2,4-dinitrophenylhydrazine
FTIR	Fourier transform infrared spectroscopy
GAC	granular activated carbon
GC/FID	gas chromatograph/ flame ionization detector
GC/MS	gas chromatograph/mass spectrometer
HEPA	high efficiency particular air
HPLC	high performance liquid chromatograph
HVAC	heating, ventilating and air-conditioning
L-H model	Langmuir-Hinshelwood model
MEK	methyl ethyl ketone (2-butanone)

MCS	multiple chemical sensitivity
NO	nitric oxide
IAQ	indoor air quality
O_3	ozone
PCO	photocatalytic oxidation
ppb	parts per billion
ppm	parts per million
PTFE	polytetrafluoroethylene
SBS	sick building syndrome
SEM	scanning electron microscopy
SO_2	sulfur dioxide
TiO_2	titanium dioxide
UVA	ultraviolet A radiation
UVB	ultraviolet B radiation
UVC	ultraviolet C radiation
UV-PCO	ultraviolet – photocatalytic oxidation
VB	valence band
VOCs	volatile organic compounds
VUV	vacuum ultraviolet

LIST OF SYMBOLS

English Symbols	Description
a	geometric surface area per unit reactor volume (m^{-1})
A	area (m^2)
A_0	plane area of UV light (m^2)
C	concentration (mg/m^3)
D	diffusion coefficient (m^2/s)
D_e	effective diffusion coefficient (m^2/s)
D_m	molecular diffusion coefficient (m^2/s)
E_a	activation energy (kJ/mol)
F	view factor
I	UV irradiance (mW/cm^2)
k_1	adsorption constant
k_{-1}	desorption constant
k_r	global kinetic coefficient of the oxidation reaction (s^{-1})
K	Langmuir's absorption parameter (m^3/mg)
k_0	synthetic kinetic rate coefficient (s^{-1})
k_g	inter-phase mass transfer coefficient (m/s)
L_f	TiO_2 film thickness (μm)
P	pressure (atm)
Q	volumetric airflow rate (m^3/s)

Q’	rate of heat generation of adsorption (kJ/mol)
r	PCO reaction rate (mol/m^3s)
R	gas constant (J/k•mol)
s	length of the connecting line (m)
T	temperature (K)
t	time (min)
u	velocity (m/s)
W	length size of the cross section of the square duct (m)

Greek letters	**Description**
α	proportionality constant
β	reaction order with respect to UV light applied
ξ	stoichiometric coefficient of the compound in the reaction
η	PCO efficiency (%)
ρ	wall reflectivity (%)
Ω	angle or collision integral
λ	wavelength (nm)
ε	porosity of the catalyst
τ	tortuosity of the catalyst
$\bar{\sigma}$	effectiveness factor of the photocatalyst
υ	air viscosity (m^2/s)

μ	UV irradiance extinction coefficient

Dimensionless parameters	**Description**
X,Y,Z	axial distance x/W, y/W, z/W
NTU_m	the number of mass transfer units
Φ	UV irradiance
Re	Reynolds number, $Re = uD/\varepsilon\upsilon$
Sc	Schmidt number, $Sc = \upsilon/D_m$
Sh	Sherwood number, $Sh = k_g D/D_m$

Subscripts	**Description**
ad	adjacent walls
ads	adsorption
B	bulk
CO_2	carbon dioxide
des	desorption
down	downstream
f	filter
H_2O	humidity
i	species

in	inlet
j	intermediates converted from i
op	opposing wall
out	outlet
S	sorbed-phase
t	time
up	upstream
w	wall
x,y,z	vector
–	mean
0	initial
1	duct wall at the right side of UV light
2	duct wall at the left side of UV light

1. INTRODUCTION

1.1 Indoor Air Quality Problems

During the past three decades, indoor air quality (IAQ) has become an important issue of global concern. Sick Building Syndrome (SBS), Building Related Illness (BRI) and Multiple Chemical Sensitivity (MCS) are frequently appearing on research reports (Hedge et al., 1986; Hedge et al., 1989; Hansen 1995; Sundell 1996; Tillman et al., 2006; Gupta et al., 2007). There are three main reasons for why this problem occurs. First, due to energy-saving requirements since the energy crisis of the seventies, the building ventilation rate has generally declined, and air-tightness has substantially increased (Becker 1979; Nq 1992), thereby causing a serious problem for indoor air quality. Second, the man-made materials (including decoration materials and furniture) have been widely used, releasing of a large number of chemical pollutants, mainly volatile and semi-volatile organic compounds (Huang and Haghighat, 2003; Yang et al., 2005). Moreover, since most people spend more than 80% of their life indoors (Books et al., 1991), the concentration of chemical pollutants becomes the dominant contributor to personal exposure. Third, with the development of global economy, the living standard, as well as the requirements for comfortable living and working environment, has generally been greatly improving, resulting in a growing conflict between the people’s tendency to over-decorate, thus contributing to the pollution of indoor air, and the people's requirements for improving indoor air

quality. In this manner, indoor air quality is closely linked with people's health and life quality.

1.2 Indoor Air Control Strategies in HVAC Systems

1.2.1 Dilution Ventilation Control

The design of building Heating, Ventilating and Air-Conditioning (HVAC) systems must take into account health and comfort of the occupants, as well as the energy consumption and the environment. The system needs to protect occupants against chemical contaminants from numerous internal sources - office equipment, furniture, building materials, appliances, as well as bio-contaminants (Haghighat and De Bellis, 1998; Wang et al., 2009). To reduce exposure to internal contaminants, outdoor air is brought in to dilute the indoor air. The quantity of the outdoor air brought into the building can have a direct negative effect on the energy cost of ventilation. There is a cost to heat, cool, humidify or dehumidify the outdoor air, depending on the location and season. This leads to a balancing act between IAQ and ventilation costs.

The strategy of diluting indoor contaminants with outdoor air assumes that the outdoor air is clean; this is not the case in many large cities or near industrial complexes. Most ventilation systems have a form of particulate filtration, but this usually is intended more to protect heating and cooling equipment from fouling than to protect the occupants. At the same time, this particulate filtration system is not effective for gaseous contaminants removal. The attempt is to design an efficient air

purification system to be able to respond to the threat of chemical release, either intentional, as in a terrorist attack, or unintentional, as in an industrial accident.

1.2.2 Filtration and Purification Control

The needs to provide a healthy, safe and comfortable indoor environment and to reduce building energy consumption have all increased the interest in systems that filter gaseous contaminants from the air. Today, the filters commonly used for air cleaning are designed to capture the various size particles, while being generally ineffective in the removal of gaseous or vapour phase pollutants and certain micro-organisms. Some air cleaners which are designed to remove chemical agents act on the basis of the adsorption phenomenon. For this purpose, granular activated carbons or zeolites are commonly used, since they have a high capacity for pollutant adsorption due to a highly developed porous structure and a huge specific surface area (Haghighat et al., 2008; Bastani et al., 2010).

Another promising technology which has great potential in this respect is the photocatalytic oxidation (PCO) (Hager and Bauer, 1999; Lin and Li, 2003; Ginestet et al., 2005; Zhong et al., 2010). PCO technique for air purification is usually implemented under room temperature and pressure, and may be more energy-saving than other conventional techniques. This technology can play a significant role in reducing building energy consumption and indoor air contaminant level, improving the well-being of occupants. PCO uses a semiconductor, most often titanium dioxide (TiO_2), which is inexpensive and is capable of effectively oxidizing most organic

compounds. During the PCO process, the absorption of light in the near ultraviolet (UV) range results in the electron transition from the valence band to the conduction band. The subsequent generation of positive holes and their interactions with water vapor leads to the formation of hydroxyl radicals. These act as powerful oxidizing agents and can be used to oxidize atmospheric pollutants such as various oxides of nitrogen (NO_x) and the volatile organic compounds (VOCs).

Most PCO technologies can be potentially implemented in buildings as in-duct systems, operating either on the return air or the supply air, or as stand-alone (portable) air cleaners. For such systems, UV lamps are used to provide high energy radiation and thus promote electron transition within the catalyst. In addition, if the system is emitting radiation in the range of Ultraviolet C (UVC), *i.e.* in the wavelength band from 200 to 280 nm, and more specifically around 254 nm, where the radiation becomes germicidal, Ultraviolet–photocatalytic oxidation (UV-PCO) could contribute to the removal and deactivation of microorganisms (Wang et al., 2009). Finally, vacuum ultraviolet (VUV) lights can be used to generate a narrow-band UV light (185 nm) which may initiate ozonation reactions (air-phase), leading to the decomposition of VOCs with unsaturated carbon-carbon bonds.

1.3 Research Objectives

On the one hand, industrial applications of UV-PCO have been studied for years, and considerable knowledge has been developed. On the other hand, indoor air applications are putting into play much more complex operating conditions than in

industrial applications: contaminants are never isolated but are present as complex mixtures in the air; their concentrations in the incoming air, as well as possibly their temperature and humidity, will vary over time. UV-PCO technology is still at an experimental stage for such applications. In the past two decades, majority of investigations have been conducted in bench-scale PCO reactors and only on few compounds with high concentrations. However, no systematic studies have been carried out regarding its comprehensive performance under the conditions relevant to the real applications. Furthermore, although a number of such devices are available on the market, many questions remain about the parameters influencing their efficiency and the formation of harmful by-products.

In the quest for more successful commercial applications of UV-PCO technology in buildings, more attention is being brought to the modeling and simulation of the reactors in order to obtain a more comprehensive and systematic understanding of the UV-PCO system. In the past two decades, although different prediction models (Obee, 1996; Zhang et al., 2003; Yang et al., 2005; Chen et al., 2005) for PCO reactors have been developed, most of them are not intended for mechanical ventilation applications and cannot correctly simulate the behavior of a PCO reactor under the conditions encountered in buildings (Vincent et al., 2009; Puma et al., 2009).

The aim of this study is to develop methodologies to evaluate the performance of the PCO system for the IAQ applications. Since there are many factors influencing the performance of PCO, it is necessary to further investigate the effect of certain parameters on the PCO efficiency. A systematic parametric study helps us understand

the impacts of different parameters and their interactions on the PCO performance.

The ultimate goal of this work is to develop and validate a comprehensive and reliable mathematical model that can be used to simulate the performance of the UV-PCO devices for indoor applications. The development of a reliable and validated model can facilitate the widespread application of UV-PCO for indoor air treatment and purification in mechanically ventilated buildings.

1.4 Methodology of This Study

The analysis methodology adopted in this study is depicted in Figure 1-1 and consists of the following steps:

- **Objectives**: Identifying the problems and specifying the objectives of the research project.
- **Literature review**: Reviewing of the state of the art in PCO technique and finding out all the potential factors affecting the PCO efficiency.
- **Design PCO system**: Designing a versatile UV-PCO system operated under the conditions relevant to the actual applications.
- **Experimental setup**: Constructing a pilot test system, choosing the appropriate measuring instruments, and developing a scientific testing method.
- **PCO tests**: Carrying out extensive UV-PCO tests under different operational and experimental conditions.
- **Data collection**: Utilizing Microsoft Excel to manage and analyze experimental data.

In addition, another parallel work in our proposed PCO project is carried out and illustrated as shown in Figure 1-1:

- **Model development**: Setting up of an initial model based on literature review and preliminary test results, designing additional experiments to determine the values of PCO model parameters, and then gradually improving the model based on the experimental data and basic adsorption/photocatalysis mechanisms involved.
- **Implement**: Using Matlab to numerically solve the equations using a finite difference scheme.
- **Verification and validation**: Validating the model to access its adequacy. If there is a large deviation between the results predicted by the PCO model with the experimental data, the proposed model should be further revised so that it can correctly predict the performance of the PCO air cleaners.
- **Parametric study**: The validated model is parametrically studied to understand the impacts of different parameters and their interactions on the PCO behavior.

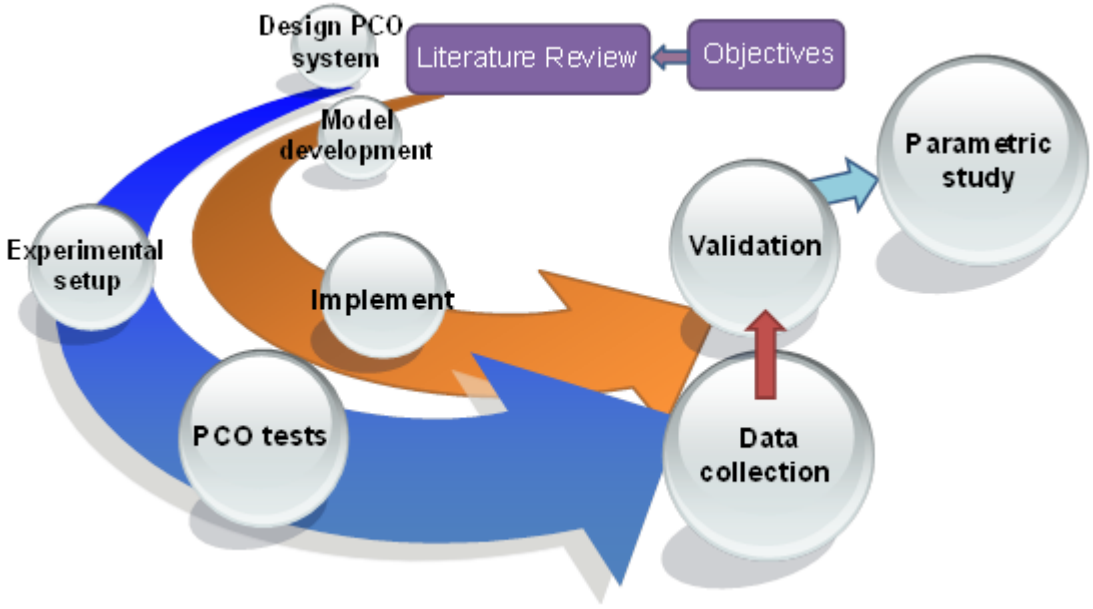

Figure 1-1 The methodology of this study

2. LITERATURE REVIEW

2.1 Fundamentals of PCO

2.1.1 Reaction Mechanism

The PCO process may be divided into seven elemental mass transfer processes (Hougen and Watson, 1947) occurring in series, namely:

1) Advection (VOCs and precursor species are carried by airflows),

2) Mass transfer of the reactants from the main flow to the exterior surface of the catalyst particle,

3) Molecular diffusion and/or Knudsen flow of the reactants from the exterior surface of the catalyst particle into the interior pore structure,

4) Adsorption onto the interior catalyst surface,

5) Photochemical reaction at the catalyst surface,

6) Desorption of the reaction product(s) from the surface of the catalyst, and

7) Mass transfer of the products from the interior catalyst pores to the gross external surface of the catalyst by ordinary molecular diffusion and/or Knudsen diffusion, and finally external diffusion to the main flow (Figure 2-1).

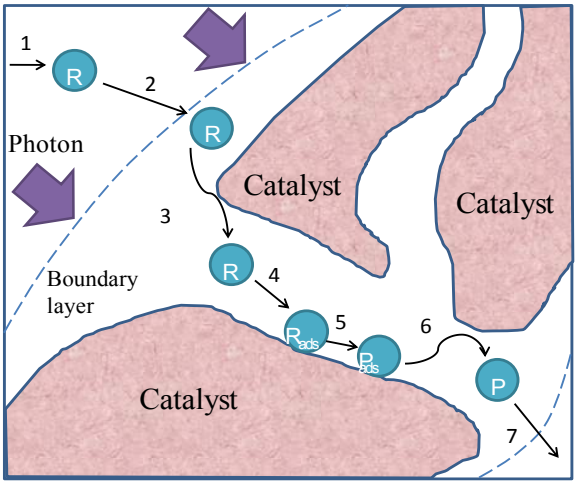

Figure 2-1 Elemental mass transfer processes involved in the photocatalysis of VOCs with a non-porous catalyst

The reaction mechanism itself (step 5) can be explained using Figure 2-2 which illustrates the chemical mechanism at the catalyst surface. When the semiconductor is illuminated by photons whose energy hν is equal or greater than the band-gap energy E_g (Figure 2-2), the semiconductor absorbs the photons. This process stimulates the electron transfer from the valence band (VB) to the conduction band (CB) and creates positive holes in the VB. These highly reactive electron (e^-_{CB})-hole (h^+_{VB}) pairs can either recombine to produce heat or be used to reduce or oxidize species at the semiconductor surface. The positive holes react with the adsorbed water to form highly reactive hydroxyl radicals (·OH), which can initiate the oxidation of the adsorbed organic compounds. Under optimal reaction conditions, organic pollutants can be completely oxidized to form carbon dioxide, water, etc., as the final products. Eqs. (2-1) to (2-9) describe a possible reaction pathway using titanium dioxide (TiO_2) as the semiconductor.

$$TiO_2 + h\nu \rightarrow h^+_{VB} + e^-_{CB} \qquad [2\text{-}1]$$

$$H_2O_{(ads)} \rightarrow OH^- + H^+ \quad [2\text{-}2]$$

$$OH^- + h^+_{VB} \rightarrow \cdot OH \quad [2\text{-}3]$$

$$O_2 + e^-_{CB} \rightarrow O^-_2 \quad [2\text{-}4]$$

$$O^-_2 + H_2O \rightarrow \cdot OOH + OH^- \quad [2\text{-}5]$$

$$2 \cdot OOH \rightarrow O_2 + H_2O_2 \quad [2\text{-}6]$$

$$\cdot OOH + H_2O + e^-_{CB} \rightarrow H_2O_2 + OH^- \quad [2\text{-}7]$$

$$H_2O_2 + e^-_{CB} \rightarrow \cdot OH + OH^- \quad [2\text{-}8]$$

$$\cdot OH + \text{Pollutant} + O_2 \rightarrow \text{Products } (CO_2, H_2O, \text{etc.}) \quad [2\text{-}9]$$

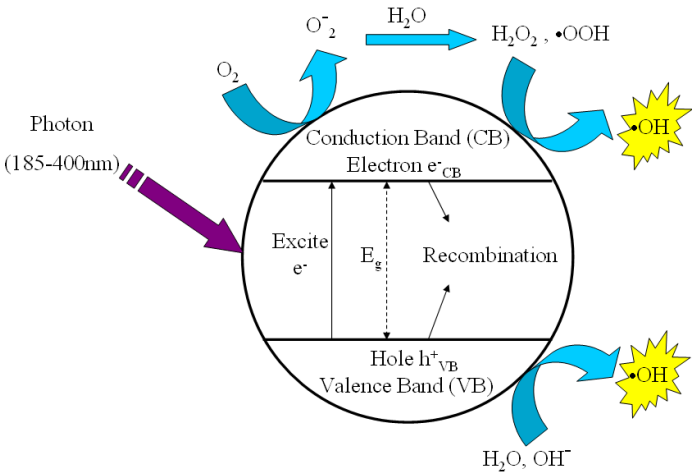

Figure 2-2 Primary mechanism of photocatalytic reaction

Understanding the fundamentals of UV-PCO is of central importance for interpreting the experimental data, improving the knowledge on the parameters influencing the PCO efficiency, and finally optimizing systems for building applications. To achieve this, one key point is to consider that the kinetics of each of the above-mentioned elemental phenomenon is determined by many factors, and one factor may have influence on several processes. For instance, the airflow rate not only determines the amounts of contaminants and precursors (H_2O, $\cdot OH$) incoming to the

system, but also the boundary layer mass transfer coefficients and, thus, the diffusion kinetics of both reagents and products. Chemical kinetics at the catalyst surface is influenced by the UV irradiance, which determines the rate of electron transfer, but also temperature, which determines the speed of the subsequent surface reactions. The rate limiting process of the whole VOC mineralization process determines the efficiency and the quantum yield of the by-products. The problem is that this rate limiting process may be different depending on the physical properties of the catalyst, the reactor geometry, the operation of the system, and the environmental conditions. Now the question is what the PCO kinetics is in specified conditions. The question may be answered by modeling. As a result, Section 2.2 presents a critical review of the various modeling approaches.

2.1.2 Semiconductor Photocatalyst

During past decades, many semiconductors have been examined as candidate photocatalysts, such as ZnO, ZrO_2, SnO_2, CeO_2, WO_3, Fe_2O_3, Al_2O_3 and TiO_2 (Herrmann et al., 1981; Casado et al., 1990; Luo and Ollis, 1996; d'Hennezel et al., 1998). Among these photocatalysts, nano-TiO_2, as the most important oxide semiconductor, has been extensively studied and developed due to the appropriate physical and chemical properties, such as catalytic activity, photocatalytic activity, high sensitivity for the gases, as well as dielectric characteristics. Moreover, high chemical stability, optical stability and low cost make it a widely used photocatalyst in the industry.

These properties of TiO_2 largely depend on its crystal structure, phase and particle size. The two industrially useful crystalline forms of TiO_2 are anatase and rutile; generally, anatase particles perform better than the other (Zeltner and Tompkins, 2005). At present, various techniques of synthesis of nanocrystalline TiO_2 have been developed; these include the sol - gel method, the hydrothermal method, as well as the gas condensation method.

Due to the UV light region accounting for only 3-5% of the solar light, considerable work has been carried out toward modifying TiO_2 and testing the other semiconductors to improve the overlap of the absorption spectrum of the photocatalyst with the solar spectrum (Kirchnerova et al., 2005; Ai et al., 2009; Kowalska et al., 2008; Dawson and Kamat, 2001; Cozzoli et al., 2004). Technically, solar applications are feasible when additional metal ions, such as Pt, Au, and Ag, are deposited onto the TiO_2 lattice to enhance catalytic activity (Kowalska et al., 2008; Dawson and Kamat, 2001; Cozzoli et al., 2004). Another strategy employed to utilize visible light is to develop stable single-phase photocatalysts. For example, Ai et al. (2009) developed nonaqueous sol-gel synthesized of BiOBr microspheres, and their results revealed that this novel photocatalyst exhibited higher photocatalytic efficiency than that of TiO_2 on degradation of NO under the UV-visible light irradiation and showed a high photocatalytic activity even under the visible light.

2.1.3 Light Source

Commercial UV lamps emit light in the range of 185 nm and 400 nm, which

covers vacuum UV, UVC, Ultraviolet B radiation (UVB) and UVA. Table 2-1 lists the common UV lamps and shows that the shorter the wavelength, the higher the energy. However, this does not necessarily mean that the shorter wavelengths give a higher performance: Zhang et al. (2003a) found that 365 nm is more efficient than 254 nm when TiO_2/O_3/UV is used to degrade toluene.

Table 2-1 Types of UV lamps in the literature

Type	Nominal Power (W)	λ (nm)	Irradiation (mW/cm^2)	Ref.
Black-light lamp	---	352	5.6	Obee and Hay, 1997
Hg lamp	125	300-400 (peak:365)	---	d'Hennezel et al., 1998
Hg-Xe lamp	---	365	1.0	Noguchi et al., 1998
High pressure mercury lamp	400	Peak: 365	---	Jing et al., 2004
Germicidal lamp	8	200-280 (peak:254)	2.58	Li et al., 2006
Black-light lamp	8	310-400 (peak:365)	1.28	
Fluorescent UV lamp	30	267	---	Liu et al., 2006
Fluorescent UV lamp	18	350	---	Vorontsov, 2007
Hg lamp	12	254.7 and 184.9	---	Boulamanti et al., 2008
Xenon lamp	1500	≤340	---	Bekbolet et al., 2009

The location of the lamp affects greatly the PCO efficiency in the duct system. The mounting location is a place that allows enough space for the lamp to be installed and to be replaced easily. In order for the UV-PCO system to be effective, the UV purifier must be strategically oriented to maximize exposure. The lamp may be

mounted vertically or horizontally within the HVAC system. When the ultraviolet lamps are installed parallel with airflow, TiO_2 plate must be mounted around the four sides of the duct for maximum exposure. The limitation of this method is that it is hard to ensure that all the air effectively pass through the PCO system since only the VOCs in the air close to the duct surface could be influenced by the photocatalytic reaction. The larger the diameter of the duct, the less exposure (smaller view factor) is. In order to ensure that all the air passing through the duct participates in the photocatalytic reaction, a TiO_2 plate may be installed perpendicularly in the duct. From this point of view, UV lamps also need to be installed parallel with TiO_2 plate so they could deliver more UV energy to TiO_2.

In addition, the number of UV lamps in the UV-PCO unit is another important consideration. If there are not sufficient lamps to deliver the required UV energy to the TiO_2, the hydroxyl radical concentrations become a rate-limiting process, and the efficiency of PCO system is reduced. If too many lamps are used, energy is wasted. Furthermore, the adsorption coefficient decreases with the higher light intensity due to an increase of temperatures in local area. Therefore, this is a complicated problem which involves many factors, such as the output of the UV lamps, the distance between the lamps and the TiO_2 surface and the size of the duct.

2.1.4 PCO Reaction By-products

The main concern in the application of the PCO technology in an HVAC system is the formation of the undesired by-products. However, the concentration of the

individual VOC by-products in the indoor air is typically in the range of parts per billion (ppb). It is a big challenge to detect the very low concentrations of the by-products that may cause health concerns. Table 2-2 summarizes the by-products of PCO degradation of different gas-phase contaminants.

Table 2-2 By-products of PCO reactions

Primary contaminant	By-products	Analysis methods	Ref.
benzene	phenol	GC/MS, HPLC	d'Hennezel et al., 1998
heptane	propanal, butanal, 3-heptanone, 4-heptanone, carbon monoxide	GC/TCD, GC/MS	Shang et al., 2002
n-Butanol	butanal, propanal, ethanal, crotonaldehyde	GC/MS, GC/FID	Kirchnerova et al., 2005
formaldehyde	carbon monoxide	Q-Trak Indoor Air Quality Meter	Liu et al., 2006
phenol	o-DHB, p-DHB, 1,4-BQ	HPLC	Ortiz-Gomez et al., 2007
toluene	benzyl alcohol, benzaldehyde, benzoic acid, p-toluquinone, cresol	GC/MS, GC/FID	Guo et al., 2008
diethyl cyanophosphate	HCN, diethylphosphate, acetic acid, formic acid	FTIR	Kolinko and Kozlov, 2008
xylene	ethylbenzene	GC/MS, GC/FID	Boulamanti et al., 2008
acetone	formic acid, acetic acid, formaldehyde, bicarbonate	FTIR	Hernandez-Alonso et al., 2009
1-propanol	propionaldehyde, acetaldehyde	GC/MS	Vincent et al., 2009

Most PCO reactions are stepwise, which means they take many steps to form the final reaction product. An intermediate is generated by one of the middle-steps of the PCO reaction. Therefore, intermediate formation has a close relationship with the PCO reaction mechanisms of different contaminants. The appearance and the concentrations of the by-products depend on the experimental conditions, the PCO reactor configurations, the characteristics of the catalysts, as well as the different analytical methods (Kirchnerova et al., 2005; Boulamanti et al., 2008). Shang et al. (2002) and Vincent et al. (2009) found that concentration of the by-products is reduced with the increase of the contact time of the contaminant with UV illumination. Some by-products accumulated on the surface of the catalysts result in deactivation of the catalysts.

Ozone (O_3) is another problematic by-product which seriously impacts people's health. The process to generate O_3 includes two stages: first, oxygen breaks into two oxygen atoms with the illumination of the UV light; secondly, the highly unstable atom combines with oxygen to form O_3. O_3 is mainly produced by the 185 nm UV wavelength. The O_3 level which can be produced by a VUV lamp and the amount of O_3 which can be removed by a PCO filter need to be further examined in this study.

2.1.5 Economics of PCO

Lamp Life

Many factors are associated with the overall life of the UV lamps. There is no standard to rate the different UV lamps for the IAQ applications. After the UV lamps

are produced, UV lamp manufacturers always provide the expected lamp life data based on their evaluation system. In actuality, the UV lamps used in the PCO system may not reach their expected life-time due to the real operating currents and the ambient conditions. Currently, the method which has been widely used by the manufacturers to rate lamp life attempts to measure the time when the lamp's irradiance drops to 70% of the original output (Jin et al., 2007). Some typical lamp life-spans are outlined in the Table 2-3.

Table 2-3 Typical rated lamp life
(provided by Triatomic Environmental Inc.)

Lamp Type	Quartz Type	Filament Type	Rated Life Span
Twin Tube Lamp	Soft Quartz	Filament	6,000 hours
"Hot" Filament Lamp	Hard Quartz	Filament	9,000 hours
High Output "Hot" Filament Lamp	Hard Quartz	Filament	8,000 hours
Filament Guard Lamps	Hard Quartz	Filament with Cathode Guard	12,000 hours
Filament Guard Lamps with Ambient Quartz Shield	Hard Quartz	Filament with Cathode Guard	14,500 hours
Cold Cathode	Hard Quartz	Cold Cathode Electrode	20,000 hours
Cold Cathode with Ambient Quartz Shield	Hard Quartz	Cold Cathode Electrode	24,000 hours

One can expect that the irradiance emitted from a light source diminishes with the illumination time. During the continuous operation of a hot cathode fluorescent light source, (i.e., low-pressure Hg vapor lamp), the gradual thinning of the tungsten filament can lead to a complete failure of the bulb. The decrease in the light irradiance with illumination time affects the performance of the photocatalytic reaction. The shorter wavelengths tend to age more rapidly (Jin et al., 2007). Annual replacement of

lamps is usually recommended for low-pressure lamps.

Henschel (1998) argues that electricity for operating the UV bulbs and bulb replacement cost constitute the two main contributions to PCO operational cost. If the system was installed with low-pressure fluorescent bulbs of 10,000 h lifetime instead of medium-pressure bulbs of 1,000 h lifetime, $2,370 annual cost due to bulb replacement in the 9,900 W reactor could be saved.

Catalyst Life

Many studies reported that photocatalysts would be deactivated after working for a certain period of time (d'Hennezel et al., 1998; Alberici and Jardim, 1997; Ameen and Raupp, 1999). The common phenomena mentioned during the deactivation include the appearance of yellow viscous material on the surface of TiO_2 and decreased reaction rate of PCO. Not all yellow materials have been analyzed and identified, and part of it is regarded as the intermediates by several investigators. Zhao and Yang (2003) concluded from their literature review that deactivation may originate from fouling which changes the catalyst surface by blocking pores, but overall generation of reaction residues which cause the loss of active sites on the surface. Some intermediates are irreversibly chemically adsorbed; they accumulate at the catalyst surface, which gradually retard the reaction and finally stop it due to lack of reagents. PCO degradation of toluene was experimentally demonstrated by Cao et al. (2000). The authors found no hydroxyl groups on the surface after the deactivation of the catalyst. Benzaldehyde and benzoic acid have been identified as the most important poisoning species (Ibusuki and Takeuchi, 1986; Luo and Ollis, 1996; Ao et

al., 2004; Cao et al., 2000). These two species are intermediates of various primary contaminants.

The regeneration of the catalyst was also examined (d'Hennezel et al., 1998; Alberici and Jardim, 1997; Ameen and Raupp, 1999; Jing et al., 2004). Jing et al. (2004) compared the lifetimes of ZnO and TiO_2 nanoparticles challenged with n-C_7H_{16} or SO_2 in PCO system, and results indicated the photocatalytic performance of TiO_2 is superior to that of ZnO due to a longer lifetime. There are two approaches which have been widely used for the catalyst regeneration. The first one is to expose the catalyst surface to humid air under the UV radiation. The second is to illuminate the catalyst in the presence of hydrogen peroxide. Either way, the catalyst regeneration cost is a major part of the operational cost. Henschel (1998) suggested that the catalyst regeneration frequency should be every six months and the catalyst replacement frequency should be every five years.

2.2 Kinetic Models of PCO

The whole PCO chemical mechanism, Eq. (2-1) to (2-9), is often described as a uni-molecular decomposition reaction or bimolecular combination reaction, although more complex interactions may also exist (Masel, 1996). When considering the uni-molecular decomposition of the VOC at the catalyst surface, the rate of VOC removal is given by:

$$r = -\frac{dc}{dt} = k_r c_s, \qquad [2\text{-}10]$$

where k_r (s^{-1}) is the global kinetic coefficient of the oxidation reaction, and C_s is the

sorbed-phase concentration of the VOCs. Using the Langmuir-Hinshelwood model (L-H model) as an adsorption isotherm model:

$$C_s = f(C) = \frac{C_s^0 KC}{1+KC}, \qquad [2\text{-}11]$$

where C_s^0 and K are Langmuir's parameters. Substituting Eq. (2-11) into Eq. (2-10) gives:

$$r = -\frac{dC}{dt} = \frac{k_0 KC}{1+KC}, \qquad [2\text{-}12]$$

In this expression, k_0 (s^{-1}) = k_r C_s^0 is a synthetic kinetic rate coefficient that embeds both the kinetic coefficient of the oxidation reaction, k_r, and the sorbed-phase concentration corresponding to the monolayer coverage of the surface, C_s^0.

By rearranging Eq. (2-12), one obtains,

$$\frac{1}{r} = \frac{1}{k_0 K} \cdot \frac{1}{C} + \frac{1}{k_0}, \qquad [2\text{-}13]$$

where $1/Kk_0$ and $1/k_0$ can further be obtained experimentally: from the slope and intercept of the fitting curve of 1/r and 1/C.

Since indoor air contains hundreds of contaminants, a competition for adsorption at the catalyst surface may occur. In this case, the sorbed-phase concentration of the VOCs is decreased in a way that can be described by the extended Langmuir equation (Kapoor et al., 1990):

$$C_s = f(C_i) = \frac{C_s^0 KC}{1+\sum_{i=1}^{n} K_i C_i} \quad \text{i=1,2, …n,} \qquad [2\text{-}14]$$

where the terms K_i and C_i stand for Langmuir's constants and the air-phase

concentrations of the species i, respectively, and n is the total number of species contained in the air. Substituting Eq. (2-14) into Eq. (2-10) gives:

$$r = k\frac{KC}{1+\sum_{i=1}^{n} K_i C_i}, \qquad [2\text{-}15]$$

This model has been used by Turchi et al. (1995) and Wang et al. (1999) to investigate the adsorption competition between isopropanol, acetone and methanol and the adsorption competition between dichloroethylene and water molecules, respectively.

If considering that the PCO process of a given VOC originates from a bimolecular reaction, the removal rates of each reagent i, r_i, is the product of kinetic rate of the reaction, k_r, the stoichiometric coefficient of the compound in the reaction, ξ_i, and the sorbed-phase concentrations of both reagents:

$$r_i = -\frac{dC_i}{dt} = k_r \xi_i \prod_{j=1}^{2} c_{sj}, \qquad [2\text{-}16]$$

Using the Langmuir's adsorption isotherm model for each reagent, Eq. (2-11) leads to the following PCO kinetic model:

$$r_i = k_i \frac{K_i C_i K_{j,j\neq i} C_{j,j\neq i}}{\left(1+K_i C_i\right)\left(1+K_{j,j\neq i} C_{j,j\neq i}\right)}, \text{ i =1,2,} \qquad [2\text{-}17]$$

where k_i embeds the kinetic coefficient of the global reaction, the stoichiometric coefficient of the compound i in the reaction and the coefficients C_s^0 of the two reagents.

Practically, Eq. (2-17) proves to be relevant if the hydroxyl radical concentration at the catalyst surface may become rate limiting or, by extension, if the moisture content of the air is sufficiently low so that advective transport of water vapor

becomes the rate limiting process of the whole PCO process. In such a case, the species i and j of Eq. (2-17) are the VOCs of interest and the humidity. This model, or similar ones, has been proposed by several researchers (i.e. Adamson, 1982); further developments would come from the implementation of Eq. (2-14) instead of Eq. (2-11) if competition for sorption is to be considered. However, one limitation of water competition model is that the adsorption equilibrium data of water vapour usually shows two inflexion points and thus does not fit a Langmuir isotherm (Restrepo and Mosquera, 2009). Therefore, the models can fail in the range of high humidity (up to 70%). It must also be noted that the above mentioned kinetic models only represent steps 3 to 5 of the whole PCO process (see Figure 2-1). Generally, it is assumed that the air-phase concentrations over the catalyst surface are uniform and the same as in the bulk air-phase of the airflow, which may be a very rough assumption if boundary layer (BL) diffusion is rate limiting. This problem can nevertheless be easily overcome by coupling in series Eq. (2-12), Eq. (2-15) or Eq. (2-17) with the equation(s) representing the mass conservation of species within the bulk-air phase of the flow on one hand, and BL diffusion equation(s) on the other hand. The mass conservation equation(s) account for the advective transports and the boundary layer mass flux. Thus, the BL diffusion equation is given as:

$$\frac{\partial c}{\partial t} = k_g \nabla c \quad , \qquad [2\text{-}18]$$

where c is the local air-phase concentration and k_g (m/s) is the convective mass transfer coefficient. The convective mass transfer coefficient can be related to the airflow rate through the correlation between dimensionless numbers.

Another possible shortcoming of the PCO kinetic models is that mass transports only occur on the irradiated surface that is exposed to the airflow, while experimental studies show that catalyst porosity can be a key factor in determining the photocatalytic performance of TiO_2 coatings (Tanaka and Suganuma, 2001; Yi et al., 2008). The significance of solid-phase transports actually depends on the nature of the catalyst. Most PCO devices now use thin coatings or films made from nano-sized TiO_2 powders. Depending on the way the photocatalyst is applied (sol-gel process, chemical vapour deposition, physical vapour deposition or thermal spraying) and further treated (drying, heating/calcinations for better adhesion on the support), the structural properties can be different. For instance, Tanaka and Suganuma (2001) noted that the apparent porosity of the same type of TiO_2 gel decreased from 50% to less than 2% when the calcination temperature was increased from 150 to 600°C. Meanwhile, the effective surface area determined by the BET technique decreased from 210 to 0.2 m^2/g; Krysa et al. (2004) obtained similar results. Finally, Tomkiewics et al. (1994) reported that some commercial TiO_2 powders have porosity and specific surface area as high as 80% and 426 m^2/g, respectively, with a pore size distribution in the range of mesopores (2-50 nm). These structural properties suggest that the surface area available for adsorption of gases on the solid surface can be much higher than the catalyst surface area that is exposed to the airflow. Moreover, Obee (1996) indicated that UV light intensity decreases exponentially as the distance to the exposed surface increases, and, thus, suggested that photo degradation may occur at the pore surfaces, with a lower activity of the catalyst.

Considering that chemical kinetics are constrained by the diffusion and the sorption processes that determine the amounts of reagents locally available, the contaminant's mass transports within the catalyst could be represented by implementing Eq. (2-12) or Eq. (2-17) into Fick's law(s) , which represents the pore diffusion of reagent(s) and is given by:

$$\frac{\partial C}{\partial t} = D\nabla^2 C \qquad [2\text{-}19]$$

where ∇ is the three-dimensional Laplacian, $\frac{\partial^2}{\partial x^2}+\frac{\partial^2}{\partial y^2}+\frac{\partial^2}{\partial z^2}$, D is the diffusion coefficient, and c is the gas phase concentration over the catalyst surface.

In this case, the local photodegradation rate of the compound, r (Eq. (2-10)), is a function of local reagent concentration(s) and the global kinetic rate constant of the degradation reaction that would vary according to the UV light extinction within the catalyst. If the photochemistry within the pores is not to be considered due to insufficient irradiation, i.e. r = 0 within the catalyst, this equation could account for the sorption dynamics of the contaminant. These phenomena may greatly affect the PCO efficiency, especially during the early stage of system operation, (before the contaminant reaches adsorption equilibrium for the concentration tested). They may be the reason why many authors noted the decrease of the removal efficiencies after the system is switched on (d'Hennezel et al., 1998; Alberici and Jardim, 1997; Ameen and Raupp, 1999).

Implementing the boundary layer and the catalyst internal diffusion models would provide a detailed modeling of all steps involved in the PCO process, thus

allowing for a thorough analysis of the factors determining the removal efficiency. However, the issue is that several model parameters have to be determined experimentally, which can be a demanding task. In this context, the approach proposed by Zhang et al. (2003) may be more practical. Fundamentally, Zhang et al.'s model is made of the following two equations and boundary conditions to describe the VOC transport through the photocatalytic reactor:

$$\frac{-QdC}{Wdx} = KC_s(x), \qquad [2\text{-}20]$$

$$KC_s(x) = k_g\left[C(x) - C_s(x)\right] \qquad x = 0,\ C = C_{in}, \qquad [2\text{-}21]$$

where Q is the volumetric airflow rate (m^3/s), W is the catalyst plate width (m) and x is the spatial dimension perpendicular to the surface. C is the average VOC air-phase concentration and C_{in} is the inlet air VOCs concentration. Here, C_s stands here for the air-phase VOC concentration over the catalyst, and K_g stands for the convective mass transfer coefficient. Finally, K (m/s) is called the reaction rate constant which also includes the contribution of adsorption, desorption and possibly internal diffusion.

Zhang et al. (2003) then used an analogy between heat exchangers and photocatalytic reactors as a way to express the photooxidation performance of the PCO reactors as a function of only two parameters: the system efficiency and the number of mass transfer units (NTU_m). The number of mass transfer units is a function of the airflow rate, Q, the physical parameters, k_g and K, as well as the surface area of the catalyst, A (m^2):

$$NTU_m = \frac{KA}{Q\left((1+\frac{K}{k_g})\right)} \quad . \qquad [2\text{-}22]$$

Moreover, the NTU_m is related to η through the relation:

$$\eta = 1 - e^{-NTU_m} \quad . \qquad [2\text{-}23]$$

Based on Eq. (2-22) and (2-23), Zhang et al.'s method involves the following steps:

1) Determining the NTU_m experimentally (for the VOCs and operating conditions of interest),

2) Calculating η from Eq. (2-23), and

3) Determining the room VOCs concentration(s), and subsequently assessing the impact of the cleaning system from the mass balance, where the contribution of the PCO system is easily modeled using the computed efficiency.

For instance, assuming the perfect mixing of the air within the room, no contaminant sources and no sinks, other than the PCO air cleaner operating on the recirculated air, the mass balance will become (Zhang et al., 2003):

$$V\frac{dC}{dt} = QC_{(t)}\left(1 - e^{-NTU_m}\right) \quad . \qquad [2\text{-}24]$$

Compared to the detailed model, the great advantage of this method is that only one parameter is to be determined experimentally (NTU_m). It is, nevertheless, challenging as it may be considered a dynamic model. K embeds the contributions of adsorption and the surface chemical kinetics, two processes that depend upon concentration, $C_{(t)}$, and also on temperature if non isothermal conditions are to be considered.

2.3 Factors Affecting Efficiency

2.3.1 Contaminant Mixtures

As the indoor air contains a variety of contaminants, some studies investigated the

conversion efficiency of binary or even ternary mixtures of contaminants (Litchin et al., 1996; Luo and Ollis, 1996; Pengyi et al., 2003; Ao et al., 2003a; Ao et al., 2003b; Ao et al., 2004). No general conclusion can be drawn from these studies since different species affect the PCO efficiency of the target VOCs differently, as shown by Ao et al. (2004). The investigations between PCO and formaldehyde lead to the following consensus:

- The presence of nitric oxide (NO) promotes the photocatalytic conversion of formaldehyde. Photo-dissociation of NO yields hydroxyl radicals which initiate the oxidation process in a way that has been further explained by Devahasdin et al. (2003).
- On the other hand, sulfur dioxide (SO_2) inhibits the conversion of formaldehyde. SO_2 reacts with water vapour to yield sulfate ions. The latter accumulate at the catalyst surface with the adverse effect of decreasing the adsorption of formaldehyde molecules. Studies show that sulfate ions also inhibit the conversion of ethylene, ethanol and dichloroethane (Ao et al., 2004).
- Similarly, aromatic hydrocarbons decrease the conversion efficiency of formaldehyde. Here, the intermediates, such as benzaldehyde, are generated and remain strongly bonded to the surface, thus blocking reaction sites. After some time, this can lead to a complete deactivation of the catalyst.

The same compound can affect the removal rate of various VOCs differently. For instance, Lichtin et al. (1996) noted that the presence of trichloroethylene promoted the removal rate of i-octane, dichloromethane and trichloromethane but inhibited the

acetone conversion. Finally, Ao et al. found (2004) the impact of VOCs concentration on the conversion of target VOCs. To some extent, this is consistent with the fundamentals of mass transports in PCO devices. Based on the aforementioned results and subsequent considerations, it can be concluded that the presence of chemicals can affect the conversion of the target VOC:

- Physical interactions contribute to the decrease in the adsorption of the target VOCs: all gases compete for adsorption on the catalyst surface in a way that not only depends on their affinity for sorption, but also on their concentrations (see Langmuir's multi-component adsorption isotherm model, equation 2-14). The higher the number of species in the air and/or their concentrations, the lower is the sorbed-phase concentrations of each VOC. Consequently, some contaminants will affect the conversion of the target VOCs if tested at high concentrations, but their influence may actually be negligible in the context of indoor air applications, where gas concentrations seldom exceed few tens of parts per billion (ppb). Additionally, some chemicals produce sticky intermediates that block active sites on the catalyst surface. The higher the concentration of these chemicals, the higher is the yield of the intermediates and, thus, the lower is the adsorption of the target VOCs.
- Chemical interactions can either promote or inhibit the oxidation process of the target VOCs: all species undergoing photodegradation consume hydroxyl radicals and superoxide ions, which may, in some conditions, turn to the rate-limiting phenomenon of the VOC degradation process. On the other hand, some chemicals

can increase the yield of these precursors. This is not only likely to be the case of nitric oxide, as mentioned above, but also of ozone (Pengyi et al., 2003).

The fact that the presence of contaminants globally affects the degradation of the target VOCs is the result of these dual interactions. The dominating processes can be different, and does not only depend on the nature of the species, but also their concentrations and the operating conditions of the system. Hence, multi-component mixtures either promote or inhibit the conversion of the target VOCs. Further research considering mixtures of contaminants at low concentrations is needed to determine which effect is more likely to dominate the PCO process in the context of indoor air applications.

2.3.2 Humidity

Based on the elemental approaches presented in Section 2.1, the influence of humidity on the target VOCs' conversion efficiencies can be interpreted the same way as that of the for contaminant mixtures, with the exception that the typical water vapor concentrations in the air are several orders of magnitude higher than those of the contaminants. Molecular water and hydroxyl groups, which are generated by chemical decomposition, can be weakly or strongly adsorbed on the surface of TiO_2. If there is a lack of humidity on the surface, the efficiency of PCO for some chemical compounds can be seriously reduced. On the other hand, excessive water vapor on the surface of the TiO_2 can also decrease the photo-activity because abundant water molecules tend to occupy the active sites of the reactants on the surface. Moreover,

the presence of water may enhance the efficiency of electron-hole recombination, which is an unfavourable process for the photocatalytic oxidation of air contaminants (Park et al., 1999). Therefore, the optimal humidity could be determined by the balance between conversion promotion through the chemical processes and inhibition through the physical interactions.

The concentrations specifically configured for the air cleaning process become a key issue once again. Because contaminants are present in very low concentrations in the indoor air, it is unlikely that the hydroxyl radical concentrations will become rate limiting for systems operating in rooms or in the HVAC units of residential and office buildings. Competitive adsorption and the electron-hole recombination can be viewed as the dominating interaction processes under the condition that the relative humidity is achievable in buildings and HVAC system. In other words, the conclusion would be that the best condition for PCO of the indoor air contaminants occurs when the air incoming to the system is at its lowest relative humidity. This is somewhat supported by experimental results. When concentrations in the parts per million (ppm) level or higher have been tested, most studies suggest that there is an increase in the conversion efficiency with an associated increase in the humidity (Luo and Ollis, 1996; d'Hennezel et al., 1998). On the other hand, when tested at the concentration levels that are representative of normal indoor air, experimental results generally show inhibition of the conversion efficiency of VOCs. For instance, Ao et al. (2004) studied PCO of formaldehyde with the incoming air concentration of 50 ppb. To fit

the reaction rate, r, (mol/m^2/min), with an increase in the air humidity, [H_2O], (ppm), they derived the following relationship:

$$\frac{1}{r} = 1.56003 + 0.001302[H_2O]^{0.88917} \qquad [2\text{-}25]$$

Practically, Ao et al. (2004) observed a decrease in the conversion efficiency of formaldehyde from 80% to 54% when the humidity level was increased from 2100 ppm (10% RH) to 22000 ppm (80% RH). Yu et al. (2007) also studied the photocatalytic degradation of formaldehyde, but at a slightly higher concentration of 750 g/m^3. They observed a decrease in the conversion rate from 83% to 33% when the relative humidity of air was increased from 40% to 70%.

Ao and Lee (2003) tested benzene, toluene, ethylbenzene and xylenes (BTEX), and their results revealed the same trend as for formaldehyde, but with even higher impact of humidity on the degradation rates. The conversion of toluene, for instance, was decreased from 72% to 19% when the humidity level was increased from 2100 to 22000 ppm. When they tested BTEX at much higher concentration (152 ppm), air humidity was shown to promote the conversion of toluene (Einaga et al., 2002). Finally, Luo and Ollis (1996) concluded that toluene (80-550 mg/m^3) oxidation rate increased with water concentration up to 2000-3000 mg/m^3 and decreased thereafter.

2.3.3 Air Temperature

Temperature impacts the reaction rate in many different ways: it influences the adsorption, the kinetic reaction, and the desorption processes.

According to the Arrhenius equation, the rate constant k of chemical reactions is

dependent on the temperature, T, and the activation energy, E_a.

$$k \propto f(\exp(-\frac{E_a}{RT})) \quad , \qquad [2\text{-}26]$$

where R is the gas constant. Usually, the activation energy E_a is greater than zero; hence, an increase in the temperature results in an acceleration of the reaction rate.

Adsorption is an exothermic process so that high temperatures are not conducive to adsorption. The adsorption constant, K, abides a temperature dependence equation (Doucet et al., 2006)

$$K \propto f(\exp(+\frac{Q'}{RT})) \qquad [2\text{-}27]$$

where Q' is the rate of heat generation due to adsorption.

On the other hand, desorption is an endothermic process. Higher temperatures facilitate an easy removal of the reaction products, such as carbon dioxide (CO_2), from the photocatalyst surface, consequently, creating more active sites for the PCO reaction (Yu et al., 2007).

From the above-mentioned data, it can be said that, while low temperatures are beneficial to the adsorption process, high temperatures are good for kinetic reactions and desorption processes. Because of this trade-off, under certain conditions, one of the three processes becomes dominant and starts to control the overall reaction rate. For example, an increase in temperature enhances the reaction rate when a kinetic reaction or desorption is the rate-limiting process, while a decrease in temperature enhances the reaction rate when adsorption is the rate-limiting process. This may be the reason why some researchers come to different conclusions while carrying out

experiments with different contaminants (Obee and Brown, 1995; Fu et al., 1996b; Obee and Hay, 1997).

It can also be noted that the optimal temperature may vary with different compounds. For formaldehyde, the temperature of the highest degradation rate is 25℃, which indicates that UV-PCO is a promising energy-saving technology for the oxidation of indoor air pollutants (Yu et al., 2007).

2.3.4 Air Flow Rate

The airflow rate of a reactant may also affect the reaction rate. Low and high airflow rates have different impacts on the PCO reaction. On the aspect of low airflow rate, Yu et al. (2006) investigated the relationship between the oxidation rate and the gas flow rate with 5 ppm VOCs. Their study showed that the oxidation rate increases with an increase in the airflow rate for mesitylene, m-xylene, ρ-xylene, toluene, n-hexane and iso-butanol at low flow rates (0-600 ml/min). The gas-phase mass transfer strongly affects the oxidation rate during this diffusion-controlling phase. At the same time, the oxidation rate does not change significantly with a higher flow rate but plateaus when the airflow rate exceeds 1000 ml/min. This indicates that, under this condition, the surface reaction mainly controls the oxidation rate, while the gas-phase mass transfer effect is negligible.

With respect to a high airflow rate, Ginestet et al. (2005) designed a PCO air cleaner for aircraft cabin applications using an Ultraviolet A (UVA) and UVC lamp. Their investigations clearly show the influence of the airflow rate on the efficiency of

the PCO unit. When the airflow rate is increased from 40 m^3/h to 80 m^3/h, the efficiency of the system is reduced by half. These authors also present a similar relationship between the photo-oxidation of acetone and toluene. The results of their study indicate that the conversion is strongly dependent on the residence time in the photo-reactor. Tomasic et al. (2008) and Yu et al. (2007) also came to the same conclusion.

Since a typical face velocity expected in HVAC system is around 1.8 m/s, the mass transfer effect is not considerable. The multi-pass method may be a good choice to relatively extend the residence time of VOCs in the PCO system.

2.3.5 Irradiance

Light intensity plays a crucial role in the reaction rate. Usually, the pollutant decomposition rate increases with an increase in the irradiance (Wang et al., 1998; Jacoby 1993; Obee and Brown, 1995). Obee and Brown (1995) summarized the empirical correlation between the reaction rate and the light intensity:

$$r \propto \begin{cases} I^{1/2} & I > one\,sun \\ I & I \le one\,sun \end{cases} \qquad [2\text{-}28]$$

In this equation, r (ppm/min) is the reaction rate, I (mW/cm^2) is the UV irradiance, and one sun is defined as the light the sun emits at about 1-2 mW/cm^2 for wavelengths below 350 and 400 nm. Thus, at a low light intensity, electron-hole pairs effectively participate in chemical reactions, whereas the recombination of the electron-hole pairs inhibits the rate of electron transfer at high light intensity.

The model used to predict the relationship between the reaction rate constant, k, and the light intensity was described by Silva and Faria (2009):

$$k = \alpha I^{\beta}, \qquad [2\text{-}29]$$

where α is the proportionality constant, and β is equal to 1.0 or 0.5 for the low and high absorbed light intensity, respectively. It can be seen that the reaction rate constant increases with an increase in the light intensity, since more hydroxyl radicals are generated for the oxidation reactions.

The effect of the light intensity on the apparent adsorption constant K was also modeled by Silva and Faria (2009) on the basis of pseudo-steady state:

$$K = \frac{k_1}{k_{-1} + \alpha I^{\beta}} \qquad A \underset{k_{-1}}{\overset{k_1}{\Leftrightarrow}} A_{abs}\ , \qquad [2\text{-}30]$$

where k_1 and k_{-1} are the constants representing the adsorption and the desorption of the reagents on the catalyst surface, respectively. The results show that K decreases at higher light intensities. A similar trend was obtained by Yu et al. (2008) and Du et al. (2009). Thus, it means that active species, such as electron-hole pairs and hydroxyl radicals, occupy a large portion of the whole catalyst surface, resulting in a lesser amount of the active surface available for the absorbed reagents and, as such, in a smaller value of K.

2.3.6 Reflection and Soiling

When light is emitted from a lamp, some of it may directly reach the surface of TiO_2 and provide the energy for the reaction, while the rest of it may hit the duct surface, reflect several times and then reach the TiO_2. The reflection of the light

depends on the properties of the interface. Even without considering the soiling effect, the duct surface is not smooth, and causes the light to bounce off in all directions. Decreasing the wall reflectivity decreases the light intensity and efficiency, and creates an insignificant effect of wall reflectivity with an increase in the absorption coefficient (Khalifa, 2005; Yu et al., 2008).

Besides the duct surface reflection, there is also the TiO_2 surface reflection. Brucato et al. (1997) and Hossain and Raupp (1999) developed a 3D-model to account for these reflections in a monolith channel. They assumed that the light reflecting from the thin-film coating diffuses perfectly, and that the optical thin-film properties are only dependent on the light wavelength λ. The empirical reflectivity expression fits well with the measured data and can be described as follows (Hossain and Raupp, 1999):

$$\rho(\lambda) = 0.515 + 0.455 \times \tanh[(\frac{\lambda - 420}{20}) + 1.85] \quad . \qquad [2\text{-}31]$$

The corner of the duct may be a good place to utilize the reflection, but the soiling effect also can easily appear at this place. Soiling is a very complicated phenomenon in a duct system. Many factors can lead to undesired results, including the quality of the air, the airflow rate, the UV-lamp temperature and the type of lamps. Soiling affects the lamp output and prevents the uniform delivery of UV-light to the TiO_2, causing a reduction in the PCO efficiency. The duct wall also becomes soiled in a long-term operation, which also causes a reduction in reflection. Hence, it is highly recommended that pre-filters are installed prior to the installation of the lamps to

collect particulates.

2.3.7 Mass Transfer Effect

The overall processes of conversion of VOCs to products in heterogeneous photocatalysis involve a number of sequential steps described in Section 2.1.1. Although it is disputable that the PCO reaction may take place at a liquid stream, most of the researchers propose that only those pollutant molecules in direct contact with catalyst surface undergo the PCO reaction (Thompson and Yates, 2006; Gaya and Abdullah, 2008; Debono et al., 2011). The differences in concentration between those in the active sites within the catalysts and in the bulk stream provide the driving force for the various diffusions and mass transfers in the overall sequence.

The convective mass transfer coefficients can be derived from analogies between heat and mass transfers. In the case of heat transfer, the correlations for forced convection relate the Nusselt number, which includes the convective heat transfer coefficient in its definition, to the Reynolds number and the Prandtl number. In the case of mass transfer, the correlations relate the Sherwood number, which integrates the convective mass transfer coefficient in its definition, to the Reynolds and Schmidt numbers. Numerous empirical correlations have been developed in the literature. Generally, the influencing factors for the mass transfer include the geometry of the PCO filter, the fluid dynamics of the air stream through the PCO filter and temperature.

In the catalysis industry, when the temperature is less than 100℃, the mass

transfer is far faster than the chemical rate, and the limiting rate is controlled by the chemical process. When the temperature is higher than 500℃, the catalytic oxidation process is controlled by the mass transfer (Hawthorn, 1974). For the application of PCO technology in the HVAC system, the operational temperature is around or slightly higher than the ambient temperature. That way, on the one hand, it does not introduce thermal pollution, and, on the other hand, it does not require additional energy consumption to reduce the temperature to a comfortable level. Therefore, the mass transfer is not a rate-limiting process in this application.

2.3.8 Ozonation Effect

The application of ozone-producing lamps in the UV-PCO air cleaners inevitably introduces ozone into the duct system. Some researchers reported that the addition of ozone significantly enhances PCO of VOCs, as ozone is a powerful oxidizing agent (Yu et al., 2007; Zhang et al., 2003; Zhang and Liu, 2004). Ozone itself is a problematic by-product that may seriously threaten people's health through harming the normal function of the lungs and irritating the respiratory system. Therefore, it is of the upmost necessity to add an ozone filter to remove the excess ozone after the PCO air cleaner is installed into the air supply system.

In the past half-century, kinetics and the mechanisms of the gas-phase reactions of ozone with organic compounds, mainly those containing unsaturated carbon-carbon bonds, have been well examined in the atmospheric field. The possible reaction mechanisms of the chain reactions of the photolysis of O_3 are shown in the following

equations:

$$O_3 + h\nu\ (\lambda \leq 310\ nm) \rightarrow O(^1D) + O_2 \quad [2\text{-}32]$$

$$O(^1D) + H_2O \rightarrow 2\cdot OH \quad [2\text{-}33]$$

$$\cdot OH + Pollutant + O_2 \rightarrow Products\ (CO_2, H_2O, etc.) \quad [2\text{-}34]$$

$$O(^1D) + M\ (M=air) \rightarrow O(^3P) + M \quad [2\text{-}35]$$

The gas-phase reactions of ozone with various classes of organics under the conditions relevant to the atmosphere were discussed by Atkinson and Carter (1984), and the rate constants are summarized in Table 2-4.

Table 2-4 Rate constants k for the gas-phase reactions of O_3 with various compounds

Compound	k, $cm^3molecule^{-1}s^{-1}$	T, K	Technique[b]	Lifetime[a]
Alkane (i.e ethane, hexane)	$\leq 10^{-23}$	298±2	S-IR/CL	≥30 years
Acyclic Monoalkene (i.e ethene, hexene)	10^{-16}-10^{-18}	298±2	S/F-IR/CA/ CL/UV/FTIR /MS	1-10day
Cycloalkenes, cyclodialkenes, cyclotrialkenes (i.e d-limonene, pinene)	10^{-14}-10^{-16}	295±2	S/F-CL	0.03h-3h
Monocyclic aromatic (except styrene, i.e toluene, xylene)	$\leq 10^{-20}$	297±2	S-CL	≥30 years
Oxygen-containing compounds not containing double c-c bonds (i.e alcohols, ketones)	$\leq 10^{-20}$	297±2	S/F-CL/IR/ CA	≥3 years

Note: (a) The rate constants were calculated when an O_3 concentration of 1×10^{12} molecule cm^{-3} (i.e. around 40 ppb at ground level) was used.

(b) S stands for static system; F stands for flow system; MS stands for mass spectrometry; IR

stands for infrared absorption spectroscopy; FTIR stands for Fourier transform infrared absorption spectroscopy; UV stands for ultraviolet absorption; CL stands for chemiluminescence; and CA stands for chemical analysis.

From this table, it can be found that O_3 usually plays a positive role in removing alkenes. For alkanes, aromatics and oxygen-containing organics, the reactions are very slow, with the room temperature rate constants of $\leq 10^{-20}$ cm^3 $molecules^{-1}$ s^{-1}. Hence, these reactions are of negligible atmospheric importance. It is worthwhile to mention that the ozonation rate constants were computed under atmospheric conditions, in which O_3 mixing ratios were generally around 10-40 ppb at ground level, while the O_3 concentration produced by a VUV lamp can be much higher than that. In addition, the reaction time of O_3 with organics in the in-duct system is determined by the reaction length and the airflow rate; consequently, when the O_3 concentration is stabilized over time, the removal efficiency largely depends on the reaction time. Moreover, the formation of the by-products from ozone reaction and even redundant O_3 emission can be safety concerns. Therefore, it is clear that further studies are needed on the exploration of the performance of ozonation in the in-duct systems.

2.4 Major findings

PCO is a promising technology that can be applied to the HVAC systems to improve IAQ and to protect building occupants from intentional and unintentional releases of gases. Both experimental and modeling work have been conducted to understand the mechanism of PCO, as well as to optimize the operational conditions.

The following conclusions can be drawn from this review:

- The Langmuir-Hinshelwood model is widely used to quantify the PCO reaction rate. Different L-H models have been developed to predict the reaction rate under the conditions of uni-molecular reaction, bimolecular reaction and competition. A novel model, more accurately rating different kinetic parameters, is needed to explore the possibility of combining the L-H model with mass conservation, boundary layer diffusion, light intensity and the internal diffusion of the catalyst.
- The impacts of different kinetic parameters on the PCO efficiency, such as competition of mixtures, humidity, air temperature, air flow rate and light intensity, have been discussed. The relative limiting process between the physical and photochemical interactions controls the whole PCO process. The dominating processes are different and are based on the specific conditions, which is the reason why different results were reported in the literature.
- Intermediates of PCO are studied to further understand the mechanisms of the PCO process. Lamp life and catalyst life are examined to evaluate the maintenance and economics of the PCO process.

3. UV-PCO SYSTEM SET-UP AND QUALIFICATION TEST

3.1 Introduction

American Society of Heating Refrigeration and Air Conditioning Engineers, Inc. (ASHRAE) has been developing test methods for removal of various gaseous pollutants; however, these are mainly applicable for sorbent media like activated carbons and do not fairly evaluate the potential performance of new technologies. As discussed in the previous chapter, UV-PCO technology has a potential in air cleaning, however, the mechanisms involved in UV-PCO technology are complicated and different from those of adsorbents like activated carbons. At the same time, the majority of the work was done in bench-top scale reactors under ideal reaction conditions, which is not usually the case in real applications.

One of the main objectives of this research is to develop a methodology to evaluate the performance of the UV-PCO systems for the applications in mechanically ventilated buildings. To run extensive tests in a timely and efficient manner, a test rig composed of four parallel test ducts was designed and constructed. The details of this test setup, the chemical generation system and the analysis methods are explained in this chapter. In addition, the calibration of analytical instruments and the prequalification tests of the test rig are also discussed in this chapter.

3.2 Novel Test System

3.2.1 Test Apparatus

To develop a methodology for evaluating the performance of UV-PCO in real applications, a bench-top scale setup was not considered because the results of a test, which is based on the ideal experimental conditions, could be questionable and may not be scaled up to predict the performance of full-scale systems. As a consequence of the above mentioned considerations, an innovative UV-PCO system was designed and built. Figure 3-1 shows the schematic diagram of the test apparatus. The test rig was made of four parallel aluminum ducts with 0.3 m×0.3 m (1 foot×1 foot) inner cross section area. The system was able to provide up to 255 m^3/h (150 cfm) airflow rates (with the PCO filters) and was equipped with a radial fan with speed control mounted at the end of each duct. The geometry and dimensions of test rig on the elevation view are presented in Figure 3-2.

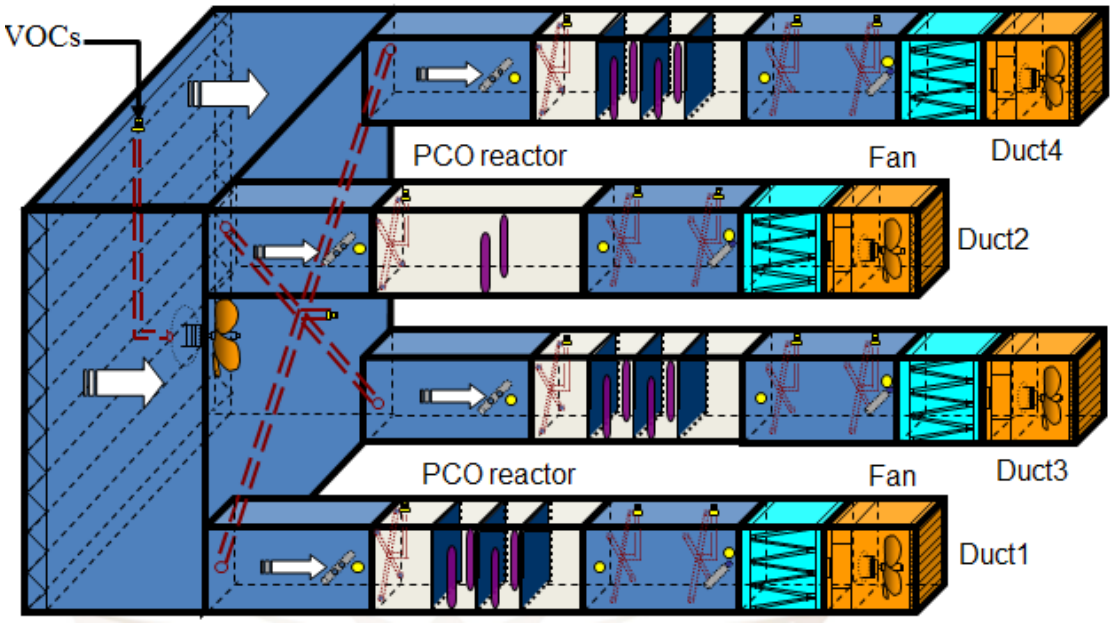

Figure 3-1 Schematic diagram of the experimental setup

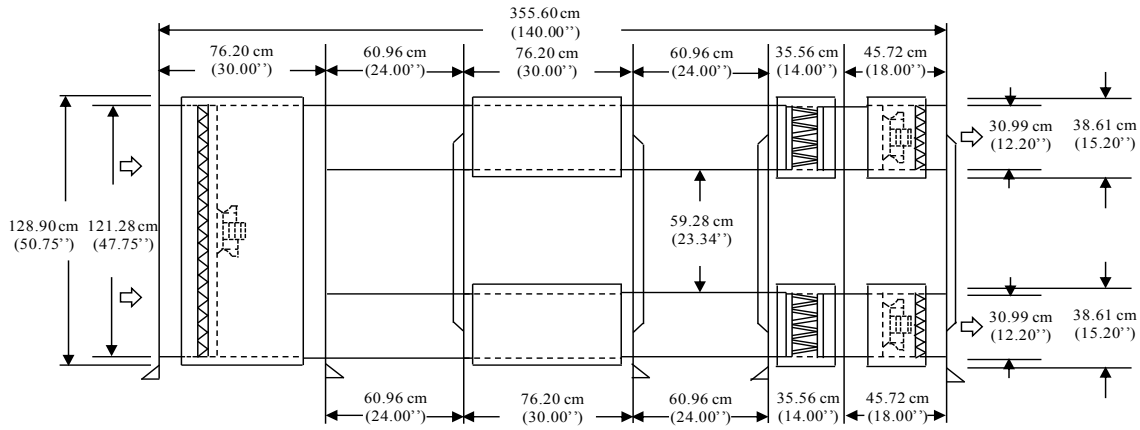

Figure 3-2 Dimensions of the test rig on elevation view

This was an open–loop mode system, and the laboratory air was introduced directly to the system after passing through a pleated fabric pre-filter. The function of the pre-filter was to remove particle pollutants, and further, to reduce the possibility of blocking the tested filter by dust deposits and to protect the fans. The air containing evaporated VOCs was introduced into the PCO system through a stainless steel tube and mixed with the laboratory air at the gas mixer chamber. The mixing part was composed of a fan surrounded by a mixing baffle and a perforated plate to provide a uniform dispersion before evenly feeding the air mixture into the four ducts. The conditions of the inlet air were monitored for humidity and temperature by a sensor (HMT 100, Vaisala) mounted at the center of the mixer chamber.

The upstream of each of the ducts was fitted with a perforated stainless steel cross tube with the outer diameter of 0.64 cm, to collect air samples, and an electronic low-flow probe (ELF-1200, EBTRON) at the center, to monitor the airflow rate. The UV-PCO reactor was designed to be versatile, so that different in-duct UV-PCO filters with various geometries could be installed (Figure 3-3). In this study, three ducts were

equipped with three PCO filters irradiated with four UV lamps arranged in two banks (Figure 3-1). The vertical distance between the surfaces of the UV lamps and the PCO filters was approximate 5 cm. Low-pressure mercury vapor lamps made by Atlantic Ultraviolet Corporation (Ster-L-Ray@U-shaped Slimline) were used as the light source. Detailed descriptions of the UV sources are provided in Section 3.2.2.1. In one of the ducts, only two VUV lamps were installed without the PCO filters in order to examine the ozonation effect. Two pressure taps were mounted before and after each of the PCO reactors. After the UV-PCO reactor, there was a probe installed at the center of each duct to monitor RH and temperature of air stream at downstream, respectively. Downstream was also fitted with two cross sampling tubes and one bulkhead union to provide ports for the collection of VOCs and ozone.

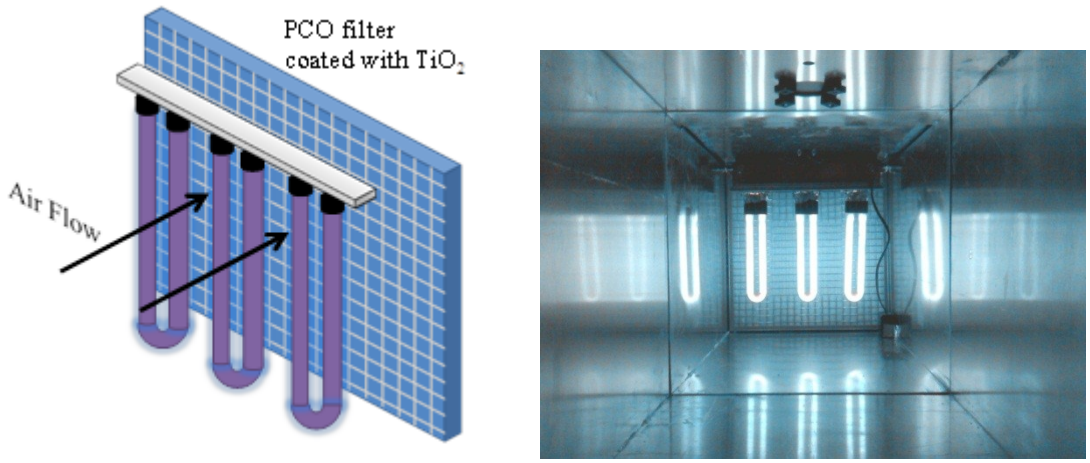

Figure 3-3 Schematic diagram of the photocatalytic reactor

The effluent stream was then introduced into the adsorption module, containing carbon and chemical absorbents to trap the residual VOCs and the generated by-products. For the application of ozone producing lamps, metal honeycombs coated with MnO_2 post-filters were installed at the end of the duct system for residual ozone

decomposition. The number of layers of MnO_2 post-filters employed in the experiments were determined by the O_3 concentration levels generated downstream, and, for all experiments, the outlet O_3 concentrations after the duct system were controlled to be less than 50ppb.

3.2.2 UV-PCO Reactor

3.2.2.1 UV Sources

A low-pressure mercury lamp (Ster-L-Ray, Atlantic Ultraviolet Inc.) was an instant-start lamp which utilized a coil filament on each end. The lamp had a double-pin connect at one ceramic end and was powered by ballasts that provided the starting electrical voltage to ionize the mercury vapour in the UV lamp and limited the current to a nominal level. The lamp life was governed by the electrode life and number of starts. The specifications of UV lamps provided by the manufacturer are listed in Table 3-1.

Table 3-1 Manufacturer's specifications of UV lamps (Ster-L-Ray, Atlantic Ultraviolet Inc.)

Lamp description		Length (mm)	Lamps Watts[a]	UV Output Total Watts[b]	UV Output μw at 1 meter[c]	Ozone Output[d]	Rated Effective Hours
Ozone free	Ozone producing						
G18T5L/U	G18T5VH/U	201	18.4	5.8	59	1.6	10,000

Notes: (a) Wattages is lamp watts only and does not include ballast loss.

(b) Ultraviolet output at 254 nm at 100 hours and 26.7℃ (approximate).

(c) Microwatts per square centimetre at one meter from lamp.

(d) Approximate ozone output in grams per hour under favorable conditions. Please note that ozone output is subject to considerable variation due to conditions under which the lamp is used; under many conditions, the ozone output may be only a fraction of the specified figure.

3.2.2.2 PCO Filter

Two commercially available PCO filters with different support media were tested in this study (Figure 3-4). PCO-A was a type of fibreglass with a TiO_2 film (TiO_2/FGFs) deposited on both surfaces. PCO-B was a type of carbon cloth with both surfaces coated with a film of TiO_2 (TiO_2/CCFs). The exact properties of each PCO filter could not be given due to the proprietary laws of these TiO_2 filters. The catalyst mats were mounted on stainless steel frames with 3.36 mesh screens supporting both the front and the back faces of the modular element. Table 3-2 gives detailed descriptions of the two PCO air filters.

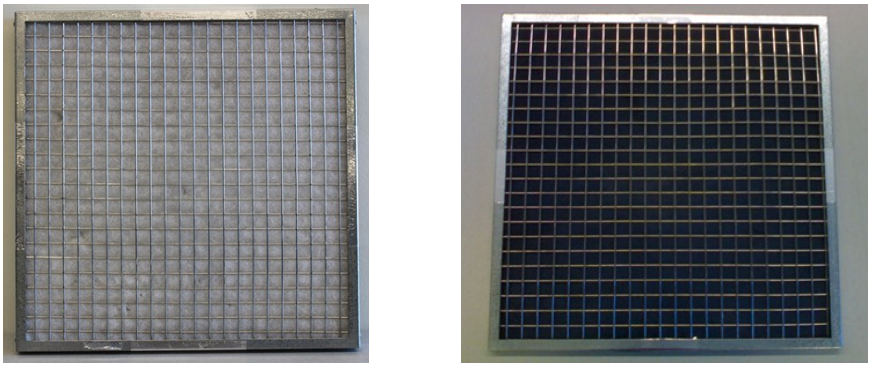

(a) TiO_2/FGFs (b) TiO_2/CCFs

Figure 3-4 PCO air filters

Table 3-2 Descriptions of three PCO filters

Filter Name	Catalyst Form	Supported Material	Air cleaning technology
TiO_2/FGFs	Thin-film	Fibreglass	UV-PCO
TiO_2/CCFs	Thin-film	Carbon cloth	UV-PCO + Sorption filtration

3.2.3 Contaminant Generation System

VOCs are referred to as the organic compounds that have boiling points roughly in the range of 50-250℃ （Health Canada, 93-EHD-166). Hence, most of the selected

VOCs were liquid at room temperature. The laboratory compressed air was used as the carried gas and its flow rate was controlled by a mass flow meter (Omega FMA 5400/5500), into which the VOCs were injected through a syringe pump (KD Scientific) (Figure 3-5). A chemically inert polytetrafluoroethylene (PTFE) tube was used as a contaminant vapor line through which the vaporized chemical was passed into the injection port. The port was placed on the top of the test rig in order to avoid condensation of the compounds on the interior duct surface. A perforated cross stainless steel tube with a diameter of 4.8 mm, which was connected with the tube transporting gaseous pollutants, was installed at the center of the duct system to uniformly distribute the VOCs in the four-duct system.

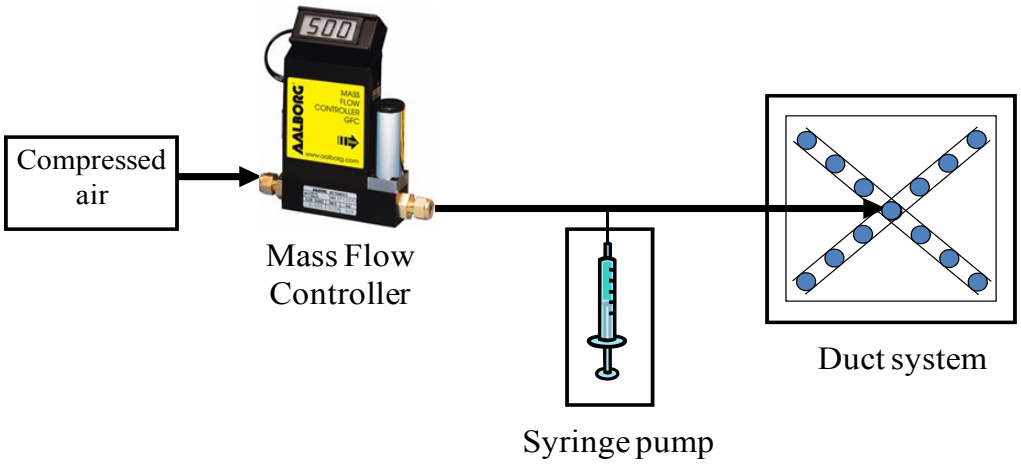

Figure 3-5 Liquid contaminant generation system

3.2.4 Sampling and Analysis Method

Figure 3-6 shows the experimental system used in this study. The inlet and the outlet concentrations of VOCs and gaseous by-products were qualitatively and quantitatively monitored by an online photo-acoustic multi-gas monitor (INNOVA

1312) equipped with an auto sampler (CBISS MK3) and an offline High Performance Liquid Chromatograph (HPLC, Perkin Elmer). The INNOVA and HPLC calibration method was developed, as shown in Appendices A and B, respectively. The concentration of ozone in each effluent stream was measured by a calibrated six-channel ozone analyzer (Model 465L) which was programmed to take samples alternatively and continuously from the downstream of each duct.

For the HPLC analysis, potential carbonyl by-products were trapped on a high purity silica adsorbent coated with 2, 4-dinitrophenylhydrazine (2, 4-DNPH) (Supelco LpDNPH S10L). Sample eluate was separated and analyzed by the HPLC with UV detection (360 nm) equipped with a C18 Brownlee validated micro-bore column (150 mm x 4.6 mm ID, 5μm film thickness). Acetonitrile and distilled water were used as the mobile phase with a flow rate of 1.0 mL/min. The following HPLC gradient analysis method of aldehyde/ketone-DNPH mixtures was developed: the ratio of 70% acetonitrile/ 30% water was held for 6 minutes, then the ratio increased to 100% acetonitrile/ 0% water and maintained for 3 minutes, and finally the ratio returned to 70% acetonitrile/ 30% water for 4 minutes.

The irradiance of 254 nm on the surface of the TiO_2 filter was monitored by a UV radiometer (Steril-Aire), whose calibration was traceable to the National Institute of Standards (NIST).

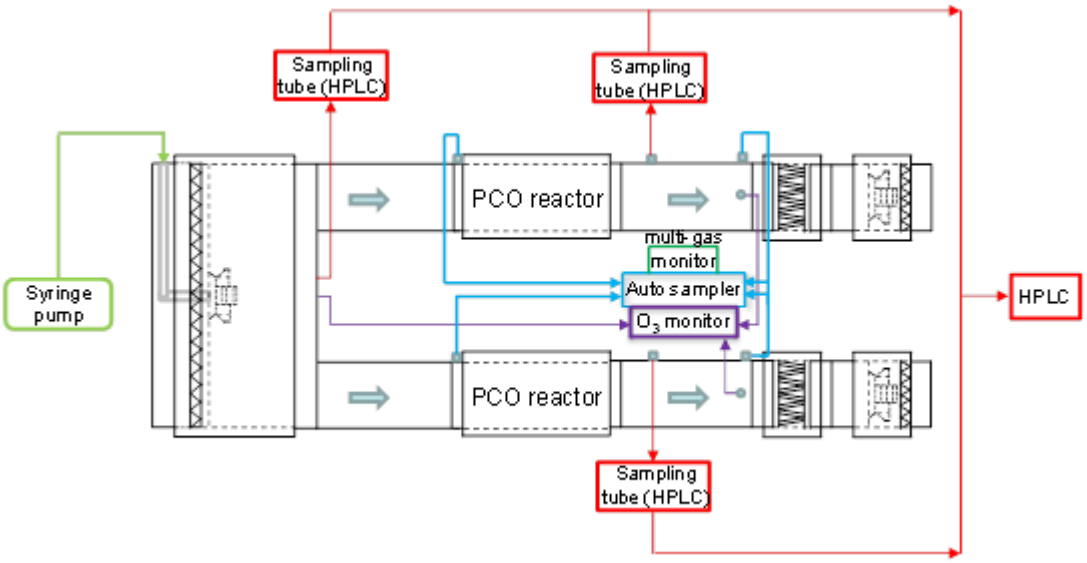

Figure 3-6 Schematic diagram of the testing system

3.3 Pre-Qualification Test

Qualification tests were conducted to quantitatively verify that the test rig is capable of providing reliable UV-PCO air cleaner efficiency measurements. Although some apparatus qualification tests are described by proposed draft of ASHRAE New Standard 145.2P, this test method is mainly aimed for assessing the performance of the sorptive media gas-phase air cleaning devices. These tests have to be modified for the UV-PCO air cleaners. The qualification testing of the test rig included:

1. The test ducts leakage test
2. The test ducts velocity uniformity
3. The concentration uniformity
4. The no filter test

3.3.1 Test Ducts Leakage Test

The test ducts leakage test was carried out without any devices installed inside the

duct system. According to the proposed draft of ASHRAE 145.2-2011, the duct pressures for the leak test are normally determined by adding to the duct operating pressures with 250 Pa (1 inch H_2O) under different airflow rates. Since the UV-PCO systems usually have a lower pressure drop than other adsorbent media beds, 250 Pa is a factor which can be added safely. Then the test duct was sealed, turning it into a closed system, by taping hardboards to the duct openings. Compressed air was carefully fed into the test duct until the aforementioned duct pressure was achieved. SF_6, a tracer gas, was injected into the four ducts system until it reached a certain concentration. A multi-gas detector was used to continuously measure the concentration of SF_6 inside the system. After the analysis, the air sample taken by the pump inside the detector was returned to the four-duct system in order to accurately evaluate the concentration decay. Figure 3-7 shows the schematic diagram of the test ducts system leakage test.

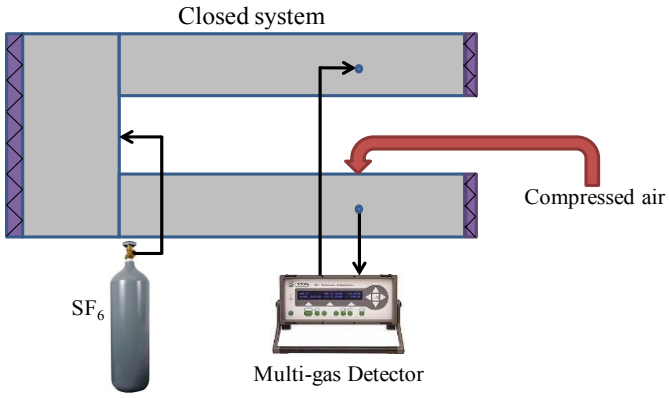

Figure 3-7 Diagram of the leakage test set up

Based on the well-mixed single zone model, the equilibrium equation of the compound SF_6 can be established as follows:

$$\frac{VdC}{dt} = -Q_{leak} \times C_{(t)} \quad (C=C_0 \text{ at } t=0)\ , \qquad [3\text{-}1]$$

Through integration, the mass balance can be written as:

$$C = C_0 \times e^{-\frac{Q_{leak} \times t}{V}}, \qquad [3\text{-}2]$$

where C (ppm) is the time dependent SF_6 concentration inside the duct (t, sec), C_0 (ppm) is the initial tracer gas concentration, V (m^3) is the volume of the closed system, and Q_{leak} (m^3/s) is the leak flow rate of the whole test rig.

The experiment was performed at an airflow rate for each duct approximately equal to 240 m^3/h (140 cfm). The total airflow rate was 960 m^3/h (567 cfm). The average duct pressure at this airflow rate was 177 Pa (0.708 inch H_2O). Hence, the duct pressure for the leak test was adjusted to around 425 Pa (1.7 inch H_2O) by metering with the compressed air. Figure 3-8 presents the SF_6 concentration decay inside the ducts.

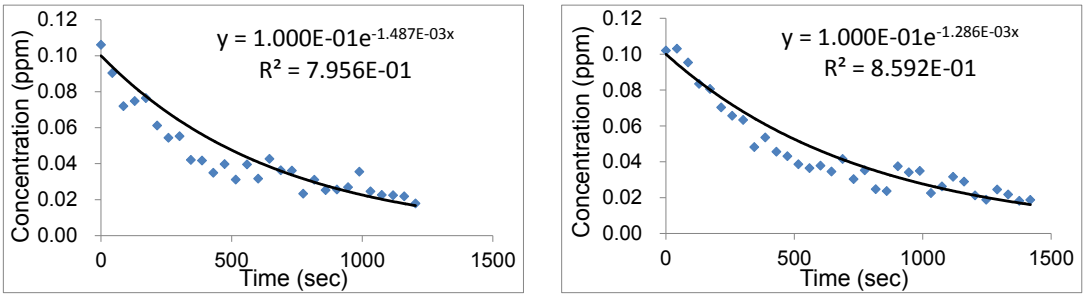

(a) **(b)**

Figure 3-8 SF_6 concentration decay with time: (a) the first test (b) the second test

The total volume of the closed part of the test rig was 1.67 m^3. Through Eq. (3-2), the computed air leakage flow rate was 8.94 m^3/h (5.26 cfm). Therefore, the leakage rate, 0.93%, did not exceed 1.0% of the test airflow rate of 963 m^3/h (567 cfm), satisfying the ASHRAE standard 145.2-2011. In addition, the whole procedure was performed again for assurance. The leakage rate of the second test was 0.80%,

indicating again that the leakage of the test system meets the required specification.

3.3.2 Test Ducts Velocity Uniformity

The velocity uniformity test standard proposed by the ASHRAE standard 52.2-1999 provides a good evaluation of the velocity uniformity inside a duct. Considering the size of each duct, 0.3 m by 0.3 m (12 inch by 12 inch), applied in the UV-PCO air cleaner, it is considerably smaller than that described in the standard, 0.6 m by 0.6 m (24 inch by 24 inch). Because of this, the traditional multi-point traverse airflow measurement techniques were not used here. The velocity was monitored by four electronic low flow probes (ELF-1200, EBTRON) installed inside each duct. Figure 3-9 shows the four ducts' positions at the right side view of the test rig.

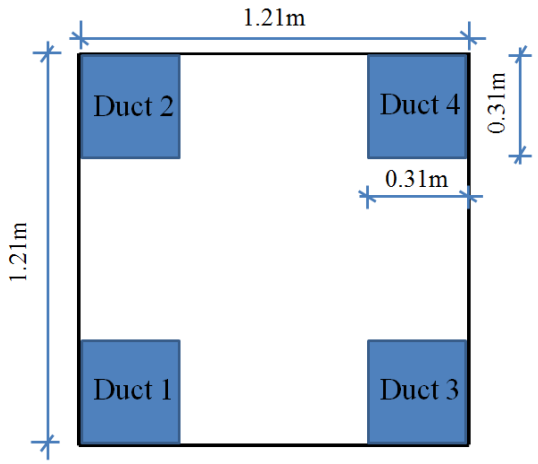

Figure 3-9 Location of each duct from back view

The velocity uniformity test is a prerequisite to guarantee that the contaminants are evenly dispersed into the four ducts. Also, the air velocity of each duct needs to be stable during the whole test period. The test was conducted at the airflow rates of 170 m^3/h (100 cfm) and 340 m^3/h (200 cfm).

12 samples were taken from each duct at 5-second sampling intervals for a period of one minute. This procedure was repeated three times. In addition, the velocity test procedure was repeated twice to validate the repeatability. Then the average of the three measurements was calculated for each duct. The coefficient of variation (CV), that is the velocity deviation of the four ducts divided by their average velocity, is used to evaluate the performance of the four-duct velocity. The results for 170 m^3/h (100 cfm) and 340 m^3/h (200 cfm) are presented in Tables 3-3, 3-4, 3-5, and 3-6, respectively.

Table 3-3 Velocity uniformity test at 170 m^3/h (100 cfm)

Duct Location	One-minute measurement	Velocity #1 (m/s)	Velocity #2 (m/s)	Velocity #3 (m/s)	Ave of three measurements
Duct 1	Max	0.556	0.561	0.562	------
	Min	0.532	0.542	0.537	------
	Ave	0.544	0.551	0.549	0.548
Duct 2	Max	0.598	0.587	0.590	------
	Min	0.567	0.561	0.572	------
	Ave	0.579	0.576	0.584	0.580
Duct 3	Max	0.566	0.557	0.562	------
	Min	0.547	0.545	0.540	------
	Ave	0.553	0.550	0.554	0.552
Duct 4	Max	0.556	0.568	0.565	------
	Min	0.531	0.538	0.545	------
	Ave	0.549	0.556	0.558	0.554
		AVE			0.559
		DEV			0.014
		CV			2.56%

Table 3-4 Velocity uniformity test at 170 m^3/h (100 cfm) (Repeated)

Duct Location	One-minute measurement	Velocity #1 (m/s)	Velocity #2 (m/s)	Velocity #3 (m/s)	Ave of three measurements
Duct 1	Max	0.550	0.546	0.553	------
	Min	0.532	0.526	0.531	------
	Ave	0.540	0.538	0.541	0.540
Duct 2	Max	0.576	0.574	0.579	------
	Min	0.560	0.555	0.561	------
	Ave	0.568	0.569	0.572	0.570
Duct 3	Max	0.557	0.547	0.555	------
	Min	0.525	0.530	0.535	------
	Ave	0.542	0.541	0.546	0.543
Duct 4	Max	0.559	0.554	0.556	------
	Min	0.531	0.535	0.536	------
	Ave	0.544	0.545	0.547	0.545
		AVE			0.549
		DEV			0.014
		CV			2.49%

Table 3-5 Velocity uniformity test at 340 m^3/h (200 cfm)

Duct Location	One-minute measurement	Velocity #1 (m/s)	Velocity #2 (m/s)	Velocity #3 (m/s)	Ave of three measurements
Duct 1	Max	1.143	1.140	1.147	------
	Min	1.086	1.093	1.094	------
	Ave	1.120	1.120	1.117	1.119
Duct 2	Max	1.136	1.127	1.131	------
	Min	1.112	1.100	1.083	------
	Ave	1.126	1.115	1.115	1.119
Duct 3	Max	1.166	1.162	1.143	------
	Min	1.127	1.125	1.107	------
	Ave	1.137	1.144	1.127	1.136
Duct 4	Max	1.169	1.146	1.128	------
	Min	1.101	1.097	1.095	------
	Ave	1.128	1.126	1.113	1.122
		AVE			1.124
		DEV			0.008
		CV			0.73%

Table 3-6 Velocity uniformity test at 340 m^3/h (200 cfm) (Repeated)

Duct Location	One-minute measurement	Velocity #1 (m/s)	Velocity #2 (m/s)	Velocity #3 (m/s)	Ave of three measurements
Duct 1	Max	1.130	1.130	1.147	------
	Min	1.075	1.062	1.052	------
	Ave	1.107	1.096	1.095	1.099
Duct 2	Max	1.088	1.127	1.117	------
	Min	1.033	0.984	1.036	------
	Ave	1.052	1.054	1.067	1.058
Duct 3	Max	1.131	1.123	1.130	------
	Min	1.104	1.091	1.084	------
	Ave	1.117	1.109	1.108	1.111
Duct 4	Max	1.103	1.088	1.103	------
	Min	1.023	1.030	1.035	------
	Ave	1.062	1.057	1.067	1.062
		AVE			1.083
		DEV			0.027
		CV			2.47%

In order to validate that the air velocity can be held constant in the case of a long-term testing, the air velocity of each duct was monitored for three days. Figure 3-10 shows that the air velocities were found to be stable.

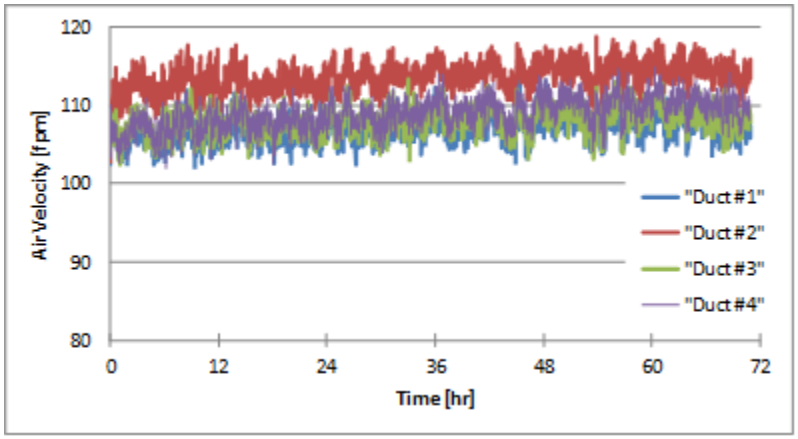

Figure 3-10 Air velocity stability test

3.3.3 Concentration Uniformity

To be able to compare the performance of the UV-PCO systems simultaneously, the experiments must be performed at an identical condition that means the pollutant concentration inside the four ducts must be the same. P-xylene was used as the challenge gas. P-xylene is relatively heavy and has a lower diffusion coefficient than that of lighter compounds, such as ethanol, acetone and so on.

The concentration uniformity test was conducted by generating p-xylene and measuring the concentration at the upstream and the downstream points of each duct. This test was carried out without any UV-PCO systems. The multi-gas analyzer INNOVA was coupled with the auto-sampler (CBISS MK3), which was programmed to alternatively and continuously take air samples from different sampling points to the gas detector. Since perforated cross-shaped tubes were connected to the corresponding sampling ports, the monitored concentrations from different sampling ports were the average concentrations in each duct. Before introducing the challenge gas, the background concentration of p-xylene at each duct was measured. Then p-xylene was injected into the PCO system, and the measurement was carried out for the two airflow rates of 170 m^3/h (100 cfm) and 340 m^3/h (200 cfm) for a period of almost 6 hours.

Figure 3-11 shows the p-xylene concentration in each duct at the airflow rate of 170 m^3/h (100 cfm) and Figure 3-12 shows the mean average concentration and the deviation for each duct. The CV, the ratio of the standard deviation to the mean average concentration of the four ducts, was found to be 0.65% for the first test. In

addition, the whole test was repeated, and the CV of 0.70% was derived for the second test.

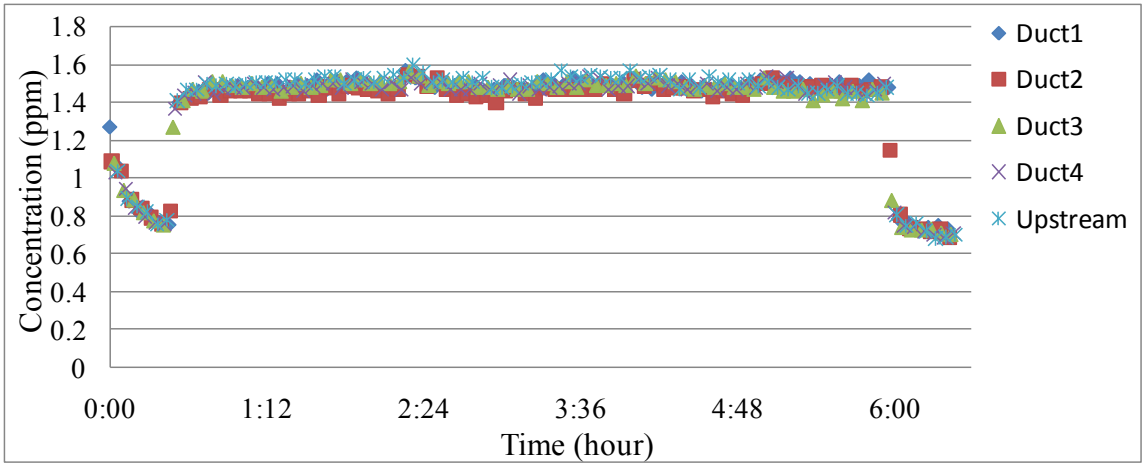

(a)

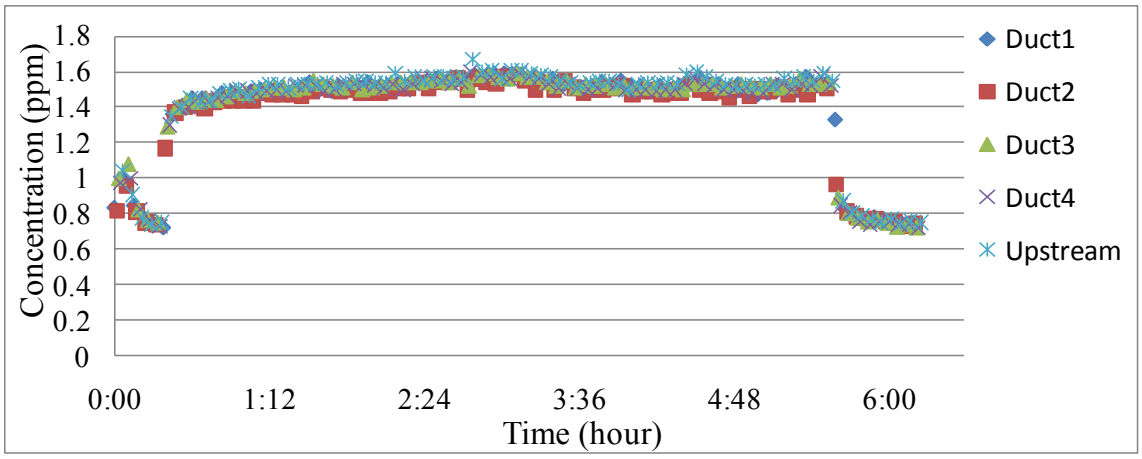

(b)

Figure 3-11 P-xylene concentration for each duct at flow rate of 170 m^3/h (100 cfm): (a) first test, and (b) repeated test

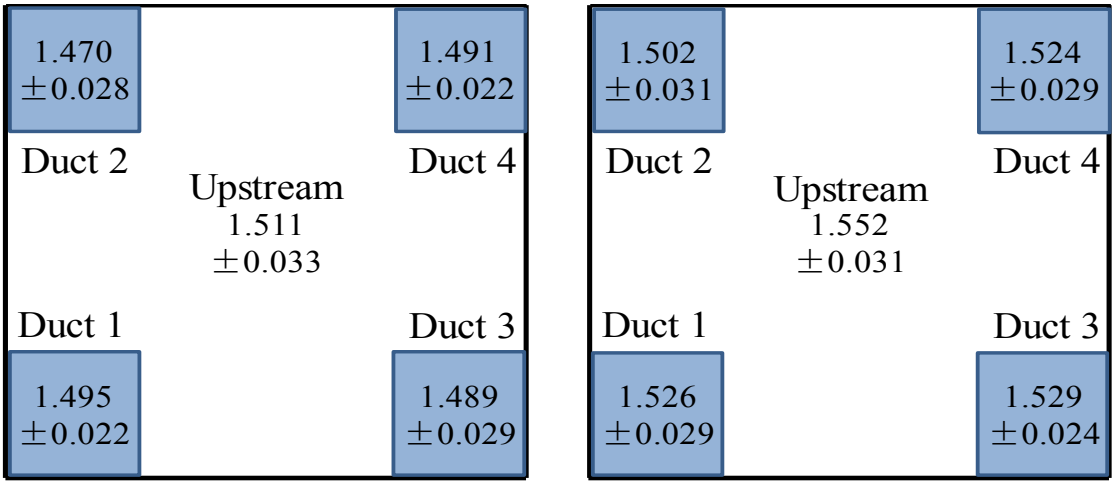

Figure 3-12 Mean average concentration and standard derivation for each duct at flow rate of 170 m^3/h (100 cfm): (a) first test, and (b) repeated test

Similarly, the concentration uniformity test at 340 m^3/h (200 cfm) was carried out twice. The CVs for both tests were found to be 1.23% and 1.16%, respectively. The p-xylene concentration for each duct is presented in Figure 3-13, and the mean average concentration and the standard derivation for each duct are shown in Figure 3-14.

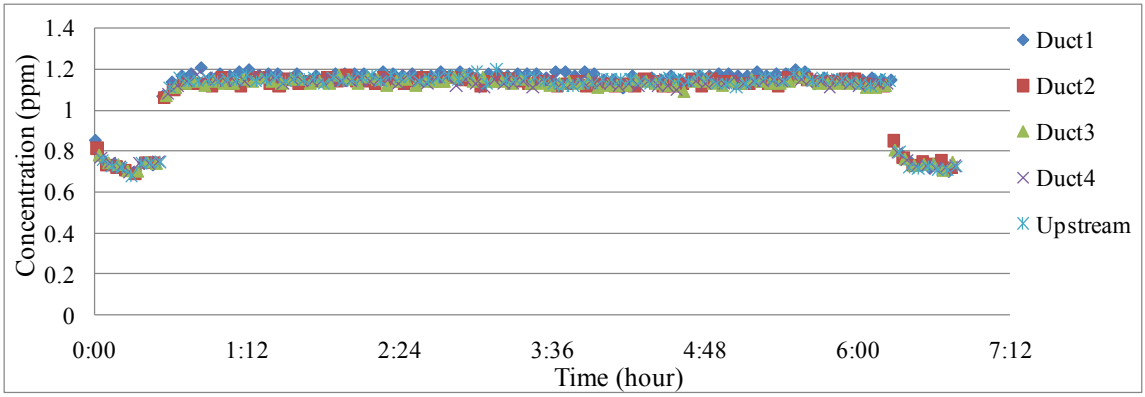

(a)

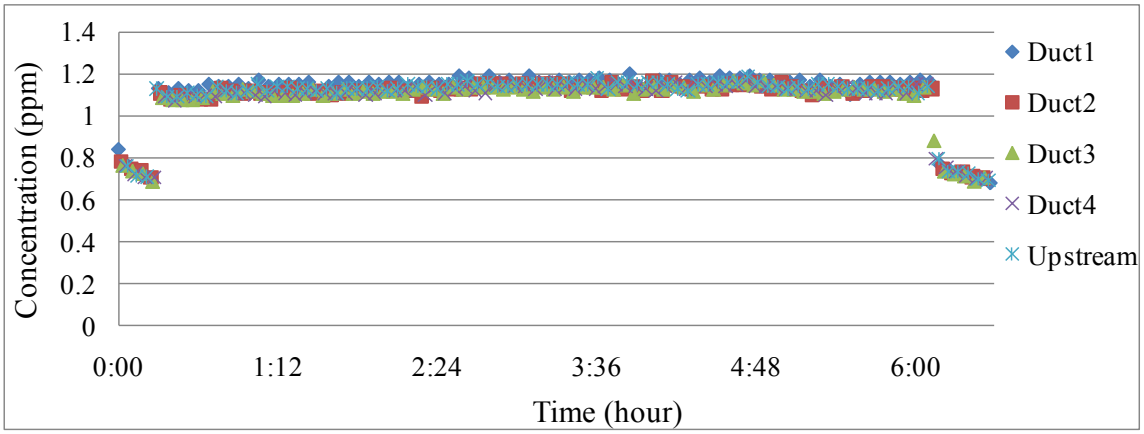

(b)

Figure 3-13 P-xylene concentration for each duct at flow rate of 340 m^3/h (200 cfm): (a) first test, and (b) repeated test

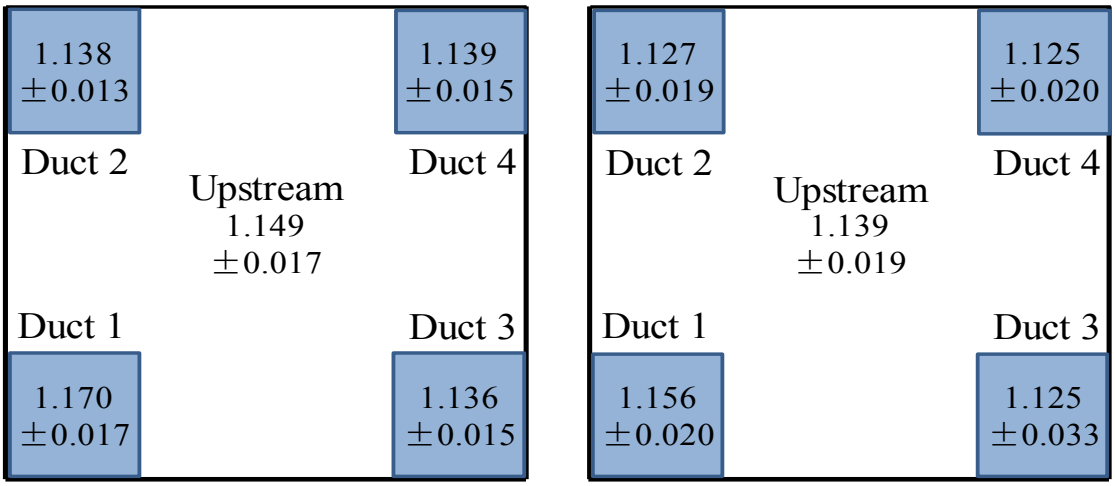

Figure 3-14 Mean average concentration and derivation for each duct at flow rate of 340 m^3/h (200 cfm): (a) first test, and (b) repeated test

3.3.4 No Filter (Sink/Leakage) Test

An upstream-downstream comparison test was performed to check the adequacy of the overall duct; this test was performed without a UV-PCO device. As there was no PCO filter installed, the calculated single-pass removal efficiency indicates a loss of the challenge gas, resultant from the leak and the sink effect.

Based on the results of the two concentration uniformity tests at the airflow rate

of 170 m^3/h (100 cfm) (the same experimental setup with no filter test), the calculated average removal efficiency was found to be 1.64% and 2.05%, respectively. Similarly, the calculated average removal efficiency for the two tests at the air flow rate of 340 m^3/h (200 cfm) was 0.28% and 0.50%., respectively. Hence, the combined leakage and sink effect of the test rig was determined to be insignificant.

3.4 Quantification Methods

The experimental data collected from the upstream and the downstream measurement ports is employed to calculate the effectiveness of a UV-PCO air cleaner. The photocatalytic oxidation reaction takes place immediately when the sample is exposed to the UV light. After the contaminant injection, the concentration of the contaminant increases until it reaches a stable condition. Single-pass efficiency, η_t (%), which is determined by the amount of the removed pollutant from the air stream after it goes through the air cleaner, is widely used to evaluate the performance of an in-duct air cleaner. It is defined as follows:

$$\eta_t(\%) = \frac{Q(C_{up,t} - C_{down,t})}{QC_{up,t}} \times 100 = \frac{C_{up,t} - C_{down,t}}{C_{up,t}} \times 100 \quad , \qquad [3\text{-}3]$$

where η_t (%) is the single-pass efficiency of a pollutant; $C_{up,t}$ (mg/m^3) is the contaminant concentration at upstream as a function of time; $C_{down,t}$ (mg/m^3) is the contaminant concentration at downstream as a function of time and Q (m^3/s) is the airflow rate through an air cleaner.

3.5 Major Findings

Since many tests had to be carried out, a new test rig, which consisted of four parallel ducts, was designed and constructed. To ensure that the rig was appropriate for the measurements of the UV-PCO system performance, various pre-qualification tests including the air leakage test, the air velocity uniformity and stability tests, the concentration uniformity test and the no-filter test were conducted. Detailed calibration of analytical instruments was also discussed. Major findings were found as follows:

(1) A novel UV-PCO system composed of four parallel aluminum ducts was designed and constructed in a time-efficient manner. This rig could be used to equitably and thoroughly evaluate UV-PCO technology under the conditions relevant to the actual applications.

(2) The analytical instruments for measuring the concentrations of VOCs, including the multi-gas analyzer and the HPLC, were calibrated. The calibration results indicated that these instruments could provide reliable concentration measurements in the UV-PCO system.

(3) Prequalification tests of the apparatus were conducted, including the air leakage test, the air velocity uniformity and stability tests, the concentration uniformity test and the no-filter test. The experimental results quantitatively verified that the test rig was capable of providing reliable UV-PCO air cleaner efficiency measurements.

(4) Qualification methods have been developed to systematically evaluate the

performance of UV-PCO technology for the application in mechanical ventilation systems.

4. EXPERIMENTAL EVALUATION OF UV-PCO SYSTEM

4.1 Introduction

In literature, significant research has been carried out to examine PCO technology for the treatment of gaseous contaminants (Jo and Park, 2004; Jeong et al., 2005; Boulamanti et al., 2008; Sleiman et al., 2009; Yu and Brouwers, 2009), and the results indicate that PCO technology possesses a perspective for indoor air treatment. However, majority of available PCO data are based on laboratory bench-top equipped with a small PCO reactor where experiments were carried out under ideal reaction conditions, i.e. low volumetric airflow rates, tested with one or a few compounds, etc. Therefore, the test results based on the ideal experimental conditions could be problematic and may not be scaled up to predict the performance of full-scale systems. Although some research has explored the feasibility of PCO technology applied in HVAC systems (Chen et al., 2005; Disdier et al., 2005; Hodgson et al., 2007), these applications are mainly aimed at designing a portable PCO air cleaner employed in a closed room or a chamber. To the best of our knowledge, the literature especially aiming to explore the PCO performance as a single-pass way employed in an HVAC system is limited.

The application of ozone-producing lamps in UV-PCO air cleaners inevitably introduces ozone into a duct system. Ozone is a very powerful and strong oxidant, which can be applied to air purification. In the past half century, kinetics and

mechanisms of the gas-phase reactions of ozone with organic compounds under conditions relevant to the atmosphere were well examined in the atmospheric science field (Atkinson and Carter, 1984). It was found that the action of O_3 is extremely selective, and O_3 usually plays a positive role to remove only alkenes and other organic compounds containing unsaturated carbons. It is worthwhile to mention that the conditions of their observations were close to the atmospheric environment, that is, O_3 mixing ratios were generally around 10-40 ppb at ground level. On the contrary, an O_3 concentration produced by VUV lamps is usually at ppm levels depending on the numbers of lights, relative humidity, and flow rates. Also, the physical phenomenon of ozonation in a dynamic system (moving flow) is different from a static chamber system. To the best of our knowledge, no study has been carried out on the investigation of ozonation effects for a variety of compounds using a pilot duct system, which is one of the contributions of this study.

Standard test methods for air cleaning systems are mainly for measuring particulate removal without the concerns of ozone generation. ASHRAE has been developing test methods for gaseous pollutant removal; however, these are mainly applicable for sorbent media like activated carbons. The principal objective of this research is to develop methodologies to evaluate the performance of the UV-PCO systems for the IAQ applications. Therefore, this chapter demonstrates a systematic evaluation of the in-duct UV-PCO air cleaners equitably and thoroughly under the conditions relevant to the actual applications for a wide range of VOCs.

4.2 Experimental Methodology

4.2.1 Challenge Gas

Many studies have reported that more than 170 VOCs can be detected in a typical indoor environment. Therefore, it is critical to use diverse VOCs to study the performance of PCO. In this study, we follow the recommendations of VanOsdell (1994) to select the representative VOCs:

- The tested VOCs are very easy to be found in the indoor environment and have a certain degree of representative of indoor air contaminants,
- The tested VOCs have different physical natures and belong to different chemical classes,
- The tested VOCs should not have any serious health risks and can be worked safely in the absence of special protection, and
- The analytical tools of the tested VOCs are simple, and the cost of the tested VOCs is reasonable.

Therefore, toluene, p-xylene, ethanol, 1-butanol, acetone, 2-butanone (MEK), n-hexane, octane are chosen as representative of indoor air contaminants, in which they respectively pertain to aromatics, alcohols, ketones, and alkanes. Table 4-1 shows the physical properties of these compounds. In addition, due to the differences of the chemical structures of these chemicals, some groups may be easily transformed to other groups during the photochemical process, while other function groups, such as ring structures, may be difficult to be transformed. The selected chemical classes are

appropriate challenge VOCs to fully evaluate the performance of PCO technology.

Toluene, p-xylene, ethanol, 1-butanol, acetone, MEK, n-hexane, and octane are widely used as common solvents, and are able to dissolve many substances. Thus, they are frequently found in household products, such as painted wallboard, composite woods, carpeting, painted gypsum, and vinyl flooring. In addition, toluene, n-hexane and MEK are in the list of VOCs challenge gas recommended by the ASHRAE standard 145.1-2008 to comprehensively test air cleaning devices. The eight chemicals show no carcinogenic or mutagenic properties. The details of possible emission sources, potential health effects and reported concentrations of the tested VOCs are shown in Table 4-2.

During the past 20 years, the eight selected chemicals have widely been studied by researchers (Litchin et al., 1996; Luo and Ollis, 1996; Einaga et al., 2002; Ginestet et al., 2005; Kirchnerova et al., 2005; Yu et al., 2006; Boulamanti et al., 2008; Guo et al., 2008; Hernandez-Alonso et al., 2009). However, most of studies dealt with only one or two of these chemicals and no general conclusions were drawn from these studies since different species behaved differently at various experimental conditions. Hence, a systematic and comprehensive study of the PCO efficiency on these contaminants is critical to understand fully the physiochemical kinetics in the PCO process.

Table 4-1 Physical properties of the selected VOCs (NIOSH, 2010)

Chemical	VOCs Class	Molecular Formula	Molar Mass (g/mol)	Density (g/mL)	Boiling Point (℃)	Vapor Pressure (mmHg)	Solubility (at 20-25℃)	Dielectric Constant (at 20-25℃)
Toluene	Aromatics	C_7H_8	92.1	0.8669	111.1	21	0.07%	2.38
p-Xylene		C_8H_{10}	106.2	0.86	138.3	9	0.02%	2.2
Ethanol	Alcohols	C_2H_6O	46.1	0.789	78.4	44	miscible	24.3
1-Butanol		$C_4H_{10}O$	74.1	0.802	117.2	6	9%	16.68
Acetone	Ketones	C_3H_6O	58.1	0.7925	56.1	180	miscible	20.7
MEK		C_4H_8O	72.1	0.8050	79.4	78	28%	18.51
n-Hexane	Alkane	C_6H_{14}	86.2	0.6548	68.9	124	0.002%	1.88
Octane		C_8H_{18}	114.2	0.703	125.6	10	0.00007%	1.94

Note: Water (very polar) has a dielectric constant of 80.10 at 20℃.

Table 4-2 Possible emission sources, potential health effects and reported concentrations of the tested VOCs (Namiesnik et al., 1992; Nagda and Rector, 2003; Geiss et al., 2011; NIOSH, 2010)

Chemical	Source Materials	Reported air quality (μg/m^3)			Potential Health Effects
		Aircraft	Residential	Office	
Toluene	Paints, adhesives, gasoline, combustion products	6.8-68	37-320	5.7-58	Disorders or diseases of the skin, eye, liver, kidney, nervous system, respiratory and/or pulmonary system, lung.
p-Xylene		2.5-5.0	18-120	4.6-37	Disorders of the skin, respiratory and central nervous system.
Ethanol	Aerosols, window cleaners, paints, paint thinners, cosmetics and adhesives	324-1116	120-490	---	Causes severe eye irritation and moderate skin irritation. Disorders of kidneys, heart, central nervous system, liver.
1-Butanol		---	0.4-9.8	0.3-41.4	Causes irritation to eyes, skin and respiratory tract. Affects central nervous system.
Acetone	Lacquers, vanishes, polish removers, adhesives	40.8-58.9	10.4-165.1	1.4-336.8	Causes irritation to eyes, skin and respiratory tract. Affects central nervous system.
MEK		2.5-10.0	---	---	Causes irritation to nose, throat, eyes, skin and respiratory tract. Disorders of lung.
n-Hexane	Paints, adhesives, gasoline, combustion products	---	0.2-78.4	0.3-33.3	Causes irritation to eyes, skin and respiratory tract. Disorders of lung, central and peripheral nervous system.
Octane		---	8.8-32.7	7.7-32.8	Respiratory tract irritation, skin irritation, eye irritation, central nervous system depression

4.2.2 Materials

Eight reagent grade chemicals cover major chemical categories and have a wide range of different physical properties such as molecule weight and polarity. They included toluene (99.9%), p-xylene (99.9%), 1-butanol (99.9%), n-hexane (96%), octane (95%), MEK (99.9%), and acetone (99.5%) from Fisher Scientific Inc. (Canada), and ethanol (99%) from SAQ (Société des alcools du Québec - Québec Alcohol Board). Other HPLC grade chemicals used for HPLC analysis include methanol (99.9%) and acetonitrile (99.9%) from Fisher Scientific Inc. (Canada).

Ultra high purity (99.999%) nitrogen and helium from Praxair Canada Inc. were used as carrier gases for GC/MS analysis. Compressed sulfur hexafluoride (1.07 ppm) from Matheson Inc. was used as a tracer gas for the leakage test.

The water used for the analytical instrument calibration and adsorption tests was deionized water filtered with a Milli-Q system (Millipore Inc.).

4.2.3 Experimental Conditions

4.2.3.1 VOCs Concentration

The target concentration of the selected challenge gases was a sub-ppm level (0.25 - 2 ppm) to represent real indoor air pollution conditions. Table 4-3 shows concentrations of each compound in units of mg/m^3 at expected inlet conditions.

Table 4-3 Target VOCs concentrations

VOC	Syringe Pump System		
	0.25 ppm	**0.5 ppm**	**1 ppm**
Toluene	0.94 mg/m^3	1.89 mg/m^3	3.77 mg/m^3
p-Xylene	1.10 mg/m^3	2.21 mg/m^3	4.41 mg/m^3
Ethanol	0.47 mg/m^3	0.95 mg/m^3	1.89 mg/m^3
1-Butanol	0.76 mg/m^3	1.52 mg/m^3	2.42 mg/m^3 (0.8 ppm)
Acetone	1.19 mg/m^3 (0.5 ppm)	2.38 mg/m^3 (1 ppm)	4.76 mg/m^3 (2 ppm)
MEK	0.74 mg/m^3	1.48 mg/m^3	2.95 mg/m^3
Hexane	0.88 mg/m^3	1.77 mg/m^3	3.53 mg/m^3
Octane	1.17 mg/m^3	2.34 mg/m^3	4.67 mg/m^3

4.2.3.2 In-duct Air Flow Rate

The UV-PCO experiments were carried at the airflow rates ranging from 43 m^3/h (25 cfm) to 255 m^3/h (150 cfm), where the corresponding face velocity ranged between 0.12 m/s and 0.75 m/s. Four electronic low-flow probes (ELF-1200, EBTRON), based on the thermal dispersion technology, were used to accurately measure the airflow rates in four ducts. They had 0-10 VDC linear output signals and measured the airflow rates in the range of 0-500 fpm. The accuracy of air flow rate measurement was ±1.3%.

4.2.3.3 UV Light Intensity

Figure 4-1, provided by the manufacturer (Ster-L-Ray, Atlantic Ultraviolet Inc.), shows the UV lamp characteristics. Approximately 95% of the ultraviolet energy emitted from germicidal lamps is at the mercury resonance wavelength of 254 nm, while the relative irradiance of the other wavelengths of interest, such as 313 nm and 365 nm, is considerably small. Ozone producing lamps, in addition to emitting germicidal ultraviolet

output at 254 nm, also emit ozone producing rays at 185 nm, around 5% of the UV energy emitted at 185 nm. Hence, these UV lamps (with or without ozone producing) can be regarded as monochromatic light sources. In addition, the UVC output usually decreases over time and after 6,000 hours of work it may reduce to 80% of the initial UVC output. Moreover, the UVC output varies with the bulb wall temperature and the maximum UVC output can be reached when the bulb wall operates about 42℃.

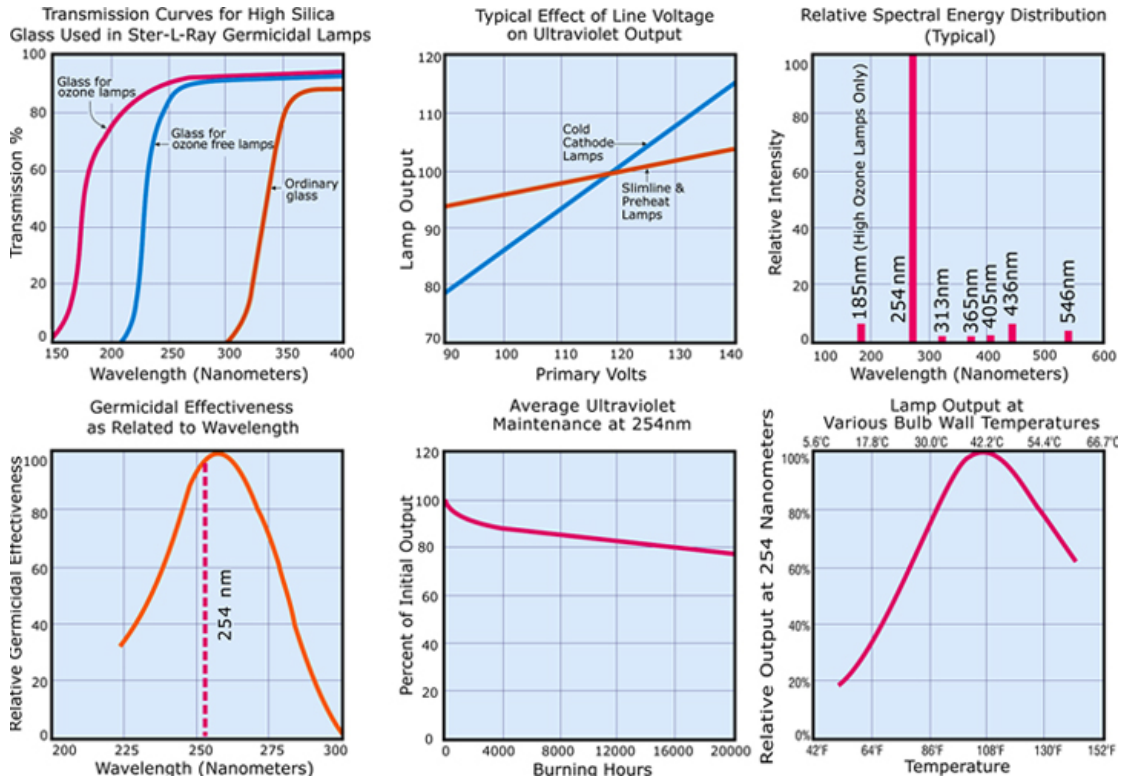

Figure 4-1 Characteristics of a UV lamp (provided by Atlantic Ultraviolet Inc.)

There were four layouts of UV lamps in this study and the geometry dimensions are presented in Figure 4-2. Through varying the numbers of UV lamps, the irradiance reaching to the surface of the catalyst was different, and thus various PCO behaviors could be examined. Also, the ozone concentration within a duct was changeable by arranging the numbers of VUV lamps. Consequently, the ozonation effects on the

removal of VOCs could be studied.

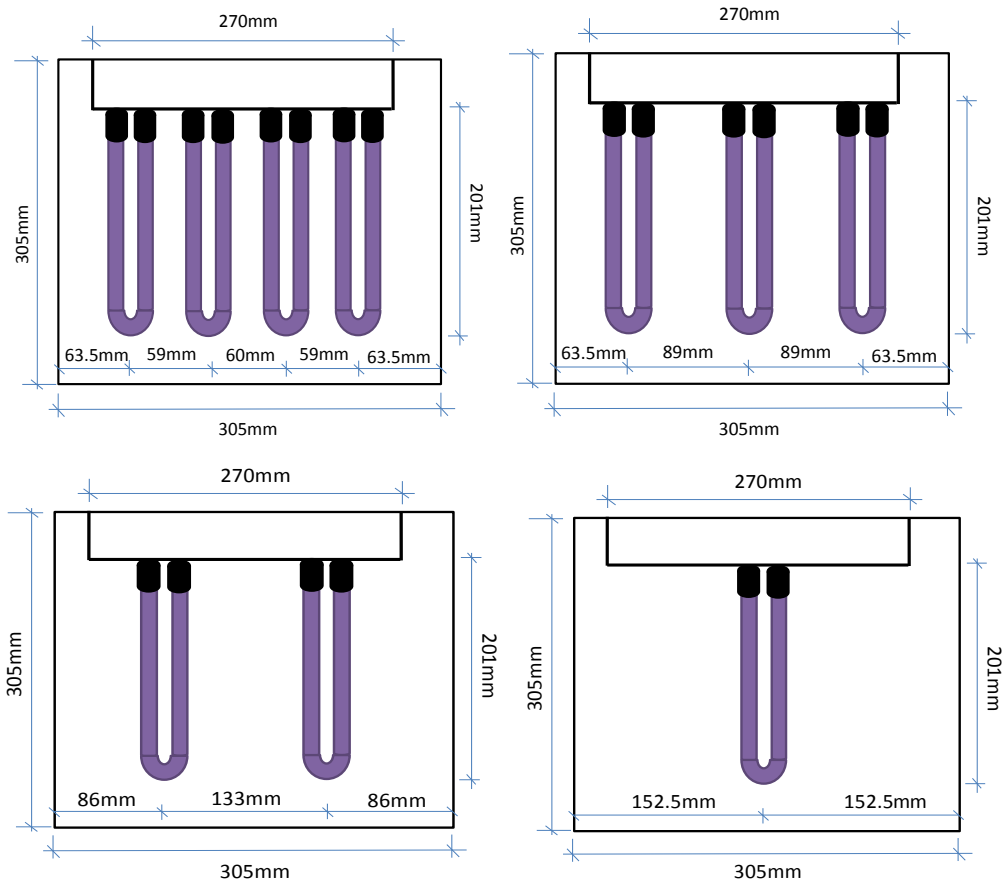

Figure 4-2 Various arrangements of UV lamps

The irradiance of 254 nm on the surface of TiO_2 filter was monitored by a UV radiometer (Steril-Aire) whose calibration was traceable to the National Institute of Standards (NIST). The radiometer sensor was fixed by a steel wire mesh frame, and the vertical distance between the sensor and the UV lamp surface was the same as that between the catalyst surface and the UV lamps. The area of the steel wire frame was evenly divided into 36 small lattices of 5.1 cm×5.1 cm (2 inch×2 inch). The locations of nine irradiance measurement ports were equally arranged at the center of the mesh frame. The distances between different testing points are shown in Figure 4-3. The average of nine irradiance values represented the average irradiance on the surface of the PCO filter.

During the UV-PCO tests, a UV radiometer sensor facing the UV lamps was located at the corner of each duct to continuously measure the irradiance emitted from UV lamps. Park (2004) reported that the illuminance ratio of two arbitrary surfaces in a space in the presence of one initial light source with varying quantity at a fixed location is always constant. According to this conclusion, the average irradiance on the catalyst surface for each test can be correctly estimated when the relationship of readings at various positions is known. Table 4-4 shows the relationship between readings measured at 5.1 cm (2 inch) vertical distance away from the catalyst and readings at the corner. From the tested results, the linear coefficient of duct#1 and duct#3 (contain the same type of air filters (TiO_2/FGFs) was 1.8 and 1.7, respectively, which further supports Park's findings.

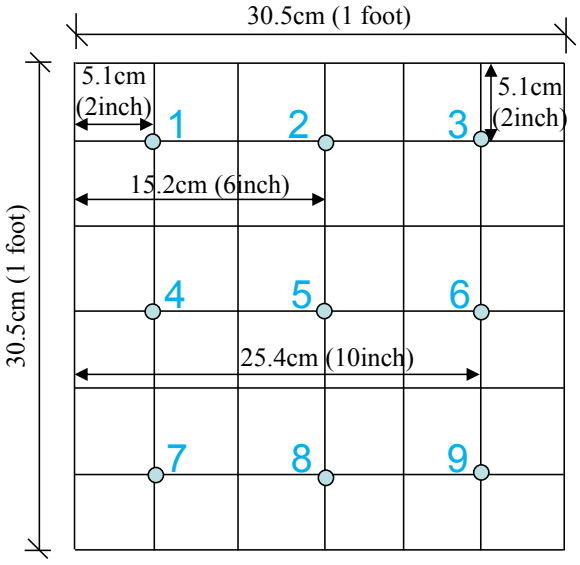

Figure 4-3 Grid to measure the irradiance

Table 4-4 Relationship of UV sensor readings at various locations

Duct No.	Sensor position	Measurement point (mW/cm^2)										Linear coefficient
		1	2	3	4	5	6	7	8	9	Ave	
Duct1	5 cm	0.20	0.13	0.20	7.66	4.04	5.99	3.36	2.06	2.02	2.85	1.8
	corner	1.53	1.52	1.62	1.54	1.48	1.47	1.55	1.64	1.59	1.55	
Duct3	5 cm	0.71	0.12	0.34	7.60	3.28	8.08	2.39	1.71	3.80	3.11	1.7
	corner	1.78	1.81	1.77	1.81	1.82	1.80	1.78	1.82	1.81	1.80	
Duct4	5 cm	0.38	0.13	0.38	6.33	3.97	7.68	4.20	2.10	3.24	3.15	2.6
	corner	1.21	1.22	1.19	1.22	1.23	1.17	1.18	1.20	1.19	1.20	

4.2.3.4 Ozone Level

A VUV lamp generates 185 nm ultraviolet light, which has sufficient energy to break oxygen into atomic oxygen. Single oxygen atom is highly unstable species, and thus rapidly combines with oxygen to form ozone. The chemical reactions are as follows:

$$O_2 + h\nu\ (\lambda < 243\ nm) \rightarrow O(^1D) + O(^3P) \quad [4\text{-}1]$$

$$O(^1D) + M \rightarrow O(^3P) + M\ (M = air) \quad [4\text{-}2]$$

$$O(^3P) + O_2 + M \rightarrow O_3 + M \quad [4\text{-}3]$$

In this study, the ozone level was measured by a calibrated 6-channel ozone monitor (Model 465L, Teledyne Inc.) based on absorption of 254 nm UV light due to an internal electronic resonance of the O_3 molecules. Ozone reading, calculated on the basis of the Beer-Lambert Law, had an accuracy of $\pm$0.1% for the full scale range. Four channels connected to the each downstream to measure the ozone concentration in each duct; one channel connected to the upstream of the PCO system to account for the VOCs interference effects; one channel connected to the exhaust of the PCO system to examine the lifetime of the ozone scrubber filter. The ozone analyzer was programmed to

alternatively and continuously take samples from six channels.

The ozone output strongly depends on the number of VUV lamps, oxygen and moisture levels, and airflow rates in a duct. The optimal conditions for ozone production are 20℃ still air supplied by a compressor (oil-less) with an air dryer (provided by the UV lamp manufacture). It is found that the formation of ozone is to some extent inhibited in the presence of water vapor in air. Figure 4-4 presents the relationship between the ozone concentration generated from 3 VUV lamps and RH of the air stream passing through these lamps: the higher the RH is, the lower ozone production is.

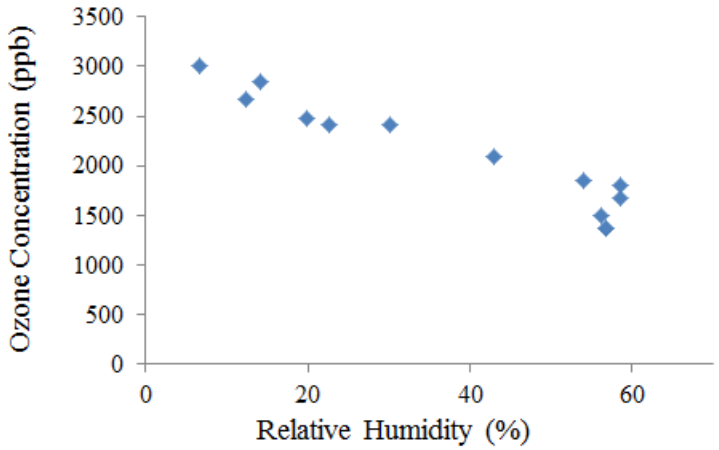

Figure 4-4 Ozone output vs. RH

Figure 4-5 shows the measured ozone concentration and irradiance of 254 nm vs. time in a duct at airflow rates of 170 m^3/h with three VUV lamps. For both cases, the stable ozone concentration and irradiance were observed after the VUV lamps were turned on for less than five minutes. The ozone concentration and the irradiance were kept steady for the duration test. Hence, the performance of UV-PCO is evaluated when these parameters reach the stable conditions; the effect of the initial few minutes is not considered in this study.

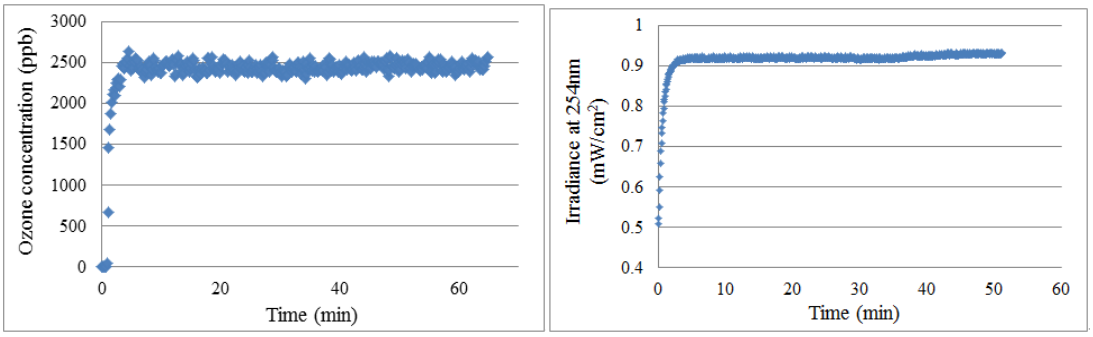

(a) (b)

Figure 4-5 (a) Ozone concentration vs. time (b) Irradiance of 254 nm at around 1 m away from UV lamps vs. Time

4.2.3.5 Temperature and Relative Humidity

Five Vaisala HUMICAP® humidity and temperature transmitters (HMT100 Series) were used to measure the relative humidity and temperature at one upstream zone and at four downstream zones. The probes were mounted at the center of the ducts. Real-time data display for each channel was provided by the Bench-Link Data Logger software and was transferred to a computer. The temperature sensor had an accuracy of ±0.17℃, and the RH sensor had an accuracy of ±0.17% RH. The RH and temperature were not controlled and experiments were carried out at room conditions. The range of RH and temperature in this study was 10-60% and 20-25℃, respectively. Due to the high airflow velocity (0.12-0.75 m/s) and short gas retention time (<2 s), the temperature of the air passing through the PCO reactor did not increase significantly.

4.2.3.6 Pressure Drop

The differential pressure between the upstream and the downstream locations was monitored by a micromanometer (DP-CALC^{TM}, Model 5825). Average of 5 readings was

taken as a result. The pressure measurements had a resolution of 0.1 Pa (0.001 inch H_2O) and an accuracy of ±1 Pa (0.005 inch H_2O).

4.2.4 Experimental Procedure

The three-step injection procedure was developed and adopted for all UV-PCO tests, which included the following details. First, the preparation work contained calibration of the air sampling pumps and the sampling cartridges, and calibration of the online multi-gas monitor for the selected compounds. Meanwhile, the sampling and measurement system was established by placing the sampling lines and sampling pumps in positions and connecting KI (potassium iodide) ozone scrubbers in the sampling lines, setting up the real-time test system to monitor the airflow rate, temperature, and RH in each duct, setting up the online measurement system to monitor the VOCs and ozone at upstream and downstream of each duct, and setting up an appropriate contaminant generation system.

Second, the proper PCO filters and UV lamps were installed in the designated position in each PCO reactor. The fans were turned on and were set at an appropriate airflow rate; the multi-gas analyzer and the ozone monitor were turned on to measure the background for 30 minutes; and then UV lamps were switched on to get a stable UV output. When the experimental conditions became stable, the PCO reaction could be initiated by first injection of a challenge VOC with an appropriate injection rate, and the real-time concentration was recorded by the online measurement system. Once the steady-state condition was reached, DNPH samples were taken at sampling rate of 1.3 L/min for 1.5 hours to explore the generation of by-products. For all compounds at inlet concentration of 500 ppb, DNPH samples were taken twice in four ducts to check the

repeatability of by-products. Upon DNPH sampling completion, the UV-PCO test was ended by stopping the injection while the measurement was continued. Then the UV-PCO test was repeated with second injection and third injection. In order to avoid catalyst deactivation resulting from the high concentration, the order of injection rate was in accordance with the expected concentration from low to high. The whole duration of a UV-PCO test for a VOC with three concentration levels lasted approximate 10 hours.

Before starting of a UV-PCO test for another VOC, each set of PCO filters was irradiated under UV lamps with fans running for a period of around 10 hours to regenerate the catalyst and to remove the residue compounds in the PCO system. Table 4-5 lists a series of the UV-PCO tests performed in this study.

Table 4-5 Summary of tests performed in the pilot duct system

Chemical Category	Test Compound	Test Date	Test Concentration (ppb)	RH	T (℃)	Flow rate (m^3/h) (cfm)	Note
Alcohols	Ethanol	07/05/12	250,500,1000	15	25	170 (100)	Inlet Concentration effect
	1-Butanol	11/05/12	250,500,800	19	25	170 (100)	Inlet Concentration effect
Alkanes	Hexane	14/05/12	250,500,1000	32	25	170 (100)	Inlet Concentration effect
	Octane	16/05/12	250,500,1000	43	25	170 (100)	Inlet Concentration effect
Ketones	MEK	18/05/12	250,500,1000	22	25	170 (100)	Inlet Concentration effect
	Acetone	23/05/12	500,1000,2000	44	24	170 (100)	Inlet Concentration effect
Aromatics	p-Xylene	28/05/12	250,500,1000	34	24	170 (100)	Inlet Concentration effect
	Toluene	30/05/12	250,500,1000	45	21	170 (100)	Inlet Concentration effect
Alcohols	Ethanol	03/04/12	500	9	22	170 (100)	RH effect
		07/05/12	500	15	25	170 (100)	
		09/05/12	500	43	25	170 (100)	
		01/06/12	500	30	22	170 (100)	
		21/06/12	500	56	21	170 (100)	
Ketones	Acetone	23/05/12	500	44	24	170 (100)	RH effect
		26/06/12	500	50	22	170 (100)	
Aromatics	Toluene	30/05/12	500	45	21	170 (100)	RH effect
		02/07/12	500	55	22	170 (100)	
Alkanes	Hexane	14/05/12	500	32	25	170 (100)	RH effect
		04/07/12	500	57	22	170 (100)	
Alcohols	Ethanol	09/06/12	250,500,1000	37	21	170 (100)	Ozonation effect
	1-butanol	11/06/12	250,500,800	56	21	170 (100)	Ozonation effect

Chemical Category	Test Compound	Test Date	Test Concentration (ppb)	RH	T (℃)	Flow rate (m^3/h) (cfm)	Note
Alkanes	Hexane	12/06/12	250,500,1000	57	21	170 (100)	Ozonation effect
	Octane	13/06/12	250,500,1000	53	21	170 (100)	Ozonation effect
Aromatics	p-Xylene	14/06/12	250,500,1000	37	21	170 (100)	Ozonation effect
	Toluene	15/06/12	250,500,1000	37	21	170 (100)	Ozonation effect
Ketones	MEK	17/06/12	250,500,1000	56	22	170 (100)	Ozonation effect
	Acetone	19/06/12	500,1000,2000	57	21	170 (100)	Ozonation effect
Alcohols	Ethanol	09/05/12	500	43	25	127 (75),255 (150)	Flow effect
		22/06/12	500	53	22	170 (100),77 (45), 43 (25)	
Ketones	Acetone	26/06/12	500	50	22	170 (100),77 (45), 43 (25)	Flow effect
Aromatics	Toluene	02/07/12	500	55	22	170 (100),77 (45), 43 (25)	Flow effect
Alkanes	Hexane	04/07/12	500	57	22	170 (100),77 (45), 43 (25)	Flow effect
Alcohols	Ethanol	22/07/12	500	56	21	170 (100)	Irradiance effect
Alkanes	Hexane	22/07/12	500	57	21	170 (100)	Irradiance effect
Ketones	Acetone	23/07/12	500	57	21	170 (100)	Irradiance effect
Aromatics	Toluene	23/07/12	500	60	22	170 (100)	Irradiance effect

4.3 UVC Photolysis

UVC Photolysis is a chemical reaction that takes place under the UVC irradiance without the presence of a catalyst. In this part, the objective was to examine whether the VOCs could be broken down into smaller molecules through the absorption of UVC light. The experimental setup included only three UVC lamps in the center of the duct system without any PCO filter installed (Figure 4-6). The photolysis experiments were carried out at the airflow rate of 170 m^3/h. UVC photolysis of the selected VOCs was separately investigated. However, for all VOCs tested, the results indicated that UVC irradiance itself could not definitely remove VOCs. Hence, the energy of 254 nm was not sufficiently high to break down C-C or C-H bonds. In other words, the direct photolysis with 254 nm UV radiation was negligible and the majority of the VOCs was unreacted.

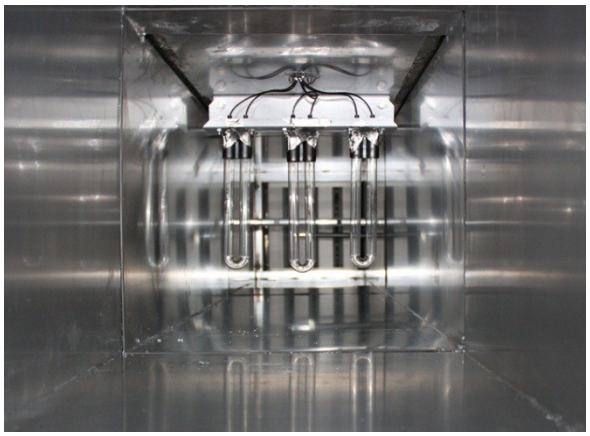

Figure 4-6 Photolysis test setup

4.4 VUV Ozonation

In this section, four ozone concentration levels were established by placing different numbers of lamps in each duct. Eight types of single compound with three inlet concentration levels were employed to explore the ozonation effects using the same

methodology described in section 4.2.4. Figure 4-7 shows the single-pass removal efficiencies of ozone with similar concentrations for various compounds at the 170 m^3/h (100 cfm) airflow rate in the absence of any PCO filter. It clearly shows acetone and MEK were scarcely removed by O_3. This low reactivity in the reaction is due to the weaker electron withdrawing power of the carbonyl group compared to the hydrocarbons. Hence, ketones react with ozone much less readily than the other compounds do. In a duct system, the effect of ozonation on the elimination of ketones is negligible. The results also indicate ozone reacted readily with the heavier compounds in the same class resulting in higher removal efficiency, especially for aromatics. For toluene and p-xylene with similar inlet concentrations, the single-pass removal efficiency of ozone for p-xylene was around twice of toluene. This is consistent with the results reported by Bailey (1982) that the rate of ozone attack on substituted benzenes increases with increasing alkyl group substitution. Moreover, these results further show that under the condition of a constant ozone concentration, an increased concentration of a challenge compound reduced significantly the ozone removal efficiency. A fast reaction of hydroxyl radicals with compounds can be observed, which implies that highly reactive hydroxyl radicals generated from photolysis of ozone are a key reaction species during the ozonation (Bailey, 1982).

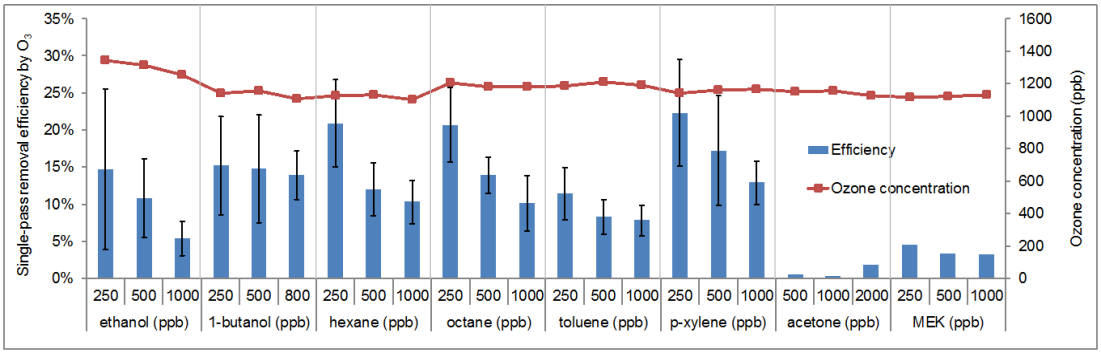

Figure 4-7 Single-pass removal efficiencies of various compounds at three concentration levels by ozone (RH=35%-58%)

Figure 4-8 shows that the conversion rates of various reagents increased with ozone concentrations. This can be explained by the fact that the higher single-pass removal efficiencies are reached at higher ozone concentrations where more hydroxyl radicals are available to enhance gas-phase photochemical reactions. However, ozone itself is a problematic by-product that may threaten building occupants' health seriously through harming the lung function and irritating the respiratory system. Therefore, it is extremely necessary to add an ozone filter to remove excess ozone after a VUV-PCO air cleaner in the air supply system.

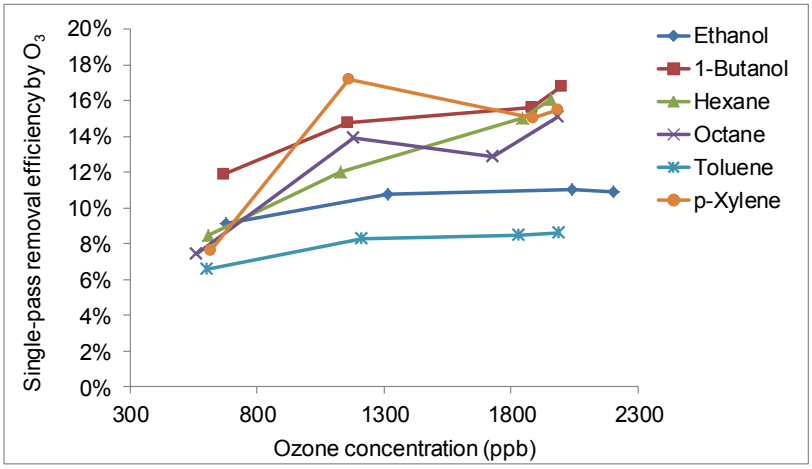

Figure 4-8 Ozone concentration versus single-pass removal efficiency for various compounds (initial concentration=500 ppb)

4.5 Adsorption Performance

4.5.1 Introduction

Usually, the values of adsorption coefficient were determined by fitting a kinetic PCO model with experimental data (Bouzaza et al., 2006; Shiraishi and Ishimatsu, 2009; Sleiman et al., 2009). In fact the values derived from a kinetic study are usually much higher than those obtained from the Langmuir adsorption isotherm in the absence of light (Mills and Hunte, 1997). In a few articles relevant to the adsorption isotherms (Demeestere et al., 2003; Tomida et al., 2005; Chen et al., 2011; Maudhuit et al., 2011), the adsorption performance was examined with a limited number of compounds of interest, such as toluene, acetone, and trichloroethylene. Moreover, the effect of relative humidity on adsorption isotherms has not been fully examined. To the best of our knowledge, no systematic studies have been conducted with respect to an adsorption phenomenon of a photocatalyst for a wide range of VOCs. Also research on the adsorption properties of a photocatalyst placed on various substrates is limited.

Experimental determination of adsorption coefficient is a basic research for UV-PCO technology since the adsorption coefficient is a critical parameter that influences the surface coverage of adsorbed compounds, thereby affecting the photocatalytic oxidation rate. In this section, the adsorption performance of TiO_2 loaded on two different substrates, fiberglass fibers (FGFs) and carbon cloth fibers (CCFs) was experimentally investigated. For the FGFs, this section demonstrates a systematic evaluation of adsorption performance at various humidity conditions (9.6±0.6% - 70.2±2.7%) for eight compounds. The challenge air concentrations of each selected compound were from 0.5 ppm to 5 ppm. For the CCFs with and without TiO_2 coating, ethanol and hexane were

employed to examine the adsorption performance, as a typical polar and a non-polar reagent, respectively, and at various humidity conditions. This section provides a profound insight into the basic knowledge of TiO_2 adsorption mechanism, helps to determine the values of adsorption coefficients for a PCO modeling, and further reveals that the adsorption behavior is closely related to the characteristics of substrates.

4.5.2 Experimental and Methodology

4.5.2.1 Experimental Setup

To quantitatively study equilibrium adsorption and to examine the impact of relative humidity, the bench-scale adsorption test setup complying with ASHRAE Standard 145.1 (2008) was used (Figure 4-9). The laboratory compressed air was used as the carrier gas, its flow rate was controlled by a mass flow meter, and it was purified by passing it through a GAC filter to remove potential contaminants. The humidity of the mixed stream was varied from 9.6%±0.6% to 70.2%±2.7% by adjusting the flow rate of the compressed air into the distilled water bottle. In addition, the temperature of the distilled water bottle was maintained constant through a water bath so that it could provide water vapor with a steady concentration. The selected chemicals were in a liquid state at room temperature; they were automatically injected through a syringe pump (KD Scientific). The injected concentrations of selected chemicals were calculated on the basis of airflow rate, chemical injection rate and the chemical properties.

Before connecting to a media column, a PTFE tube (Figure 4-9(1)) was first connected to the test system and was used to transport gaseous pollutant to the calibrated multi-gas analyzer (INNOVA 1312). After the inlet concentration reached a steady state,

the PTFE tube was replaced by a media column filled with TiO_2/FGFs, TiO_2/CCFs, or CCFs (Figure 4-9(2)). The concentration of challenge VOCs after the media column was measured continuously till it was equal to the previous stabilized concentration. For each compound, the adsorption test was performed at T= 22.8±0.5℃ and four different injected concentrations (0.496±0.013 ppm, 0.990±0.010 ppm, 1.971±0.023 ppm, and 4.955±0.063 ppm). Before performing each adsorption experiment, the air filter was conditioned overnight under the corresponding humid conditions to be tested; after each adsorption test, the air filter was conditioned again for regeneration by passing through humidified compressed air.

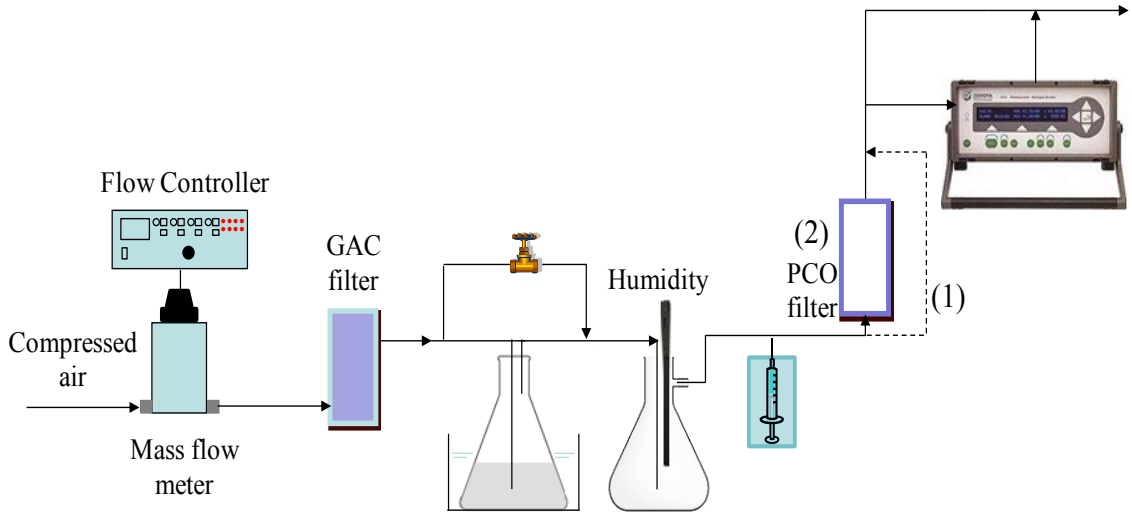

Figure 4-9 Adsorption test setup

4.5.2.2 Adsorption Isotherm Methodology

Many different expressions that describe dynamic equilibrium of sorbed-phase and gaseous phase have been proposed, among which the Langmuir isotherm is the most widely applied in the field of surface kinetics. The Langmuir isotherm model describes

adsorbate-adsorbent systems in which the extent of adsorbate coverage is limited to monolayer coverage of the surface, especially at low loadings. The sorbed-phase concentration of the VOC at the catalyst fiber surface, Cs, can also be estimated by this model.

$$C_S = f(C) = \frac{C_S^0 KC}{1+KC} \qquad [4\text{-}4]$$

where C_S^0 is the maximum sorbed-phase concentration corresponding to monolayer complete coverage, C is the gaseous phase concentration, K is an equilibrium constant, which is the adsorption constant divided by the desorption constant. When the concentration of challenge gases is very low, that is KC<<1, Eq. (4-4) can be simplified to:

$$C_s = f(C) = C_S^0 KC = K_L' C \ , \qquad [4\text{-}5]$$

where K_L' is the synthetic Langmuir parameter that embeds both the saturation capacity, C_S^0 , and the equilibrium constant, K. Eq. (4-5) can be changed into Eq. (4-6) by converting the sorbed-phase concentration, Cs, to the mass of VOCs adsorbed in the surface of catalyst, m_s, and introducing the mass of air filters, m_f, to compensate its impact to the adsorption behavior.

$$\frac{m_s}{m_f} = K_L C \ , \qquad [4\text{-}6]$$

where m_s is the mass of adsorbed VOCs, m_f is the mass of air filters, and K_L is the adsorption coefficient which is defined as the ratio between the mass of adsorbed VOCs in solid phase and the concentration of VOCs in air phase at adsorption equilibrium per unit weight of air filters.

4.5.2.3 Analysis Method

Based on the experimental data obtained from both upstream and downstream air concentration measurements, adsorption capacity of the fiberglass PCO filter for a certain VOC gas can be evaluated. This capacity is expressed as the ratio of the adsorbed mass of contaminant gas over the removal media weight (Haghighat et al. 2008):

$$R_C = \frac{\int_0^{T_{ads}} Q\left(C_{up}^{(t)} - C_{down}^{(t)}\right) dt}{M_{PCO}}, \qquad [4\text{-}7]$$

where R_C is the filter capacity when it reaches equilibrium; T_{ads} is the elapsed time of adsorption test (min); Q is the airflow rate (m^3/min); $C_{up}^{(t)}$ and $C_{down}^{(t)}$ are the upstream and downstream concentration (g/m^3) as a function of elapsed time, respectively; M_{PCO} is the mass of removal media (g): for TiO_2/FGFs, it was 2.715 g; for TiO_2/CCFs with TiO_2, it was 0.890 g; and for original CCFs, it was 0.386 g. It should be noted that in this study $C_{up}^{(t)}$ is computed as the average upstream concentration (before adsorption occurs).

4.5.3 Adsorption Performance for Individual VOC

Figure 4-10 presents the adsorption isotherms for the selected challenge VOCs under different RH conditions. The dimensionless mass ratio (g/g) was used to facilitate the comparison. This figure shows, at four RH levels, all isotherms are linear with respect to the equilibrium concentration. This indicates that the adsorption behaviors of TiO_2/FGFs, TiO_2/CCFs, and CCFs follow ideal monolayer adsorption at low ppm concentrations. The adsorption coefficients were then calculated and it is summarized in Table 4-6. The results clearly indicate that the adsorption performance of the TiO_2 catalyst varies for different compounds and substrates. It also shows that the adsorption coefficient is

significantly affected by the presence of water vapor.

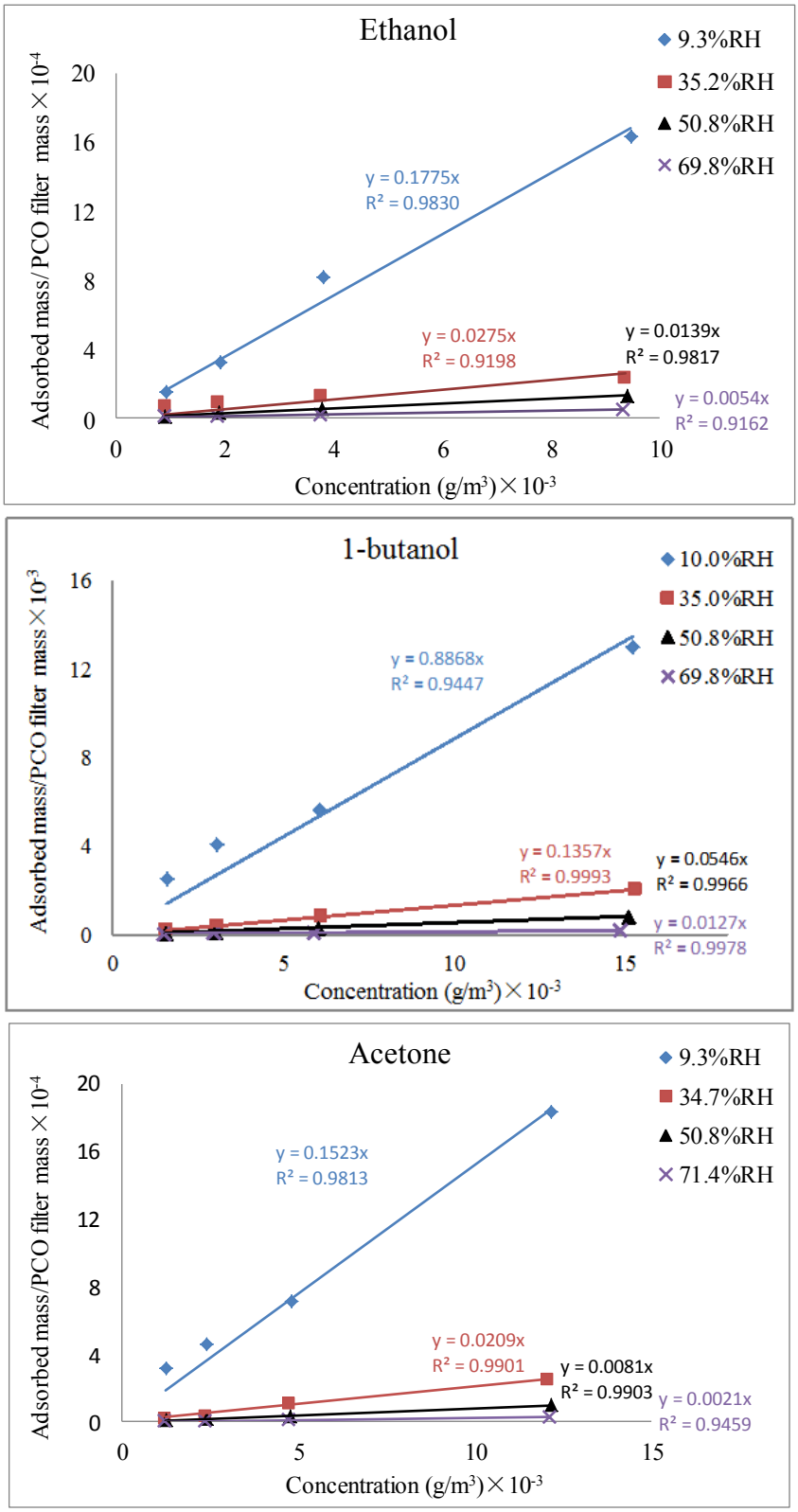

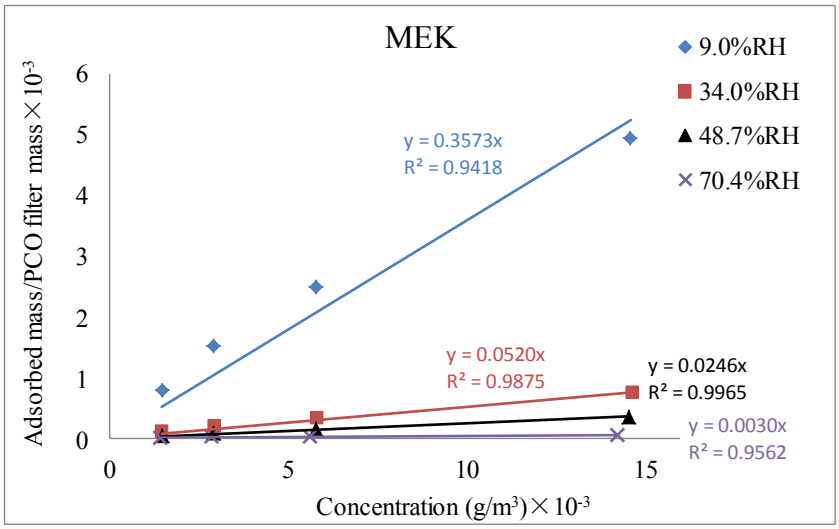
MEK
9.0%RH
34.0%RH
48.7%RH
70.4%RH
y = 0.3573x
R² = 0.9418
y = 0.0520x
R² = 0.9875
y = 0.0246x
R² = 0.9965
y = 0.0030x
R² = 0.9562
Adsorbed mass/PCO filter mass × 10-3
Concentration (g/m3) × 10-3
0
1
2
3
4
5
6
0
5
10
15

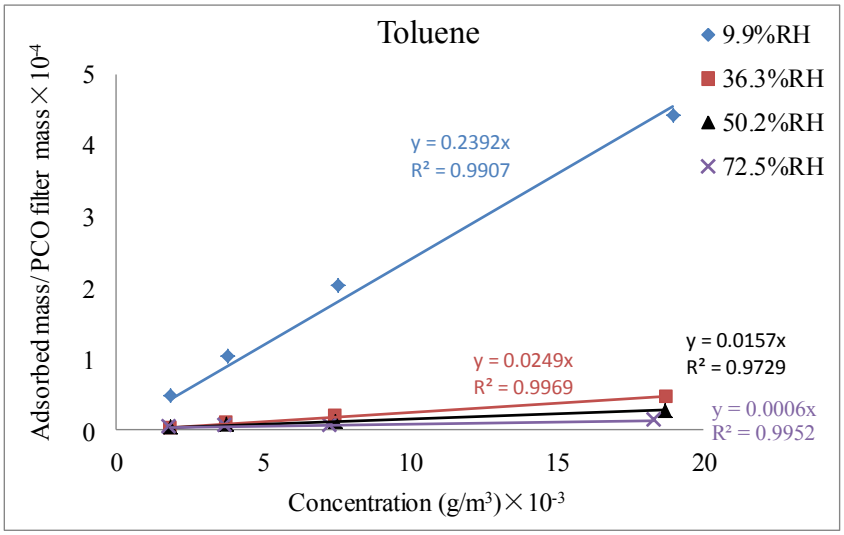
Toluene
9.9%RH
36.3%RH
50.2%RH
72.5%RH
y = 0.2392x
R² = 0.9907
y = 0.0249x
R² = 0.9969
y = 0.0157x
R² = 0.9729
y = 0.0006x
R² = 0.9952
Adsorbed mass/PCO filter mass × 10-4
Concentration (g/m3) × 10-3
0
1
2
3
4
5
0
5
10
15
20

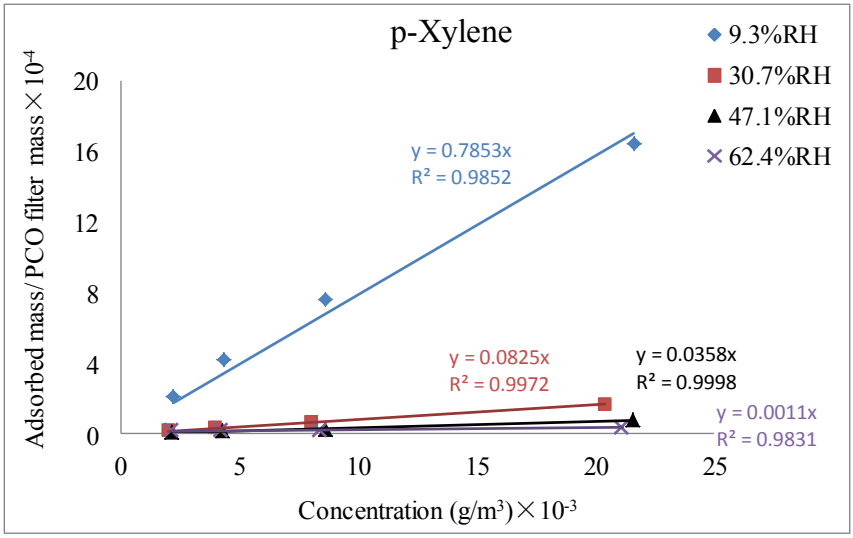
p-Xylene
9.3%RH
30.7%RH
47.1%RH
62.4%RH
y = 0.7853x
R² = 0.9852
y = 0.0825x
R² = 0.9972
y = 0.0358x
R² = 0.9998
y = 0.0011x
R² = 0.9831
Adsorbed mass/PCO filter mass × 10-4
Concentration (g/m3) × 10-3
0
4
8
12
16
20
0
5
10
15
20
25

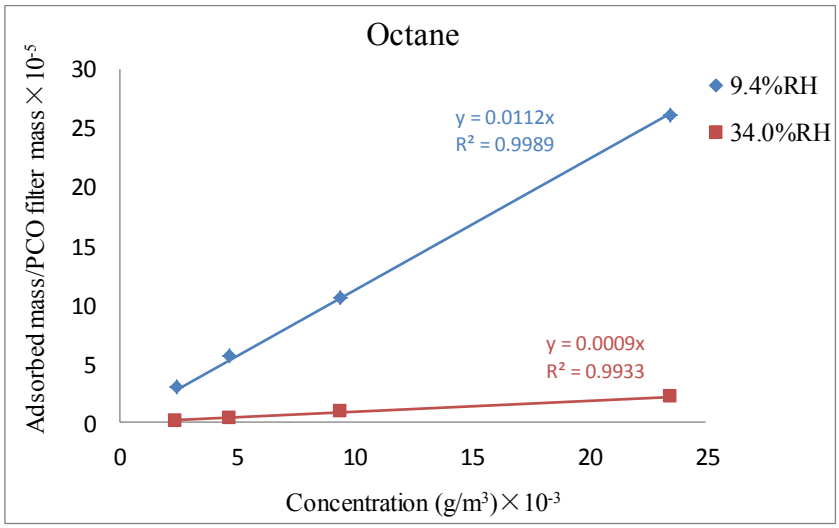
Octane
Adsorbed mass/PCO filter mass × 10-5
30
25
20
15
10
5
0
0
5
10
15
20
25
Concentration (g/m3)× 10-3
9.4%RH
34.0%RH
y = 0.0112x
R² = 0.9989
y = 0.0009x
R² = 0.9933

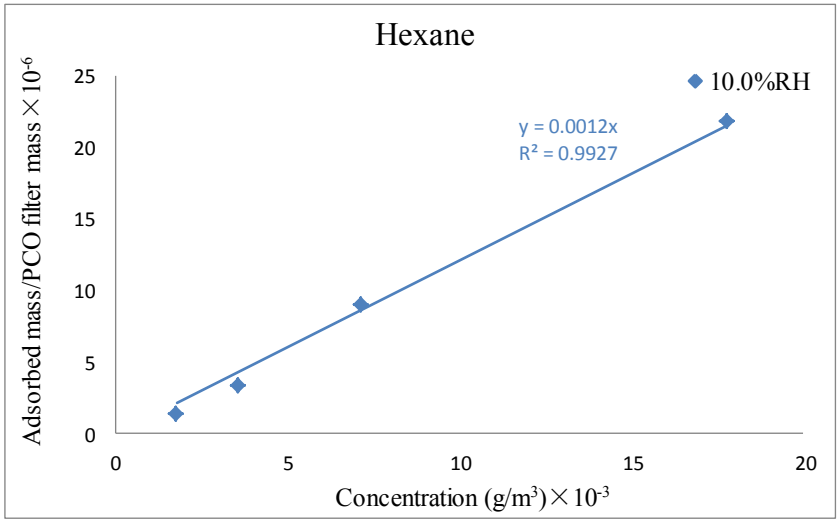
Hexane
Adsorbed mass/PCO filter mass × 10-6
25
20
15
10
5
0
0
5
10
15
20
Concentration (g/m3)× 10-3
10.0%RH
y = 0.0012x
R² = 0.9927

(a) TiO_2/FGFs

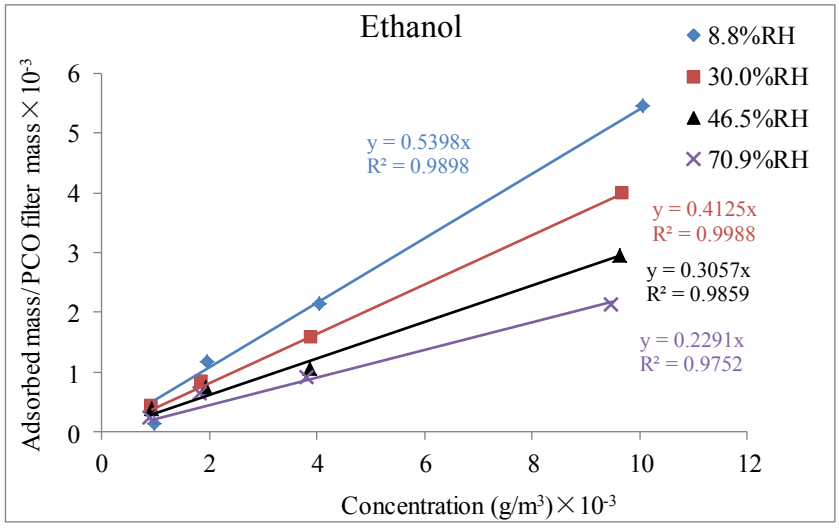
Ethanol
Adsorbed mass/PCO filter mass × 10-3
6
5
4
3
2
1
0
0
2
4
6
8
10
12
Concentration (g/m3)× 10-3
8.8%RH
30.0%RH
46.5%RH
70.9%RH
y = 0.5398x
R² = 0.9898
y = 0.4125x
R² = 0.9988
y = 0.3057x
R² = 0.9859
y = 0.2291x
R² = 0.9752

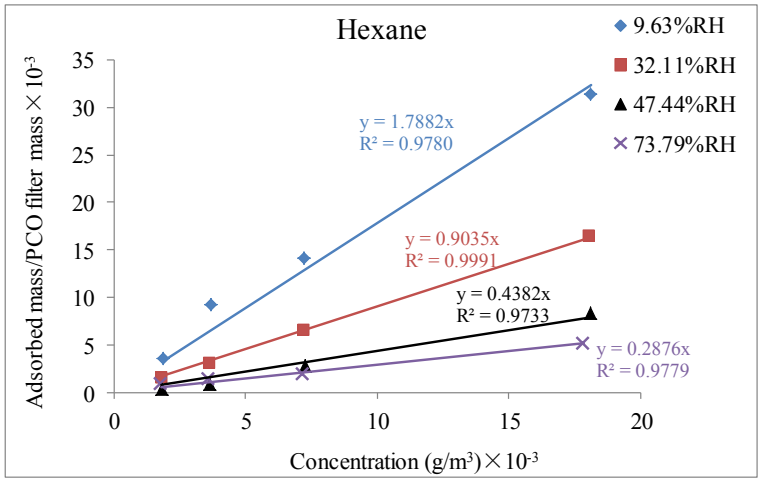

(b) CCFs

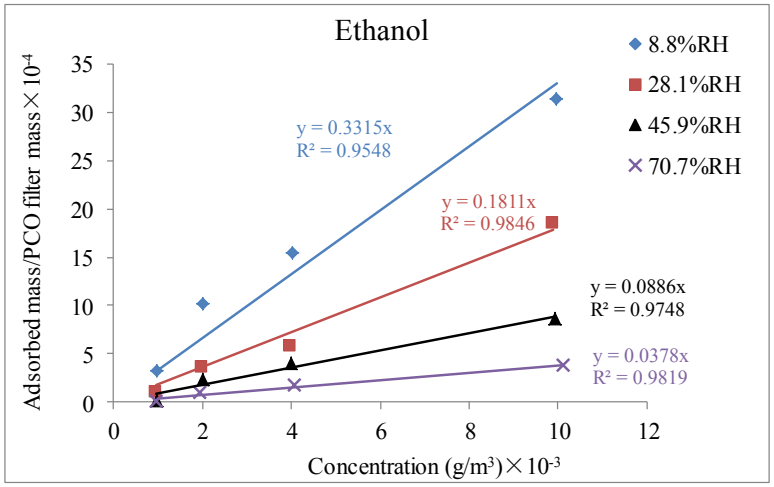

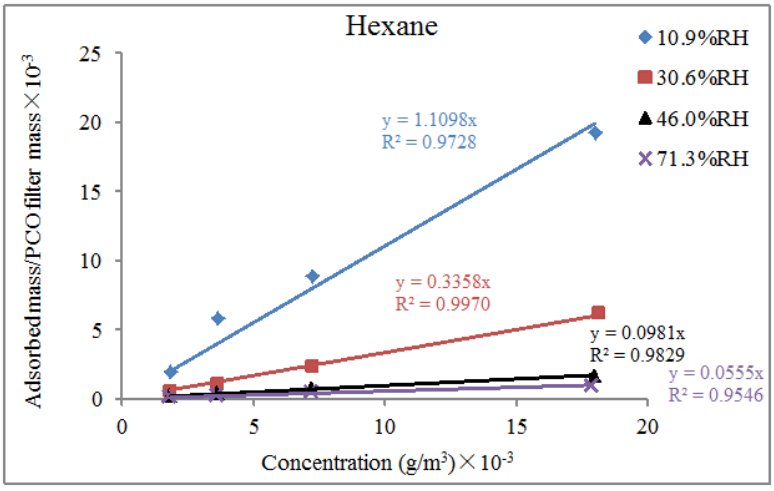

(c) TiO_2/CCFs

Figure 4-10: Adsorption isotherms of the selected challenge gases at various RH conditions (9.6%±0.6% - 70.2%±2.7%) and at 22.8±0.5℃ for (a) TiO_2/FGFs (b) CCFs (c) TiO_2/CCFs

Table 4-6 Summary of adsorption coefficient of individual VOC at various RH

Air Filter	VOC Name	Adsorption Coefficient (m^3/g)[a]			
		RH=9.6% ±0.6%	RH=32.9% ±2.5%	RH=48.3% ±1.8%	RH=70.2% ±2.7%
TiO_2/FGFs	Ethanol	0.1775	0.0275	0.0139	0.0054
	1-butanol	0.8868	0.1357	0.0546	0.0127
	Acetone	0.1523	0.0209	0.0081	0.0021
	MEK	0.3573	0.0520	0.0246	0.0030
	Toluene	0.0239	0.0025	0.0016	0.0006
	P-xylene	0.0785	0.0082	0.0036	0.0011
	Hexane	0.0012	---[b]	---[b]	---[b]
	Octane	0.0112	0.0009	---[b]	---[b]
CCFs	Ethanol	0.5398	0.4125	0.3057	0.2291
	Hexane	1.7882	0.9035	0.4382	0.2876
TiO_2/CCFs	Ethanol	0.3315	0.1811	0.0886	0.0378
	Hexane	1.1098	0.3358	0.0981	0.0555

Note: (a) The data was obtained at 22.8±0.5℃.
(b) For several compounds under a certain level of RH, the adsorption phenomena were not clearly observed and adsorption coefficients were not given.

4.5.4 Discussion

4.5.4.1 Characterization

Figure 4-11 shows the scanning electron microscopy (SEM) images of TiO_2/FGFs and TiO_2/CCFs which show fibers are randomly oriented for both media and TiO_2/CCFs displays fracture surfaces. Nano-TiO_2 particles were coated on the substrates, and the magnified SEM images in Figures 4-11(b) and 4-11(d) demonstrate nano-TiO_2 powders were more uniformly distributed on the FGFs' surface than those loaded on the CCFs due to the CCFs' fiber roughness. Figure 4-12 presents nitrogen adsorption isotherms for CCFs, TiO_2/CCFs and TiO_2/FGFs and their pore size distributions which were obtained from desorption branch of nitrogen isotherm by the BJH (Barrett-Joyner-halenda) method (1951).

The adsorption isotherms (Figure 4-10) indicate the order of adsorption capacity was

CCFs > TiO_2/CCFs > TiO_2/FGFs, which is also further verified by the measured BET surface areas (Table 4-7). The BET surface area of TiO_2/FGFs was much smaller than that of TiO_2/CCFs. It is worth mentioning that BET surface area decreased from 1490.9 m^2/g to 887.7 m^2/g when TiO_2 was loaded on the surface of CCFs. Additionally, the pore size distribution curve manifests that the pore volume of TiO_2/CCFs decreased to some extent in the range of mesopores and formation of macropores resulting from TiO_2 particle agglomeration were observed compared with the original CCFs, see Figure 4-12. This observation indicates the process of TiO_2 coating did not destroy the pore structure, and the presence of the agglomeration of catalyst was at the external surface of fibers. This is consistent with the observation reported by Guo et al. (2008) when they examined similar materials.

Figure 4-12 also shows that pore diameter distributions were narrow for CCFs and TiO_2/FGFs, and pores of three materials (CCF_S, TiO_2/FGFs, TiO_2/CCF_S) were mainly mesopores. It can also be found from Table 4-7 that the pore volume and pore size of TiO_2/CCFs were larger than those of TiO_2/FGFs.

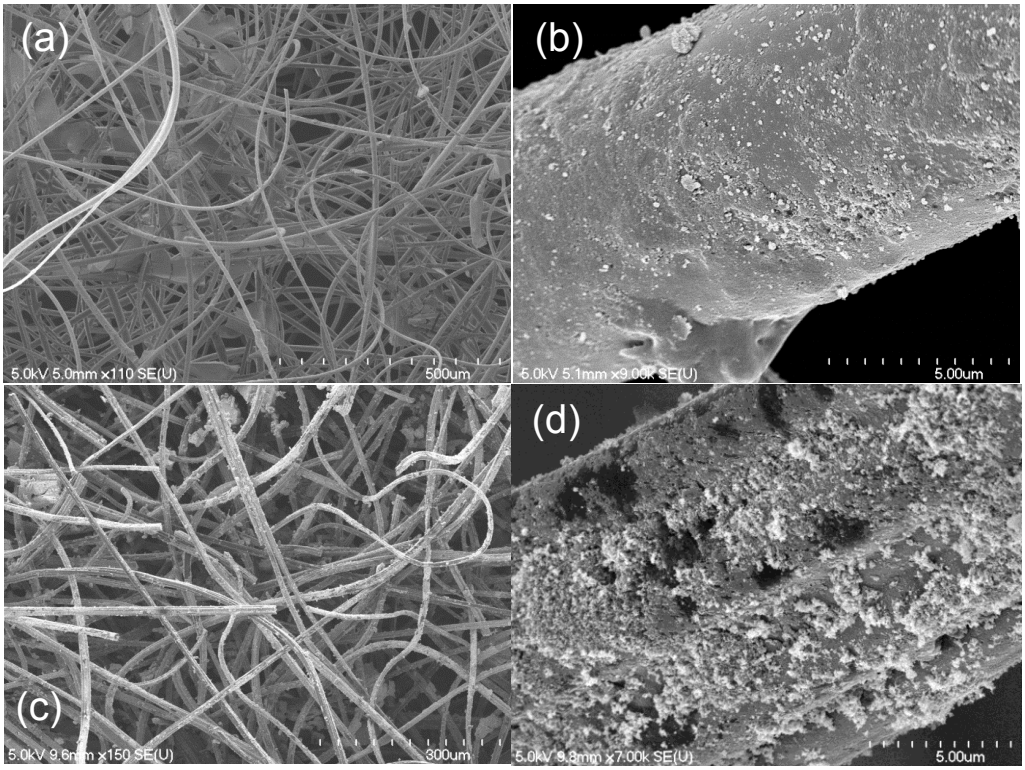

Figure 4-11: (a) SEM images of TiO_2/FGFs and (b) magnified image of TiO_2/FGFs (c) SEM images of TiO_2/CCFs and (d) magnified image of TiO_2/CCFs

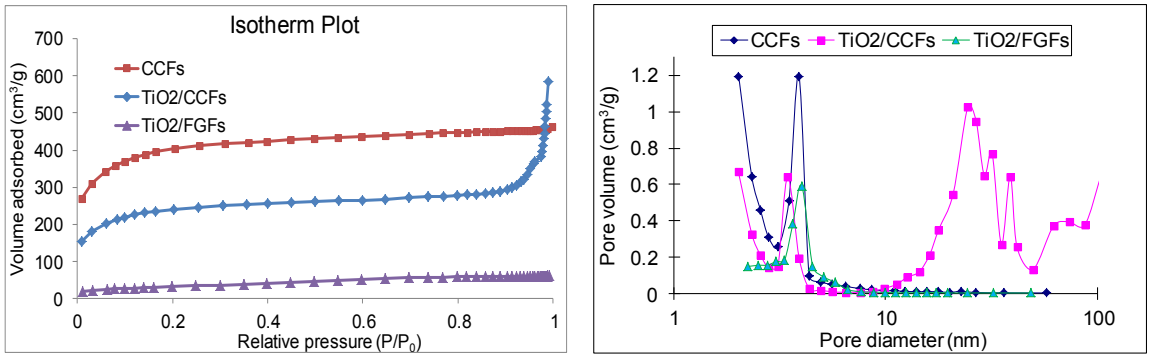

(a) (b)

Figure 4-12 (a) N_2 adsorption isotherms (b) Pore size distributions

Table 4-7 BET surface areas and pore structure parameters for three PCO filters

Parameter	CCFs	TiO_2/CCFs	TiO_2/FGFs
BET surface area (m^2/g)	1490.9	887.7	105.7
BJH desorption pore volume (cm^3/g)	0.26	0.64	0.10
BJH desorption average pore diameter (nm)	2.76	9.59	3.59
TiO_2 loading (wt%)	---	14.32	4.63

4.5.4.2 Adsorption Coefficients Verification

Demeestere et al. (2003) presented the linear adsorption curves for trichloroethylene, toluene, and chlorobezene on the photocatalyst TiO_2 at 25.0℃. They found that the adsorption coefficient of toluene was 0.00253 m^3/g and 0.000103 m^3/g for RH=0% and 57.8%, respectively. Coronado et al. (2003) reported the adsorption constant of acetone for the weak sites of TiO_2 thin film was 0.2 m^3/g and 0.046 m^3/g for RH=0% and 25%, respectively. Tomida et al. (2005) investigated the adsorption isotherms of acetone on the photocatalyst of TiO_2 coated on silica beads and obtained similar results. All the reported adsorption coefficient values are at the same order of magnitude as those obtained in this study.

4.5.4.3 Adsorption coefficient and properties of VOC

Results of TiO_2/ FGFs indicate that for the polar VOCs, such as ethanol, isobutanol, acetone, and MEK, the adsorption coefficients are roughly one order of magnitude higher than those of non-polar VOCs for a given RH level. Also, the results further indicate the TiO_2/ FGFs filter, a polar substance, has a higher adsorption preference for polar VOCs. The order of adsorption capacity for the selected chemical classes follows the sequence of alcohols > ketones > aromatics > alkanes. This feature is attributed to the strength of the corresponding intermolecular forces between adsorbed VOCs and the catalyst surface. Dispersion forces are the main intermolecular forces holding non-polar alkanes in the solid phase, which are weaker than van der Waals interactions for aromatic hydrocarbons. Due to the high dipole moment of the carbonyl group, dipole-dipole interactions for ketones are stronger than van der Waals attractions for aromatic hydrocarbons. In

addition to van der Waals interactions, hydrogen bonding plays a greater role for the attraction between alcohols and hydrated catalyst surface. This order agrees with the photocatalytic oxidation rates reported by Hodgson et al. (2007) and Obee and Hay (1999). Thus, it is inferred that the PCO reaction rate is closely related to the adsorption process.

Another trend has been observed from the results of TiO_2/ FGFs. That is, for the compounds in the same chemical class, the adsorption coefficient increases with the increase of molecular weight and boiling point. This agrees with the adsorption characteristics for sorption-based media. For the structurally similar compounds, the higher the boiling point is the greater the intermolecular forces. Hence, the van der Waals forces of the heavier compounds make them more likely to be adsorbed to the TiO_2 catalyst.

Adsorption results of CCFs and TiO_2/CCFs demonstrate that CCFs belongs to a non-polar material due to the higher adsorption capacity of hexane compared with that of ethanol, see Table 4-7. Moreover, adsorption capacity of original CCFs is higher than that of TiO_2/CCFs for both hexane and ethanol since the BET surface area of CCFs is larger than that of TiO_2/CCFs, which results in the fact that adsorption sites on CCFs are obviously more than that those on TiO_2/CCFs.

4.5.4.4 Effect of relative humidity

The effect of RH on the adsorptive performance of three substrates was investigated in the range of 9% (2300 ppm)-70% (19600 ppm). From Figure 4-13, it can be noticed that the adsorption coefficient of each tested compound decreases as RH rises from 9% to 70% for three substrates. Obviously, the presence of water vapor plays an important role

on the adsorption behavior of VOCs on the catalyst.

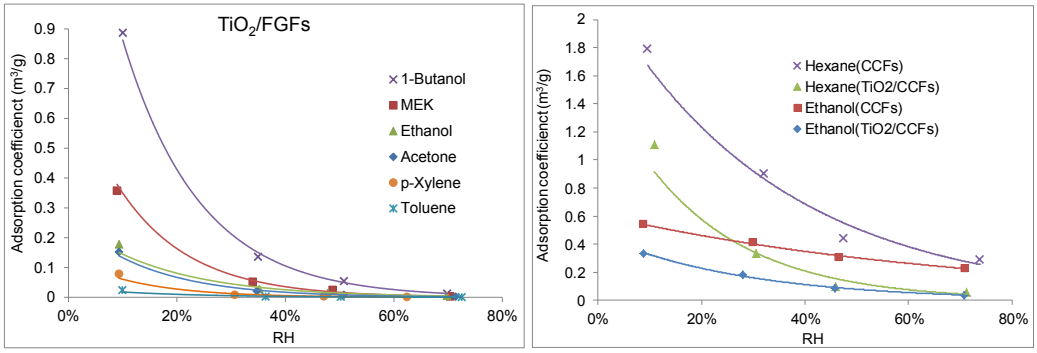

(a) TiO_2/FGFs (b) TiO_2/ CCFs and CCFs

Figure 4-13 Relation between adsorption coefficient and RH for different VOCs: (a) TiO_2/FGFs, and (b) TiO_2/ CCFs and CCFs

Figure 4-14 shows the variation of K_L as a function of RH. This figure indicates that K_L varies exponentially: an increasing amount of physically adsorbed water vapor significantly results to reducing the adsorbed organic molecules at the surface of catalyst. This phenomenon can be attributed to the competition of water molecules and VOCs molecules at the catalyst surface sites. Hydrogen bonding for water is stronger than van der Waals interactions for most tested VOCs so that water is more easily adsorbed on the surface of photocatalysts. According to Maudhuit et al. (2011), the formation of one or several layers of water clusters at the surface of TiO_2 in humid air conditions decreases accessibility of the pollutants to active sites. In addition, decreasing trends of adsorption capacity with RH also indicates the tested three PCO air filters in this study are hydrophilic. Figure 4-14 shows there is a linear relationship between $\ln(K_L)$ and RH.

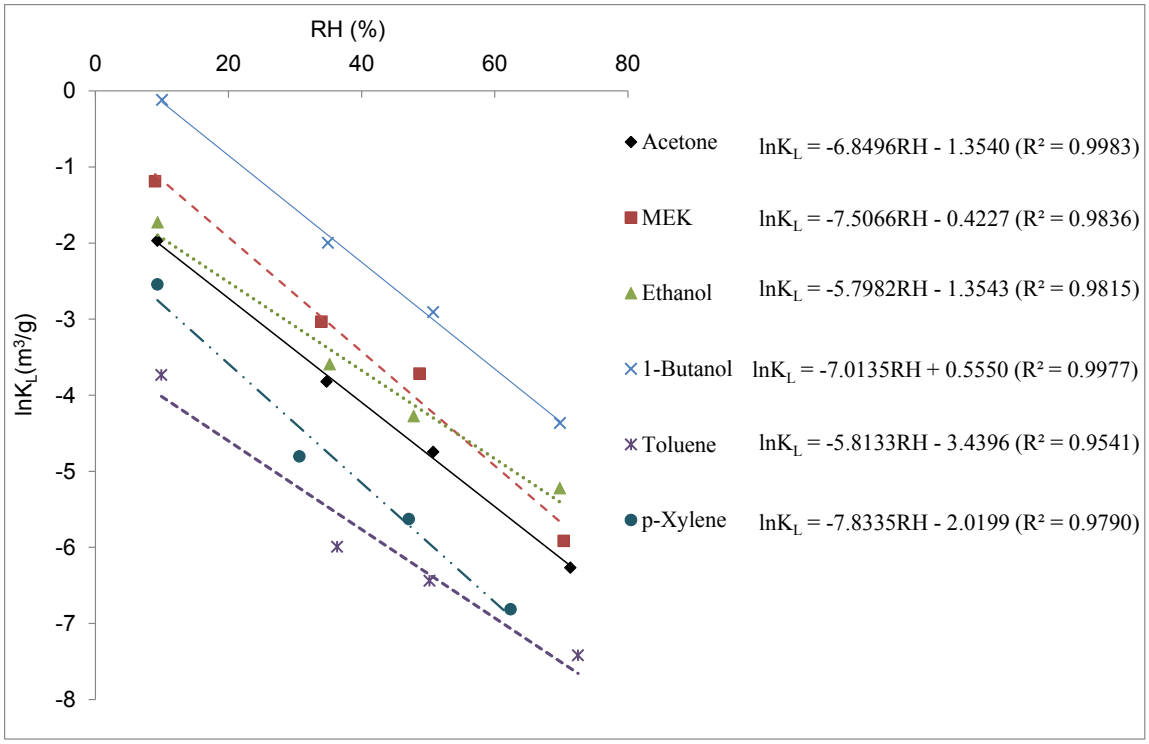

(a) TiO_2/FGFs

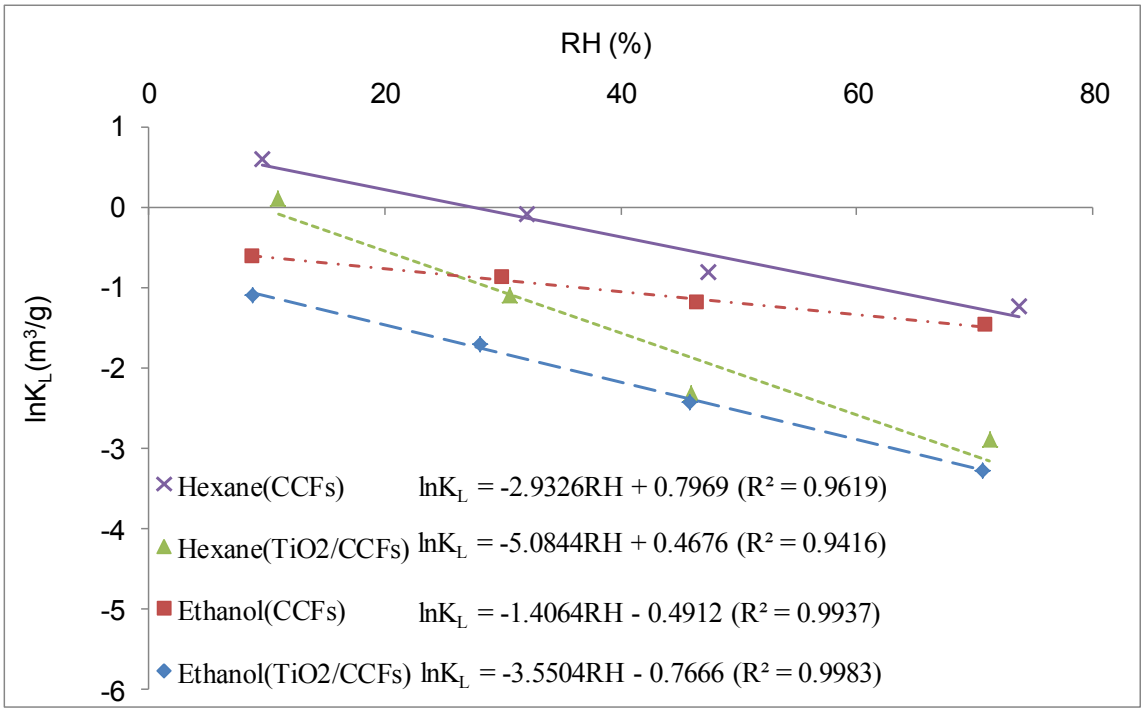

(b) TiO_2/ CCFs and CCFs

Figure 4-14 Adsorption profiles of various compounds with relative humidity range from 9.6% to 70.2% for (a) TiO_2/FGFs, and (b) TiO_2/ CCFs and CCFs

4.5.4.5 Adsorption performance of TiO_2/FGFs and TiO_2/CCFs

Table 4-7 shows that the BET surface area of TiO_2/ CCFs is higher than that of TiO_2/FGFs results in TiO_2/ CCFs having a greater adsorption capacity. This is ascribed to the fact that a large number of adsorption sites on the TiO_2/ CCFs surface are beneficial to rapid molecular diffusion of VOCs, thereby increasing the adsorption capacity. Moreover, CCFs as a supporting substrate have high adsorption ability. When the challenge VOCs come in contact with the surface of the PCO filter, part of the molecules are directly adsorbed by the TiO_2, while the rest may be physically captured by CCFs. Test results of hexane shown in Figure 4-10(b) are an excellent interpretation of the significant impact of the substrate on the adsorption performance. For TiO_2/FGFs, the adsorption capacity of hexane was very low. Even when RH was greater than 9.6%±0.6%, the adsorption phenomena were not clearly observed (Figure 4-10 (a)). While for TiO_2/ CCFs, the adsorption of hexane was obviously observed at various RH values (Figure 4-10 (c)). The adsorption capacity was found as 1.1098 m^3/g (9.6%±0.6%), 0.3358 m^3/g (32.9%±2.5%), 0.0981 m^3/g (48.3%±1.8%) and 0.0555 m^3/g (70.2%±2.7%), which was greater than the adsorption capacity of ethanol under the same RH conditions, respectively (Table 4-6). This is consistent with results reported in previous studies (Kholafaei et al., 2010) that removal performance of the granular activated carbon filters is positively correlated to the VOCs molecular weight.

Figure 4-14 shows that the presence of water vapor has less influence on the adsorption behavior of TiO_2/CCFs than that of TiO_2/FGFs. The strength of hydrophilicity of a substrate determines the extent of interactions of adsorbed water film on the TiO_2 surface. Hence, FGFs is more hydrophilic compared with CCFs so that affinity of water

for FGFs is stronger than that of CCFs. This can be interpreted with the fact that adsorption energy of water vapor for fiberglass is 0.57 J/mol (Huang et al., 1973), which is much smaller than that of 27.2 kJ/mol for activated carbon (Delage et al., 1999). Cao et al. (2000) reported that TiO_2 by itself is a kind of strongly hydrophilic substance. Therefore, the RH parameter, to some extent, influences the adsorption property of air filters with surfaces coated with TiO_2.

4.6 UV-PCO Test Results and Discussion

4.6.1 Repeatability

Figure 4-15 shows the results of the repeatability test for the TiO_2/FGFs filter and the TiO_2/CCFs filter illuminated with UVC or VUV lamps when it was challenged by 500 ppb ethanol: it shows the good agreement between the two experiments. It is worth to mention that the regeneration duration between two tests was 20 minutes, which indicates the deactivation phenomenon was negligible when the UV-PCO system was challenged by a low concentration of VOCs for a short period (around 2 hours).

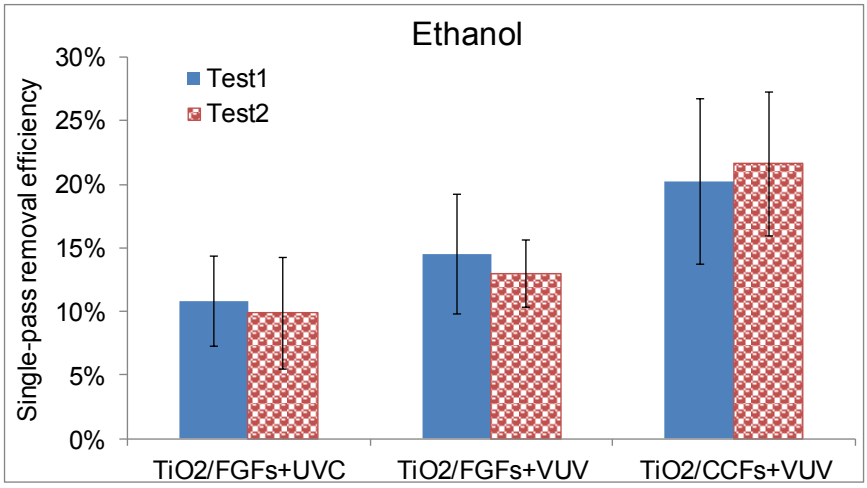

Figure 4-15 Repeatability test for three testing scenarios

4.6.2 Effect of VOC Type

The removal of different compounds was investigated separately in the four-duct system using the same configurations and arrangements. Figure 4-16 presents the conversion of each VOC at an inlet concentration of 500 ppb under three experimental scenarios (TiO_2/FGFs+UVC, TiO_2/FGFs+VUV, and TiO_2/CCFs+VUV). For two types of air filters, the order of single-pass removal efficiency of the selected chemical classes follows the sequence of alcohols > ketones > aromatics > alkanes. These observations agree with the photocatalytic oxidation rates reported by Hodgson et al. (2007) and Obee and Hay (1999). This implies that adsorption process, to be more specific, the intermolecular force is one of the key factors influencing the photocatalytic activity. For non-polar alkanes adsorbed in the solid phase, dispersion forces are the main intermolecular force, which is weaker than van der Waals interactions for aromatics. Due to the high dipole moment of the carbonyl group, dipole-dipole interactions for ketones are stronger than van der Waals attractions for aromatics. In addition to van der Waals interactions, hydrogen bonding plays a greater role for the attraction between alcohols and hydrated catalyst surface. TiO_2/FGFs filter presents hydrophilic property, and VOCs with high polarity show higher affinity to the surface of TiO_2/FGFs filter, whereas TiO_2/CCFs filter belongs to a non-polar substrate which prefers to adsorb non-polar VOCs. It is worth mentioning that RH was unregulated (15-45%) for all tests, and the cross influence of RH on the UV-PCO performance for different VOCs was not considered here.

In addition, the lighter VOC in the same chemical class always shows higher photocatalytic activity than the heavier VOC for the TiO_2/FGFs filter, which is opposite

for the TiO_2/CCFs filter. This is attributed to the fact that for the TiO_2/FGFs filter with less adsorptive ability, intermediates of small molecular weight generated from UV-PCO of light compounds are less competitive with light compounds for adsorption and photocatalytic reaction at active sites, and they are also more easily further oxidized or desorbed under humid conditions resulting in more active sites available. For example, tolualdehyde (4-Methylbenzaldehyde) generated from UV-PCO of xylene keeps a strong bond to the surface, thus blocking reaction sites. After a long-term application, this may lead to a complete deactivation of the catalyst. However, for the TiO_2/CCFs filter with strong adsorption ability, van der Waals interaction is the dominant force, which increases with molecular weight. Hence, the heavier compound of each group demonstrates more activity in UV-PCO.

It can be also observed from Figure 4-16 that single-pass UV-PCO removal efficiency of TiO_2/CCFs filter is distinctly higher than that of TiO_2/FGFs filter for all compounds. Photocatalytic activity depends not only on the properties of challenge compounds but also on the features of substrates supporting TiO_2. Generally, the larger specific surface area helps to increase photocatalytic activity since more active sites are provided through coating of TiO_2 nano-particles on the larger BET surface of TiO_2/CCFs (Zhong et al., 2012). According to Table 4-7, the BET surface area of TiO_2/CCFs was 887.7 m^2/g, which was roughly 8 times higher than that of TiO_2/FGFs leading to a higher photocatalytic activity for TiO_2/CCFs.

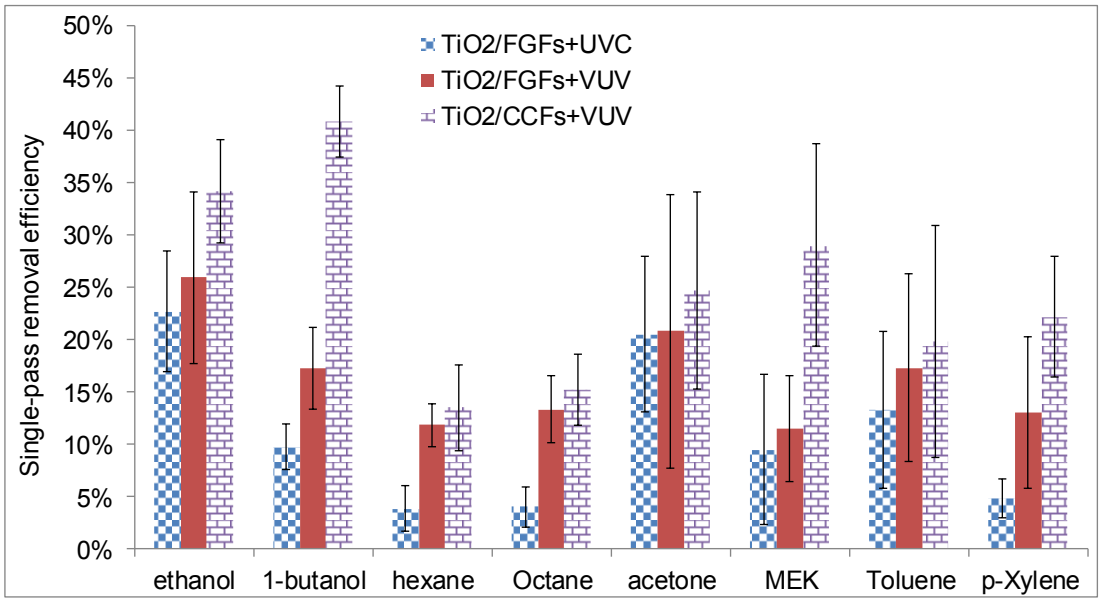

Figure 4-16 Single-pass removal efficiencies of various compounds under three different experimental scenarios (C_{in}=500 ppb, RH= 15%-45%, airflow rate= 170 m^3/h, irradiance= 27-36 W/m^2)

4.6.3 Effect of Inlet Concentration

The UV-PCO experiments were conducted using three different inlet concentration levels with all selected compounds to examine its effect on the removal performance of UV-PCO. Usually the inlet concentration was 250 ppb, 500 ppb and 1000 ppb, except that maximum 800 ppb was selected for 1-butanol due to difficult evaporation and minimum 500 ppb was used for acetone because of detection limit. The effect of the inlet concentration on the single-pass removal efficiency for various compounds is shown in Figure 4-17. The trend of a lower inlet concentration resulting in higher removal efficiency was observed for all compounds. The same behavior was also observed by Jeong et al. (2005) when they studied the photodegradation of toluene in the range of inlet concentrations from 0.6 to 20 ppm under VUV irradiation. This can be interpreted by the limited adsorption capacity of the fixed active sites at the catalyst surface. The

amount of molecules effectively participating in the UV-PCO reaction is not enhanced in the same ratio as an increase of the inlet concentration resulting in a decrease of removal efficiency. Moreover, the competitive effect between multiple by-products and the challenge VOC to some extent inhibits the adsorption of a VOC especially when its inlet concentration is high. Hence, compared with the challenge concentrations, the number of the active sites resulting from low BET surface area of TiO_2/FGFs is a limiting factor in this study. This result agrees with the conclusion made by Sleiman et al. (2009) that PCO is suitable for the photodegradation of gaseous effluents at low ppb concentration levels. It should be noted that although RH was not constant between tested compounds, it was almost constant for each individual one for three concentration levels.

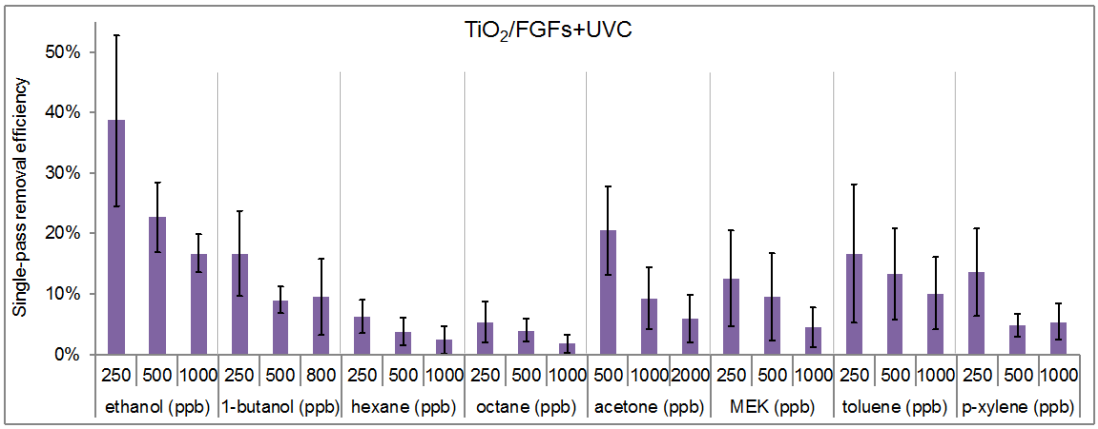

Figure 4-17 The effect of inlet concentration on conversion of various compounds under UVC irradiation for the TiO_2/FGFs air filter (RH= 15%-45%, airflow rate= 170m^3/h, irradiance= 27-30 W/m^2)

4.6.4 Effect of Airflow Rate

Figure 4-18 shows the effects of airflow rate on the conversion of ethanol. The airflow rate varied from 69 m^3/h (45 cfm) to 255 m^3/h (150 cfm) for the TiO_2/FGFs filter and from 41 m^3/h (25 cfm) to 170 m^3/h (100 cfm) for the TiO_2/CCFs filter. It is evident

from the results that the conversion decreased gradually with an increase in the airflow rate. The same behavior was also observed for acetone, hexane and toluene when the airflow rates were increased. Also, these trends are in accordance with results reported previously (Jeong et al., 2005; Hodgson et al., 2007; Yu and Brouwers, 2009). In addition, the curve of ethanol result is somewhat consistent with the finding reported by Hodgson et al. (2007) that the relationship between the reaction efficiency and the residence time is approximated reasonably well by an exponential function.

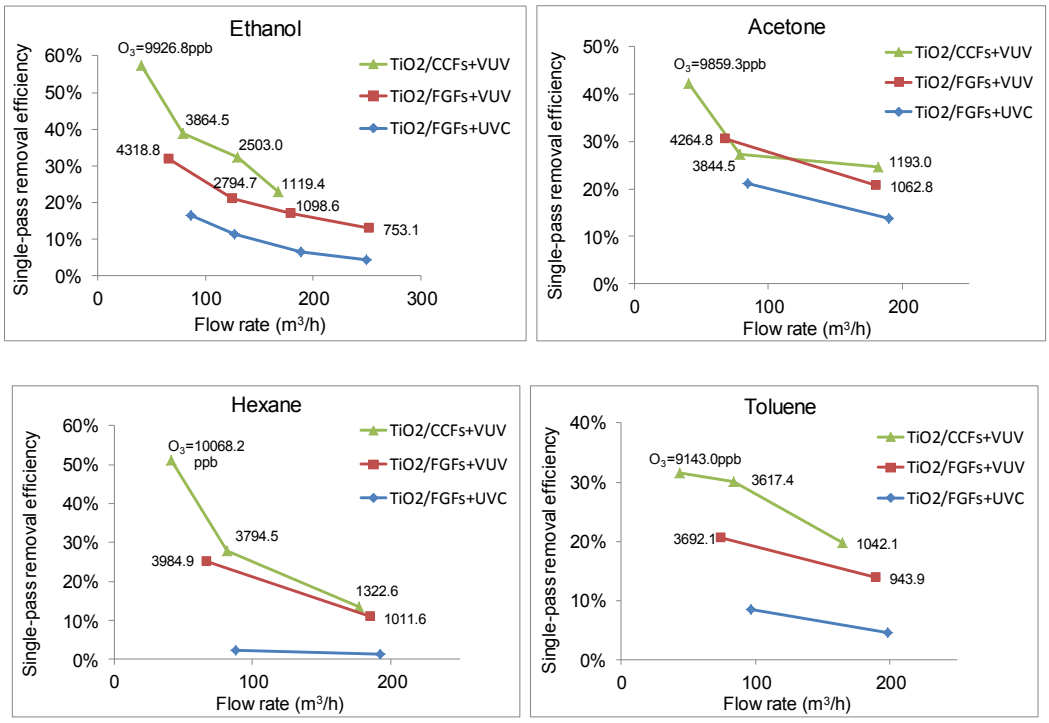

Figure 4-18 The effect of flow rate on ethanol, acetone, hexane, and toluene conversion (C_{in}=500 ppb, RH=40%-60%, irradiance= 24-39 W/m^2)

The airflow rate of 41-255 m^3/h corresponding to a face velocity of 0.12-0.76 m/s (shown in Table 4-8) was used in this study. However, by changing the airflow rate, the residence time differed a lot. Here, residence time is defined as the thickness (0.95 cm) of the air filter divided by the face velocity. Table 4-8 presents the residence time and the

pressure drop for the tested airflow rates of two air filters. Decreasing the airflow rate helps to increase the residence time so that more compounds can be adsorbed to the catalyst surface and adsorbed molecules have more chances to participate in the reactions with hydroxyl radicals, and then to be oxidized. As a consequence, a higher conversion rate can be achieved. It was observed that the pressure drop increased as the airflow rate enhanced for two filters. To be more specific, the pressure drop of the TiO_2/CCFs filter increased more compared to that of the TiO_2/FGFs filter due to the high resistance resulting from the high BET surface area of the TiO_2/CCFs filter. It should be noted that in the case of VUV irradiation, ozone concentrations were varied when airflow rate changed. Ozone also plays a certain role for the removal of VOCs, which was discussed in Section 4.4. Therefore, a lower airflow rate results in higher single-pass removal efficiency. The multi-pass method may be an alternative to relatively extend the residence time of the VOCs for PCO technology applied in HVAC systems.

Table 4-8 PCO conditions at different airflow rates

PCO filter	Airflow rate (m^3/h)	Pressure drop at PCO (Pa)	Face velocity (m/s)	Residence time (ms)
TiO_2/FGFs	69	8	0.21	45
	89	13	0.26	37
	127	26	0.38	25
	187	47	0.56	17
	255	78	0.76	12
TiO_2/CCFs	41	17	0.12	79
	81	45	0.24	40
	127	99	0.38	25
	170	188	0.51	19

4.6.5 Effect of Light Intensity

The effect of light intensity on the performance of the UV-PCO air cleaners was examined at 170 m^3/h airflow rate with the lighter compounds of each selected group (ethanol, hexane, acetone, and toluene). In this study, the configurations of one, two, three, and four UVC lamps standing in a row with two TiO_2/FGFs filters were used in each duct, and the vertical distance between air cleaners and UV lamps was kept constant. The range of irradiance employed was 16-43 W/m^2. The experimental results of single-pass removal efficiency for tested VOCs are shown in Figure 4-19. The increase trend of conversion rate with an increase of the irradiance was observed for all VOCs. The trend was correctly described by a power function, and the power exponent was in the range of 0.4-0.6, which is consistent with the reaction order of 0.5 for high absorbed light intensity (greater than 10-20 W/m^2) reported by Obee and Brown (1995). It is should be noted that the removal efficiency of ethanol was lower than that of acetone due to the possible reason of partial deactivation of the catalyst in this case.

The PCO reactions are driven by photon absorption, which results in the formation of hydroxyl radicals in the presence of water vapor. Usually, the reaction rate constant increases with the light intensity since more hydroxyl radicals are generated. However, the recombination of the electron-hole pairs at the high light intensity, to some extent, inhibits the rate of electron transfer, and thus the gain in the UV-PCO performance is not linear with the number of UV lamps employed. Additionally, not all of the photons from additional UV lamps reach the air filters. Adding more UV lamps demonstrated the positive effect of UV power on the PCO performance, which led to the conclusion that the hydroxyl radical concentration was the rate-limiting process in this system. Increasing

the number of lamps enhance the UV energy to the catalyst so that the efficiency of the PCO system was increased.

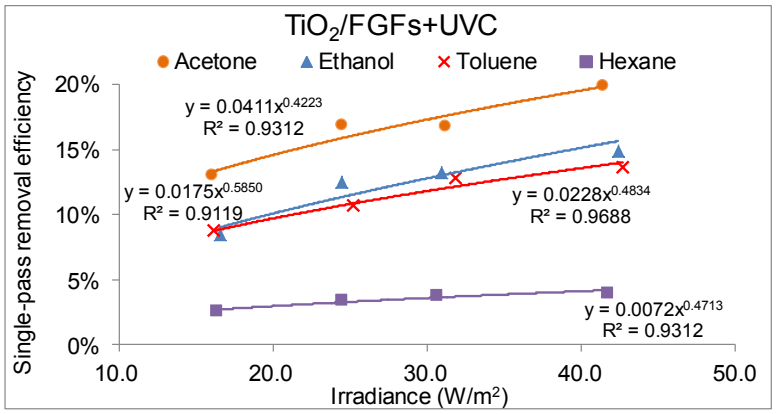

Figure 4-19 The effect of irradiance on ethanol, acetone, hexane, and toluene conversion (C_{in}=500 ppb, flow rate= 170 m^3/h, RH=55%-62%)

4.6.6 Effect of Relative Humidity

Water vapor plays a dual role in UV-PCO through the following ways: on the one hand it provides hydroxyl radicals by chemical decomposition of adsorbed water; on the other hand excessive water vapor competes with challenge compounds for the same surface of TiO_2. Numerous studies have been conducted on its effect on the performance of UV-PCO, and different results were reported in the literature. Actually, the optimal humidity level is determined by the balance between conversion promotion through chemical processes and inhibition through physical interactions (Zhong et al., 2010).

Due to the limitation of the test facility, RH inside the duct was uncontrolled. RH examining experiments were conducted when the laboratory RH conditions achieved to the expected levels. In this study, the effect of water vapor on the conversion of compounds was examined by applying humidity levels from 10% (2300 ppm) to 60% (16000 ppm) to 500 ppb ethanol and selected humidity levels to 500 ppb acetone, hexane,

and toluene. Figure 4-20 shows the single-pass removal efficiency for all chemical compounds as a function of RH at different experimental scenarios. A decrease in the conversion rate of ethanol from 26% to 11% was observed when RH increased from 10% to 57% for the TiO_2/FGFs filter under UVC illumination. In the case of VUV exposure, the conversion of ethanol for TiO_2/CCFs and TiO_2/FGFs decreased from 40% to 23% and from 30% to 13%, respectively. For the other chemical compounds, water vapor also shows inhibition effect on their conversion rates. These observations can be interpreted as the competition for adsorption between the VOC and water molecules. In addition, the presence of abundant water may enhance the possibility of electron-hole recombination, which is an unfavorable process for the treatment of indoor air pollutants by PCO technology. Moreover, Sleiman et al. (2009) reported that reaction mechanisms can be modified under different RH levels, and some strongly bound surface species formed at high RH level stick to the TiO_2 surface resulting in a decrease of mineralization. According to ASHRAE Standard 55-2010, a relative humidity between 40% and 60% is recommended for a healthy and comfortable indoor environment. Compared with VOCs concentrations (typically ppb level) in the context of indoor air applications, water vapor exists in large excess so that it is unlikely that the hydroxyl radical concentrations become a rate-limiting factor. Competitive adsorption and electron-hole recombination can be deemed as the dominating interaction processes under the condition that the relative humidity is achievable in buildings and HVAC systems.

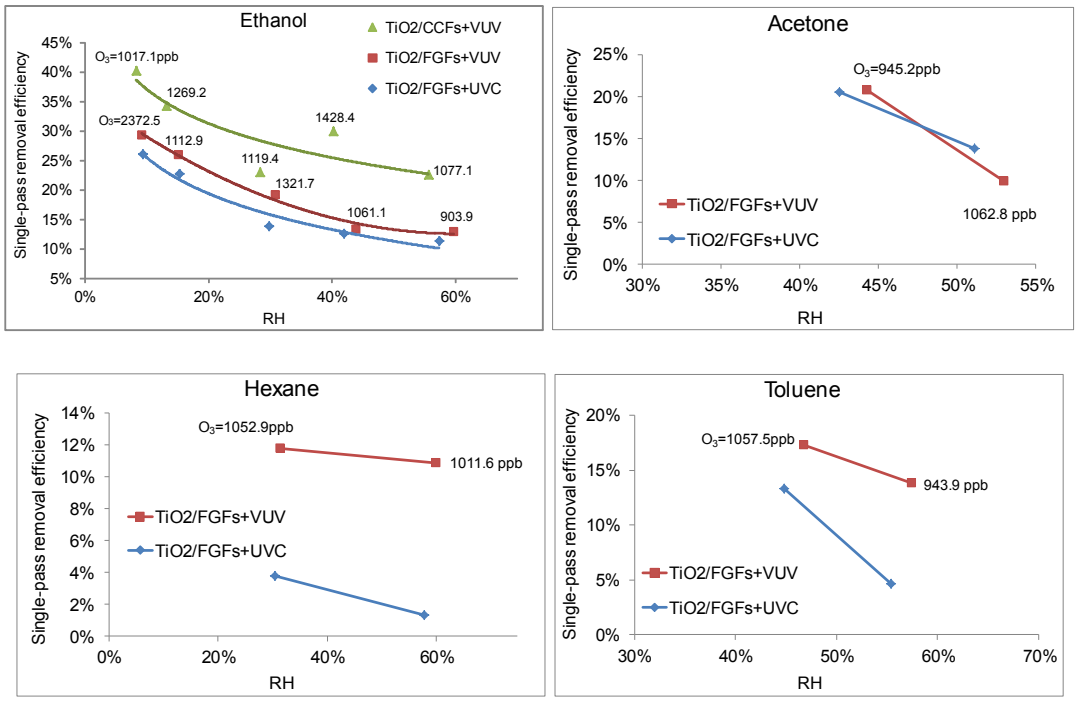

Figure 4-20 The effect of RH on ethanol, acetone, hexane, and toluene conversion at different experimental scenarios (C_{in}=500 ppb, flow rate=170 m^3/h, irradiance=24-36 W/m^2)

4.6.7 Ozone-involved UV-PCO

The electron affinity (EA) of O_3 is 2.103 eV, and is considerably larger than that of O_2 (0.44 eV) or the oxygen atom (1.46 eV) (Matejcik et al., 1996). Thus, excited electron resulting from absorbance of UV photon with TiO_2 is captured more efficiently in the presence of O_3. The possible set of reaction steps considered in this scenario is described as follows:

$$e_{CB}^- + O_3 \rightarrow O^- + O_2 \quad [4\text{-}12]$$

$$e_{CB}^- + O_2 \rightarrow O_2^- \quad [4\text{-}13]$$

$$O_2^- + O_3 \rightarrow O_2 + O_3^- \quad [4\text{-}14]$$

$$O_3^- + H_2O \rightarrow OH\cdot + OH^- + O_2 \quad [4\text{-}15]$$

The enhancement of electron capture rate due to the participation of ozone in the PCO process not only reduces the possibility of recombination of electron-hole pairs, but also more effectively produces hydroxyl radicals through complicated chain reactions. Consequently, the single-pass removal efficiency of TiO_2/ VUV was usually higher than that of TiO_2/UVC for the tested VOCs (see Figure 4-16) due to the higher generation rate of hydroxyl radicals in the presence of ozone. Jeong et al. (2005) also came to the same conclusion that employment of VUV in PCO technology may be effective for the treatment of gas streams containing high concentrations of VOCs.

4.7 By-products

4.7.1 By-products from Background Tests

The by-products background test in the duct system was implemented using the same procedure described in Section 4.2.4 except that there was no injection of chemicals and absence of a PCO filter. After the laboratory air was introduced into the test system under UV illumination, an odor was found inside the ducts. GC/MS results showed that C_5-C_{12} aldehydes were detected in the gas phase of the downstream (see Figure 4-21). Duct systems were sealed with neoprene gaskets or sealing caulk, which may emit aldehydes under exposure to ozone and/or radiation. Similar observation was made by Morrison et al. (1998).

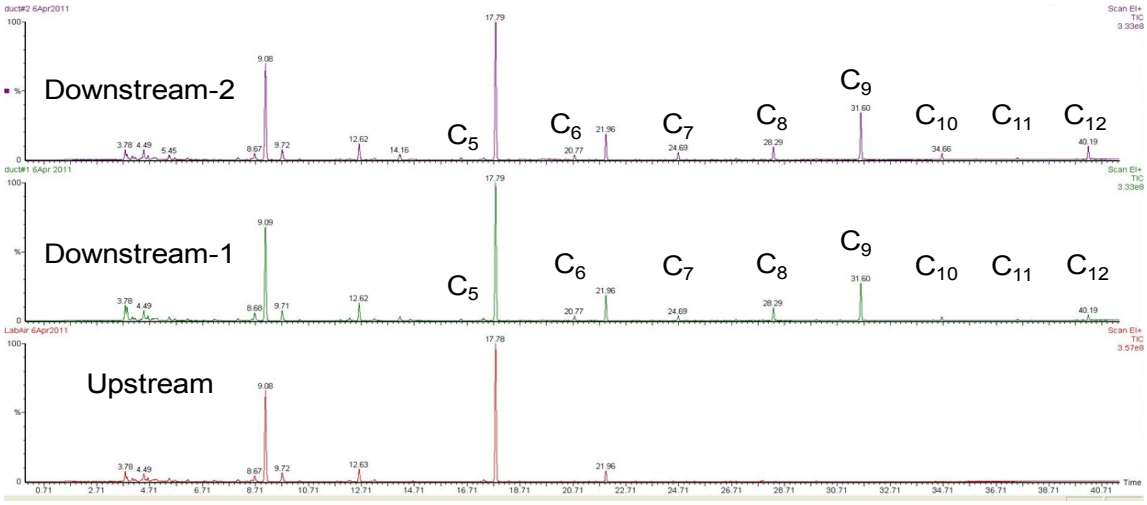

Figure 4-21 Total ion chromatogram of VOCs in the collecting gas of upstream and downstream by GC/MS. Abbreviations: C_5, pentanal; C_6, hexanal; C_7, heptanal; C_8, octanal; C_9, nonanal; C_{10}, decanal; C_{11}, undecanal; C_{12}, dodecanal.

4.7.2 By-products from UV-PCO Tests

The formation of by-products in the photocatalytic oxidation of all selected compounds was investigated. Table 4-9 lists all the gas-phase UV-PCO by-products detected using the HPLC. Formaldehyde and acetaldehyde were produced as the UV-PCO reaction products for all experiments in the absence or in the presence of ozone. Usually, yields of formaldehyde and acetaldehyde are proportional to the inlet concentrations of a challenge chemical compound. It is evident that the formation of by-products generated from incomplete oxidation by UV-PCO is closely related to the nature of a challenge compound. For example, the amount of acetaldehyde produced from PCO of ethanol was 10 times higher the amount produced from other chemical compounds. This is in accordance with the observation made by Hodgson et al. (2007) that the UV-PCO device operated in single-pass mode produced about 1.7 ppm acetaldehyde when challenged with 10 ppm ethanol, while lower than 40 ppb

acetaldehyde was produced when challenged with 10 ppm toluene and acetone. Hence, the major products derived from each chemical compound were different. For example, propinaldehyde and butyraldehyde were the major by-products for PCO of 1-butanol, benzaldehyde for toluene, tolualdehyde for p-xylene, and etc. Bold fonts in Table 4-9 denote distinct by-products observed from UV-PCO of the corresponding VOC at three concentration levels.

In the case that VUV lamps were employed in the absence of an air filter, the detected by-products generated by ozonation were not significantly different from those produced from UV-PCO, but they were generated at lower concentrations. In addition, compared with the UVC-PCO, the involvement of ozone due to the VUV lamps enhanced the mineralization of acetaldehyde and butyraldehyde as a by-product of partially oxidized ethanol and 1-butanol, respectively. This is attributed to more hydroxyl radicals generated from photolysis of ozone. Moreover, usually more by-products were produced when employing the VUV lamps than those using the UVC lamps due to the presence of ozone.

As well known, formaldehyde and acetaldehyde are considered as carcinogens in humans. The concern of the formation of more toxic by-products during the process of UV-PCO makes it necessary to employ a chemisorbent scrubber after a PCO air cleaner in order to reduce the potential health risks and indeed improve IAQ.

Table 4-9 Gas-phase UV-PCO by-products

Compound	UV lamp[a]	Gas-phase UV-PCO by-products detected by HPLC
Ethanol	UVC	Formaldehyde, **acetaldehyde**, acetone
	VUV	Formaldehyde, **acetaldehyde**, crotonaldehyde, propinaldehyde
1-Butanol	UVC	Formaldehyde, acetaldehyde, **propinaldehyde**, **butyraldehyde**
	VUV	Formaldehyde, acetaldehyde, crotonaldehyde, **propinaldehyde**, **butyraldehyde**
Hexane	UVC	Formaldehyde, acetaldehyde, acetone
	VUV	Formaldehyde, acetaldehyde, crotonaldehyde, **propinaldehyde, butyraldehyde**, tolualdehyde, **hexanal**
Octane	UVC	Formaldehyde, acetaldehyde, acetone, **crotonaldehyde, propinaldehyde**, butyraldehyde, valeraldehyde
	VUV	Formaldehyde, acetaldehyde, acetone, **propinaldehyde, butyraldehyde**, (iso)valeraldehyde
Acetone	UVC	Formaldehyde, acetaldehyde
	VUV	Formaldehyde, acetaldehyde
MEK	UVC	Formaldehyde, acetaldehyde, acetone, hexanal
	VUV	Formaldehyde, acetaldehyde, acetone, (iso)valeraldehyde, hexanal
Toluene	UVC	Formaldehyde, acetaldehyde, acetone, crotonaldehyde, butyraldehyde, **benzaldehyde**
	VUV	Formaldehyde, acetaldehyde, acetone, crotonaldehyde, butyraldehyde, propinaldehyde, **benzaldehyde**
p-Xylene	UVC	Formaldehyde, acetaldehyde, acetone, butyraldehyde, **tolualdehyde**, valeraldehyde
	VUV	Formaldehyde, acetaldehyde, acetone, crotonaldehyde, butyraldehyde, **tolualdehyde**, 2,5dimethyl benzaldehyde

Note: (a) UVC (with TiO_2/FGFs). VUV (with TiO_2/FGFs or TiO_2/CCFs or without any filter)

4.8 Major Findings

(1) Adsorption capacity of the tested filters was ranked as: CCFs > TiO_2/CCFs > TiO_2/FGFs.

(2) The test results of TiO_2/FGFs demonstrated that the TiO_2/FGFs filter presented hydrophilic property, and chemical compounds with high polarity showed higher affinity to the surface of TiO_2/FGFs filter. The adsorption capacity of the selected chemical classes ranked as follows: alcohols > ketones > aromatics > alkanes. The test results of

TiO_2/CCFs showed CCFs belonged to a non-polar substrate which preferred to adsorb non-polar chemical compounds.

(3) An increase of RH decreased the adsorption capacity for three tested media attributable to the strong hydrogen bonding for water. In addition, the influence of RH on the adsorption behavior of TiO_2/CCFs was less important than that on TiO_2/FGFs.

(4) Due to the differences in adsorption performance, photocatalytic activity of the TiO_2/CCFs air filter was obviously higher than that of TiO_2/FGFs.

(5) An innovative UV-PCO duct system experimental set-up was designed and constructed, and in-duct test methodologies were developed to investigate the performance of the UV-PCO air cleaners for the various VOCs removal. The single-pass removal efficiency of two types of air filters (TiO_2/FGFs and TiO_2/CCFs) under UVC or UVV illumination in removing the VOCs with various properties ranks as follows: alcohols > ketones > aromatics > alkanes.

(6) It was observed that the PCO removal efficiency increased by decreasing of the inlet concentration, reducing the airflow rate, increasing of the irradiance, or decreasing of RH, respectively. Competition of adsorption sites, bond energy, residence time, and the number of effective hydroxyl radicals are new interpretations of these observations based on a fundamental analysis of reaction mechanisms.

(7) It was investigated that the ozone played a critical role in the removal of alkanes, alcohols, and aromatics at three concentration levels, and the ozone removal efficiency reduced with an increase in the inlet concentrations of a challenge chemical compound. Additionally, the conversion rates of various VOCs increased with ozone concentrations. Furthermore, the conversion rates of the VOCs by the VUV-PCO were higher than that

by the UVC-PCO due to the presence of ozone.

(8) Formation of by-products had a close relationship with the PCO reaction mechanisms of different VOCs. The appearance and the concentrations of the by-products depended on the experimental conditions, the nature of a challenge VOC, as well as the characteristics of the catalysts. Therefore, by knowing the intrinsic kinetics, the design of a PCO air purifier working under optimal conditions can reduce the generation of by-products, which is the future research direction to enhance the practicability of PCO technology.

5. PHOTOCATALYTIC OXIDATION MODEL DEVELOPMENT AND VALIDATION

5.1 Introduction

Photocataytic degradation of indoor air pollutants is a complex physico-chemical process, and the catalytic reaction rate is an essential gauge of the efficiency of a UV-PCO system. Simple kinetic models are different order of empirical models, which assume the concentrations of reacting species in air as the driving force for the PCO reaction. The effects of the rest of aforementioned UV-PCO parameters are lump-summed into a reaction rate constant as well as the order of reaction (Zhang et al., 2003; Yang et al., 2005). In contrast, the models that assume the concentrations of adsorbed species on the catalyst as the driving force can separately account for the effects of pollutant mixtures, oxygen and moisture levels, as well as the concentration of reactants. Several studies (Obee, 1996, Chen et al., 2005) applied different forms (e.g., unimolecular with or without interference effects of mixture, and bimolecular) of Langmuir-Hinshelwood (L-H) model, which retains the assumptions underlying the Langmuir adsorption isotherm. L-H model, however, cannot explicitly describe UV irradiation or mass transfer of reactants in the bulk fluid and porous structure of the catalyst.

Experimental evaluation of UV-PCO technology for air purification has been conducted in Chapter 4 and the results reveal the effects of the experimental and operational variables on the photocatalytic conversion. In this chapter, a mathematical UV-PCO model is developed by integrating light scattering model, reaction kinetic model,

mass balance as well as optional ozonation model. The proposed UV-PCO model has applied to predict the PCO performance for eight VOCs removal in a pilot-scale system using TiO_2 as the photocatalyst for the model validation.

5.2 Model Assumptions

The considered PCO reactor is integrated into a mechanical ventilation system, and UV lamps with peak wavelengths of UVC and VUV are positioned in front of and parallel to the filter surface coated with titanium dioxide (TiO_2). The following fundamental mechanisms are considered in the development of an in-duct UV-PCO modeling:

- The distribution of photo energy within ducts and interaction between light and matter at the surface of catalyst;
- Convection, diffusion, and boundary transfer of contaminants in the air-phase;
- Adsorption and photocatalytic oxidation reaction on the solid-phase;
- Inter-phase mass transfer of reactant species.

A schematic representation of the UV-PCO reactor with different configurations is shown in Figure 5-1. The UV-PCO model is developed on the basis of fundamental mechanisms involved in UV-PCO technology (Figure 5-1(a), UVC lamps with TiO_2 air filters). Several assumptions are applied in the development of the UV-PCO model.

(1) The PCO reaction occurs at the surface of the catalyst fibers exposed to the UV lights. The function of the UV-PCO banks is to extend the PCO reaction surface and the concentration difference between banks is not considered.

(2) Photons reaching to the TiO_2 are totally adsorbed by the catalyst. Irradiance does

not pass through the air filter and the average irradiance is considered for each bank.

(3) The TiO_2 catalysts are uniformly coated at the fiberglass.

(4) The air flow in duct is deemed as ideal plug flow.

(5) UV light is assumed to be monochromatic since approximate 95% of the UV energy emitted from the germicidal lamps is at the mercury resonance wavelength of 254 nm.

(6) By neglecting the sink effect of the test rig, the measured downstream concentration is the same as the outlet concentration once the effluent gas passes through the PCO air filters.

An ozonation model is also developed when the VUV lamps are employed without the TiO_2 air filters (Figure 5-1 (b)). In this scenario, ozone generated from the VUV lamps is considered as a powerful oxidizing agent, which reacts with VOCs. The following assumptions are also made in the process of developing an ozonation model:

(1) Reaction with ozone is a homogeneous gas-phase reaction.

(2) Photolysis effect on the degradation of VOCs is negligible.

(3) By neglecting the sink effect of the test rig, the VOC concentration difference between upstream and downstream is attributed to the ozonation effect.

The UV-PCO model and the ozonation model are concatenated to simulate VUV lamps with TiO_2 air filters in an in-duct system (Figure 5-1 (c)). These two models are applied in accordance with the order of the actual processes involved in the ozone-assisted UV-PCO, that is, VOC is photocatalytic oxidized by UV-PCO technology followed by further oxidation with ozone. It should be noted that although the presence of

high concentration of ozone is within the UV-PCO reactor, the ozonation effect is not to be considered due to its very short contact time with VOC. Since the UV-PCO and the ozonation are continuous processes, the predicted outlet concentration by the UV-PCO model is the inlet concentration for the ozonation model.

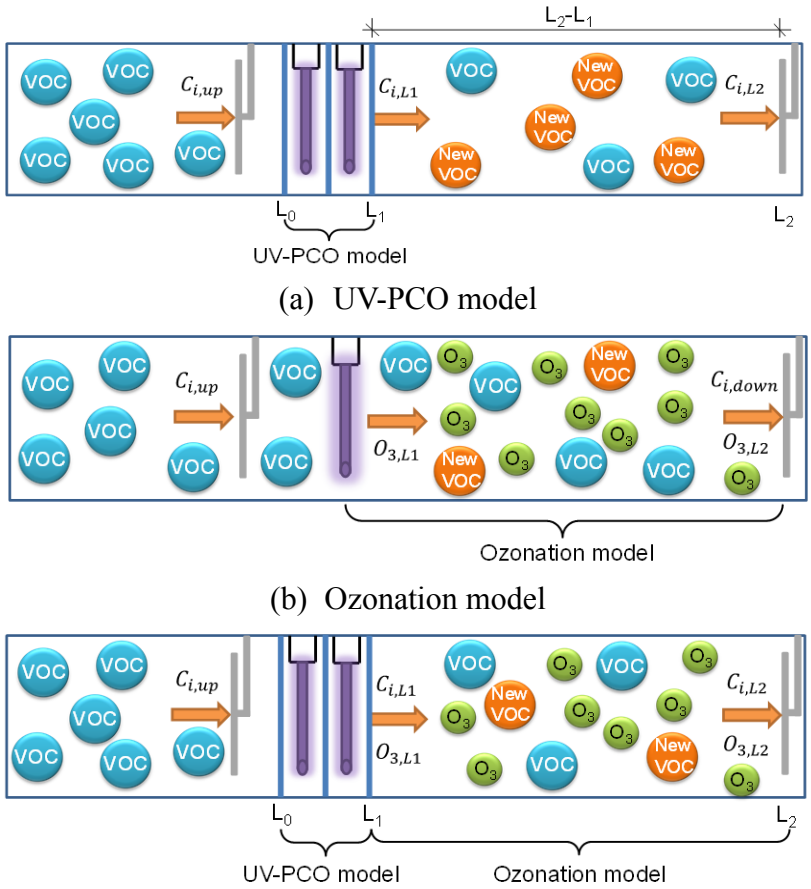

(a) UV-PCO model

(b) Ozonation model

(c) Combination of UV-PCO model and ozonation model

Figure 5-1 Schematic diagrams of UV-PCO system for various scenarios: (a) UVC lamps with TiO_2 air filters (b) VUV lamps in the absence of TiO_2 air filters (c) VUV lamps with TiO_2 air filters

5.3 Model Description

5.3.1 UV Irradiance Field Model

Existing UV irradiance models mostly assumed a uniform irradiance on the surface

of TiO_2. In reality, it is difficult to provide a uniform irradiance from UV lamps due to reflection, soiling effect and shadowing effect. In this model, the irradiation on the catalyst surface is attributed from two parts: one is photon transmittance direct from light source; another is the photons reflected from interior duct walls. The principle of view factor from radiative heat transfer, which has been commonly used in several models (Ozisik, 1973; Siegel and Howell, 1992; Hossain and Raupp, 1998; Hossain and Raupp, 1999), is also introduced in our model. Here, view factor, F(M,N), is the proportion of all radiation which leaves surface M and strikes surface N. Using this method, the contributions of irradiation of two parts to the element of TiO_2 surfaces are easily and accurately estimated.

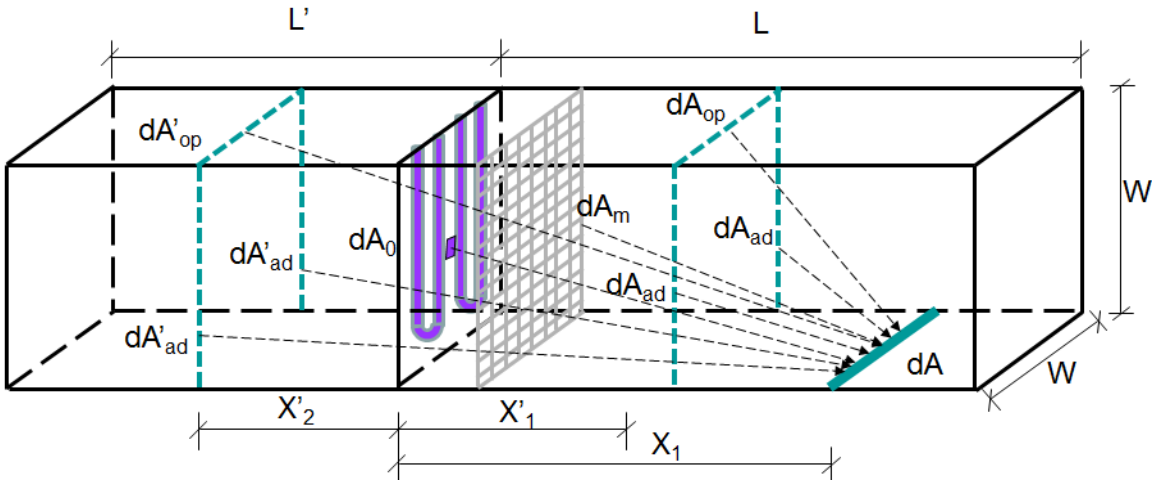

Figure 5-2 Schematic diagram of square duct demonstrating the spectral intensity contributions of differential areas to a differential wall strip element dA

The mathematical expression of the spectral intensity $I_w(\lambda)$ to the wall surface is shown below:

$$I_w(\lambda) = \int_{A_0} I_0(\lambda)\cdot dF(dA_0, dA) + 2\rho(\lambda)\int_{A_{ad}} I_w(\lambda)\cdot dF(dA_{ad}, dA) + \rho(\lambda)\int_{A_{op}} I_w(\lambda)\cdot dF(dA_{op}, dA)$$
$$+ 2\rho(\lambda)\int_{A'_{ad}} I_w(\lambda)\cdot dF(dA'_{ad}, dA) + \rho(\lambda)\int_{A'_{op}} I_w(\lambda)\cdot dF(dA'_{op}, dA) \qquad [5\text{-}1]$$

where ρ is the wall reflectivity which depends on the incident wavelength, dF are differential view factors for different areas (Figure 5-2), and $I_0(\lambda)$ is the intensity of an incident UV light. The first term is the contribution of direct illumination from all the infinitesimal dA_0 area composing the plane of UV light. The remaining terms are the contributions of indirect illumination from adjacent and opposing wall surfaces on both sides of UV source.

If we introduce dimensionless UV intensity $\Phi_w(\lambda) = I_w(\lambda)/I_0(\lambda)$ to the wall surface, Eq. (5-1) changes to:

$$\Phi_w(\lambda) = F(A_0, dA) + 2\rho(\lambda)\int_{A_{ad}} \Phi_w(\lambda)\cdot dF(dA_{ad}, dA) + \rho(\lambda)\int_{A_{op}} \Phi_w(\lambda)\cdot dF(dA_{op}, dA) + 2\rho(\lambda)\int_{A'_{ad}} \Phi_w(\lambda)\cdot dF(dA'_{ad}, dA) + \rho(\lambda)\int_{A'_{op}} \Phi_w(\lambda)\cdot dF(dA'_{op}, dA) \quad [5\text{-}2]$$

where F is integral view factor. Eq. (5-2) is a Fredholm equation of the second kind, which is the solution to find the implicit function of Φ_w when F and dF are given.

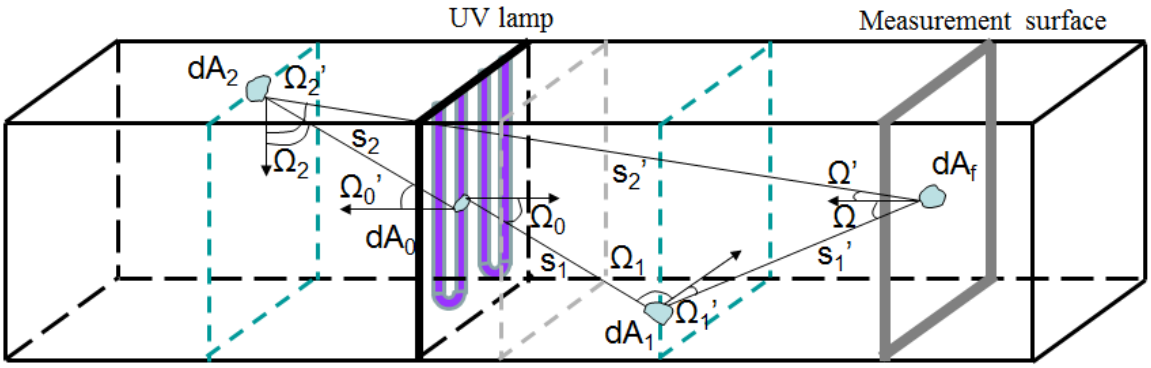

Figure 5-3 View factor associated with the radiation heat exchange between two elemental surfaces of area

According to the thermal radiation theory, the view factor is geometrically determined, and it can be expressed between two elemental surface of area dA_0 and dA_1 in a mathematical way:

$$dF(dA_0, dA_1) = \frac{\cos\Omega_0 \cos\Omega_1}{\pi s_1^{\,2}} dA_1 \qquad [5\text{-}3]$$

where Ω_0 and Ω_1 are the angles between the connecting line and the normal vectors of area dA_0 and dA_1, respectively, and s_1 is the length of the connecting line.

Similarly, the expression of differential view factors for the other pairs of elemental areas (Figure 5-3) can be described as follows:

$$dF(dA_1, dA_f) = \frac{\cos\Omega_1' \cos\Omega}{\pi s_1'^{2}} dA_f \qquad [5\text{-}4]$$

$$dF(dA_0, dA_2) = \frac{\cos\Omega_0' \cos\Omega_2}{\pi s_2^{\,2}} dA_2 \qquad [5\text{-}5]$$

$$dF(dA_2, dA_f) = \frac{\cos\Omega_2' \cos\Omega'}{\pi s_2'^{2}} dA_f \qquad [5\text{-}6]$$

The derived equations of dimensionless integral and differential view factors on one side of the UV source can be written as (Siegel and Howell, 1992; Worth et al., 1996):

$$F(A_0, dA) = \frac{1}{\pi}\left[\tan^{-1}\frac{1}{X_1} + \frac{X_1}{2}\ln\frac{X_1^{\,2}(X_1^{\,2}+2)}{(X_1^{\,2}+1)^2} - \frac{X_1}{(X_1^{\,2}+1)^{1/2}}\tan^{-1}\frac{1}{(X_1^{\,2}+1)^{1/2}}\right] \qquad [5\text{-}7]$$

$$dF(dA_{op}, dA) = \frac{1}{\pi}\left(\left|X_1 - X_1'\right|^2 + 1\right)^{-3/2} \times \tan^{-1}\frac{1}{\left(\left|X_1 - X_1'\right|^2 + 1\right)^{1/2}} dX_1' \qquad [5\text{-}8]$$

$$dF(dA_{ad}, dA) = -\frac{1}{4\pi}\ln\frac{\left|X_1 - X_1'\right|^2\left(\left|X_1 - X_1'\right|^2 + 2\right)}{\left(\left|X_1 - X_1'\right|^2 + 1\right)^2} dX_1' \qquad [5\text{-}9]$$

Here, $X_1 = x_1 / W, X_1' = x_1' / W (0 < X_1, X_1' < \frac{L}{W})$, and $X_2' = x_2' / W (0 < X_1' < \frac{L'}{W})$. W is the length size of the cross section of the square duct. Similarly, equations of

dimensionless integral and differential view factors on the other side of the UV source can be derived:

$$dF(dA_{op}^{'}, dA) = \frac{1}{\pi}(\left|X_1 + X_2^{'}\right|^2 + 1)^{-3/2} \times \tan^{-1} \frac{1}{(\left|X_1 + X_2^{'}\right|^2 + 1)^{1/2}} dX_2^{'} \qquad [5\text{-}10]$$

$$dF(dA_{ad}^{'}, dA\ ) = -\frac{1}{4\pi} \ln \frac{\left|X_1 + X_2^{'}\right|^2 (\left|X_1 + X_2^{'}\right|^2 + 2)}{(\left|X_1 + X_2^{'}\right|^2 + 1)^2} dX_2^{'} \qquad [5\text{-}11]$$

By substituting Eq. (5-7)-(5-11) into Eq. (5-2), dimensionless UV intensity Φ_w to the wall surface can be solved. Then, the mathematical expression of the spectral intensity $I_f(\lambda)$ to the fibrous filter coated with TiO_2 (Figure 5-4) is determined as follows:

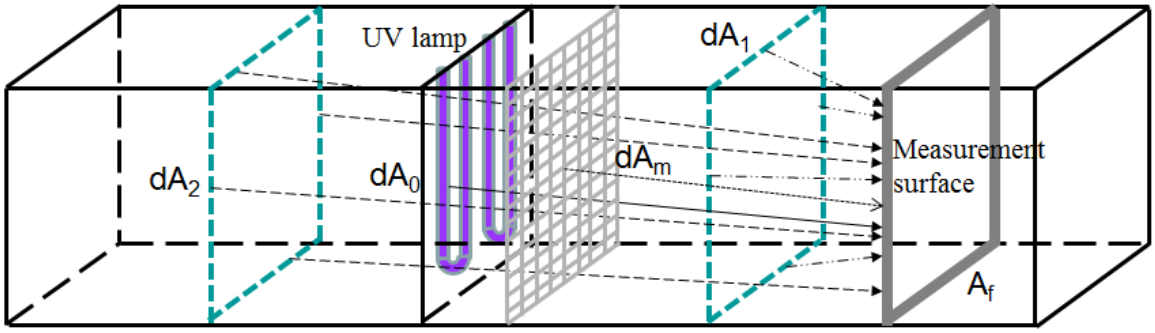

Figure 5-4 Schematic diagram of square duct demonstrating the spectral intensity contributions of differential areas to a purification filter with area A_f

$$I_f(\lambda) = \int_{A_0} I_0(\lambda) \cdot dF(dA_0, A_f) + 4\rho(\lambda) \int_{A_1} I_w(\lambda) \cdot dF(dA_1, A_f) + 4\rho(\lambda) \int_{A_2} I_w(\lambda) \cdot dF(dA_2, A_f) \qquad [5\text{-}12]$$

If we introduce dimensionless UV intensity $\Phi_f(\lambda) = I_f(\lambda) / I_0(\lambda)$ to the filter surface, Eq. (5-12) rearranges its form to:

$$\Phi_f(\lambda) = F(A_0, A_f) + 4\rho(\lambda) \int_{A_1} \Phi_w(\lambda) \cdot dF(dA_1, A_f) + 4\rho(\lambda) \int_{A_2} \Phi_w(\lambda) \cdot dF(dA_2, A_f) \qquad [5\text{-}13]$$

Here, dimensionless integral and differential view factors for different areas are also

provided by Siegel and Howell (1992).

$$F(A_0, A_f) = \frac{2X_1^{\,2}}{\pi}\left[\ln\frac{X_1^{\,2}+1}{X_1\sqrt{X_1^{\,2}+2}} + \frac{2}{X_1^{\,2}}\sqrt{X_1^{\,2}+1}\times\tan^{-1}\frac{1}{\sqrt{X_1^{\,2}+1}} - \frac{2}{X_1}\tan^{-1}\frac{1}{X_1}\right] \quad [5\text{-}14]$$

$$dF(dA_1, A_f) = \frac{1}{\pi}\left[\tan^{-1}\frac{1}{\left|X_1 - X_1^{'}\right|} + \frac{\left|X_1 - X_1^{'}\right|}{2}\times\ln\frac{\left|X_1 - X_1^{'}\right|^2\left(\left|X_1 - X_1^{'}\right|^2 + 2\right)}{\left(\left|X_1 - X_1^{'}\right|^2 + 1\right)^2}\right.$$
$$\left. - \frac{\left|X_1 - X_1^{'}\right|}{\left(\left|X_1 - X_1^{'}\right|^2 + 1\right)^{1/2}}\times\tan^{-1}\frac{1}{\left(\left|X_1 - X_1^{'}\right|^2 + 1\right)^{1/2}}\right]dX_1^{'} \quad [5\text{-}15]$$

$$dF(dA_2, A_f) = \frac{1}{\pi}\left[\tan^{-1}\frac{1}{\left|X_1 + X_2^{'}\right|} + \frac{\left|X_1 + X_2^{'}\right|}{2}\times\ln\frac{\left|X_1 + X_2^{'}\right|^2\left(\left|X_1 + X_2^{'}\right|^2 + 2\right)}{\left(\left|X_1 + X_2^{'}\right|^2 + 1\right)^2}\right.$$
$$\left. - \frac{\left|X_1 + X_2^{'}\right|}{\left(\left|X_1 + X_2^{'}\right|^2 + 1\right)^{1/2}}\times\tan^{-1}\frac{1}{\left(\left|X_1 + X_2^{'}\right|^2 + 1\right)^{1/2}}\right]dX_2^{'} \quad [5\text{-}16]$$

Compared with the previously developed irradiance models (Hossain and Raupp, 1998, 1999; Hossain et al., 1999; Alexiadis, 2006), the advantage of this new UV irradiance model is that the contributions of wall surface on left and right side of the UV light are considered, because UV sources are always mounted within a duct of HVAC systems. Therefore, this model accurately simulates the actual distribution of UV irradiation in an in-duct air purification system.

5.3.2 Mass Balance

Because the thickness of the porous TiO_2 film is thin compared to the fibrous supporting structure, the PCO filter is regarded as two flat lamellas closely linked, which was proved valid by Edwards et al. (1996) and Changrani and Raupp (2000). Figure 5-5 shows the geometry of the photocatalytic system.

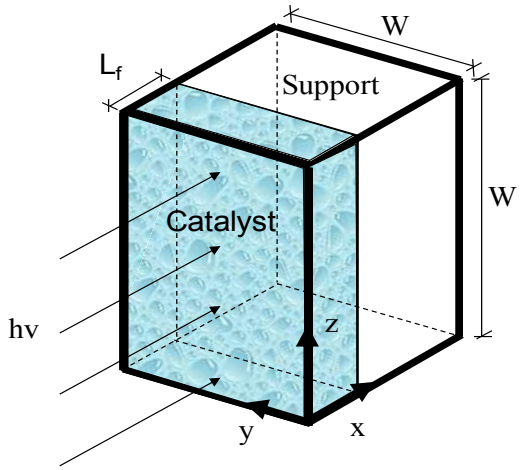

Figure 5-5 Schematic diagram of geometry of the photocatalytic system, catalyst film combined with fibrous support

The mass conservation equation for species i in air-phase is stated as following:

Rate of accumulation of mass + Rate of mass in

= Rate of mass out (main diffusion) + Rate of mass out (boundary transfer) [5-17]

Combined with Fick's law of mass diffusion, the mathematical expression of mass transfer for species i is given by:

$$\underbrace{\frac{\partial c_{iB}}{\partial t}}_{\text{Rate of accumulation}} + \underbrace{\frac{\partial (c_{iB}u_x)}{\partial x} + \frac{\partial (c_{iB}u_y)}{\partial y} + \frac{\partial (c_{iB}u_z)}{\partial z}}_{\text{Convective transport}} = \underbrace{D_{ei}\left(\frac{\partial^2 c_{iB}}{\partial x^2} + \frac{\partial^2 c_{iB}}{\partial y^2} + \frac{\partial^2 c_{iB}}{\partial z^2}\right)}_{\text{Diffusive transport}} \underbrace{- k_g a (c_{iB} - c_{iS})}_{\text{Boundary transfer}} \quad [5\text{-}18]$$

where C_{iB} is the bulk concentration of species i (mol/m^3); C_{iS} is the absorbed concentration of species i (mol/m^3) at the surface of catalyst; u_x, u_y and u_z are the velocity vector in x, y, and z direction, respectively; t is time (s); k_g is the inter-phase mass transfer coefficient (m/s); a is the geometric surface area per unit reactor volume (m^2/m^3); D_{ei} is the effective diffusion coefficient of species i (m^2/s).

Since we assume that the air flow in ducts is regarded as ideal plug flow, it is achieved by adding a mesh at the entrance of the upstream, which makes the velocity to

be constant across any cross-section of the duct. So, the lateral component of air flow velocities u_y and u_z are absent and no concentration gradients exist in both directions.

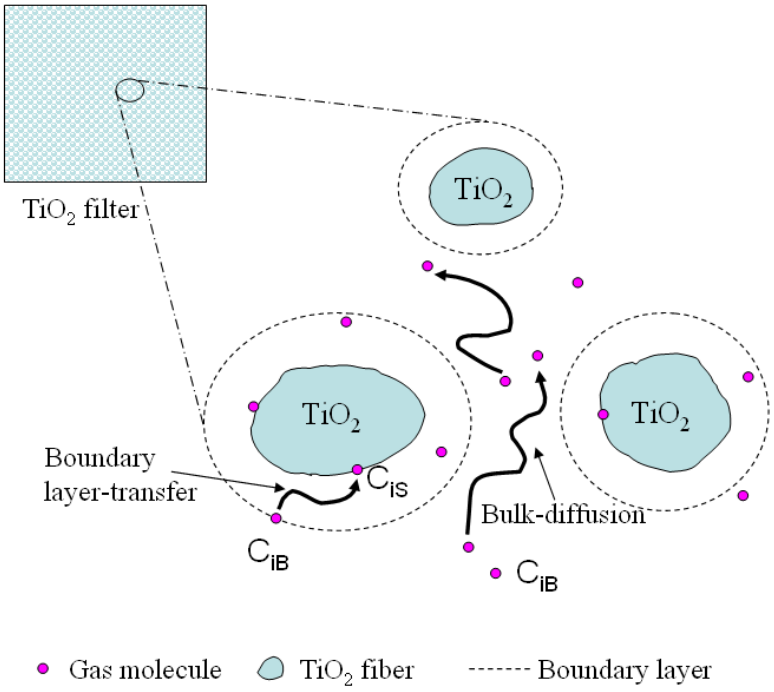

Figure 5-6 Schematic diagram of gas molecule transfer in the inter-fiber (air-phase) and at the surface of fibers (solid-phase)

Under this assumption, the mass balance of species i in the inter-fiber (air phase) (Figure 5-6) is simplified as follows:

$$\frac{\partial c_{iB}}{\partial t} + \frac{u_x \partial c_{iB}}{\partial x} = D_{ei}\left(\frac{\partial^2 c_{iB}}{\partial x^2} + \frac{\partial^2 c_{iB}}{\partial y^2} + \frac{\partial^2 c_{iB}}{\partial z^2}\right) - k_g a(c_{iB} - c_{iS})$$

$$= \frac{\varepsilon}{\tau} D_{mi}\left(\frac{\partial^2 c_{iB}}{\partial x^2} + \frac{\partial^2 c_{iB}}{\partial y^2} + \frac{\partial^2 c_{iB}}{\partial z^2}\right) - k_g a(c_{iB} - c_{iS}) \qquad [5\text{-}19]$$

Similarly, the mass balance of species i at the surface of fibers (solid phase) (Figure 5-6) is

$$\frac{\partial C_{iS}}{\partial t} = k_g a(C_{iB} - C_{iS}) - \bar{r}_i \qquad [5\text{-}20]$$

The initial and boundary conditions are

$$C_{iB} = C_{iS} = 0 \quad \text{at} \quad t = 0 \qquad [5\text{-}21]$$

$$C_{iB} = C_{in} \quad \text{at} \quad x = 0 \qquad [5\text{-}22]$$

$$C_{Bn} = C_{out} \quad \text{at} \quad x = L_f \qquad [5\text{-}23]$$

$$\frac{\partial C_{iB}}{\partial y} = 0 \quad \text{at} \quad y = 0 \quad \text{or} \quad y = W \qquad [5\text{-}24]$$

$$\frac{\partial C_{iB}}{\partial z} = 0 \quad \text{at} \quad z = 0 \quad \text{or} \quad z = W \qquad [5\text{-}25]$$

where C_{in} is the inlet concentration of species i (mol/m^3); C_{out} is the outlet concentration of species i (mol/m^3); W is the side length of square cross section (m); u_x is the inlet axial velocity in the duct (m/s); ε is the porosity of the catalyst; τ is the tortuosity of the catalyst; D_{mi} is the molecular diffusion coefficient of species i (m^2/s); $\overline{r_i}$ is the PCO reaction mean rate (mol/s m^3).

5.2.3 Reaction Kinetic Model

The determination and evaluation of kinetic parameters in a photocatalytic reaction rate model is based on the fundamental mechanisms of PCO and is one of the main obstacles for the practical application of a mathematical model of the PCO reaction. The simple representation of destruction process is

$$i + hv \rightarrow (\xi_1 i1 + \ldots + \xi_j ij + \ldots + \xi_m im) + CO_2 + H_2O \qquad [5\text{-}26]$$

where ij is the PCO intermediates of species i; ξ_j is the stoichiometric coefficient of species i in the jth reaction. Based on this mechanism, a new Langmuir-Hinshelwood reaction rate equation is developed as a means of modeling the mean PCO reaction rate of species i removal, which is given by

$$-\bar{r}_i = \bar{\sigma}(I_f)^{\beta} \frac{k_0 K_i c_{iS}}{1 + K_i c_{iS}} \qquad [5\text{-}27]$$

If we consider competition of intermediates j at the catalyst surface, the mean removal rate r_i changes to:

$$-\bar{r}_i = \bar{\sigma}(I_f)^{\beta} \frac{k_0 K_i c_{iS}}{1 + K_i c_{iS} + \sum_{j=1}^{m} K_{ij} c_{iSj}} \qquad [5\text{-}28]$$

where I_f is UV light intensity at the filter surface (W/m^2); β is the reaction order with respect to UV light applied; k_0 is the reaction rate constant ($mg/m^3/s$) that takes into account all other factors that may affect the rate; K_i and K_{ij} are adsorption equilibrium constant (m^3/mol) of species i and intermediates ij at TiO_2 surface, respectively; C_{iB} and C_{iBj} are the concentration (mol/m^3) of species i and intermediates ij at boundary layer, respectively; $\bar{\sigma}$ is the effectiveness factor of the photocatalyst, which needs to be discussed as follows.

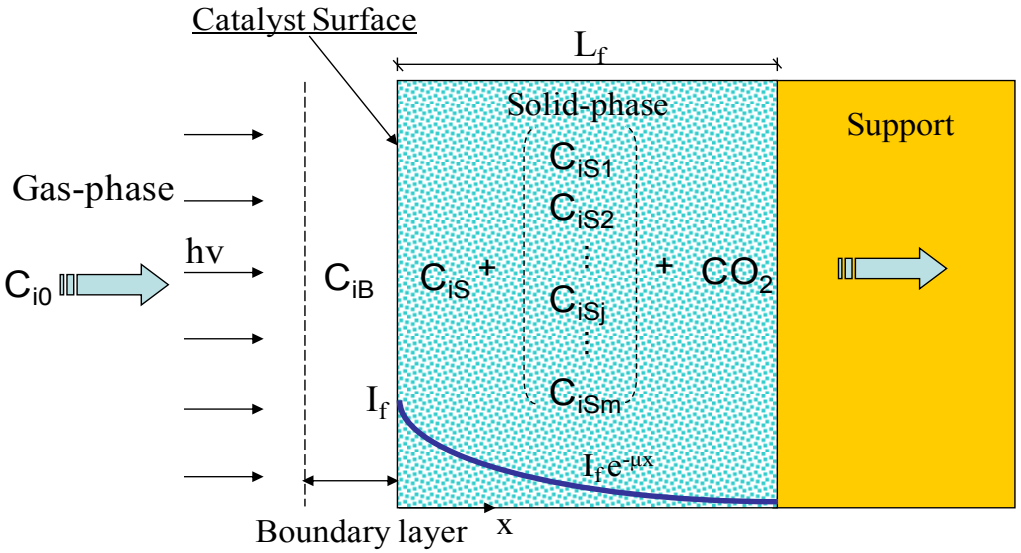

Figure 5-7 Schematic diagram of PCO reaction in the PCO reactor

Considering the irradiance distribution within the catalyst is non-uniform, that is, the

irradiance within the catalyst is smaller than that at the external surface, the effectiveness factor $\bar{\sigma}$ of the photocatalyst is used to evaluate the mean efficiency of the entire catalyst (Figure 5-7), which is defined by Hill (1977):

$\bar{\sigma}$ =actual rate for the entire catalyst/ rate evaluated at external surface [5-29]

Assuming the local species i concentration and a global kinetic rate constant of the degradation reaction do not vary with position in the catalyst and irradiance within the catalyst is exponentially attenuated, the effectiveness factor $\bar{\sigma}$ of the geometry of interest is expressed

$$\bar{\sigma} = \frac{\int_0^{L_f} r_{ix} dx}{L_f r_{i0}} = \frac{\int_0^{L_f} (I_f e^{-\mu L_f x})^{\beta} dx}{L_f (I_f)^{\beta}} = \frac{\int_0^{L_f} (e^{-\mu L_f x})^{\beta} dx}{L_f} \quad , \qquad [5\text{-}30]$$

where r_{i0} is the PCO rate at external surface (mol/m^{3}s); r_{ix} is the PCO rate within the catalyst (mol/m^{3}s); μ is the extinction coefficient per unit thickness of the film (μm^{-1}). In this case, the extinction coefficient is set to a typical value of 0.3 μm^{-1} (Changrani and Raupp, 2000), L_f is the thickness of catalyst (μm).

5.3.4 Ozonation Model

When ozone producing UV lamps are employed in the PCO reactor, the removal of indoor air pollutants by ozonation needs to be evaluated quantitatively. The ozonation model is to provide an approximation for the removal rate of the VOCs in the reaction with ozone.

$$O_3 + VOC \rightarrow Products \qquad [5\text{-}31]$$

In general, the kinetics of reactions of ozone with organic compounds is shown to be second order (Bailey, 1982). Hence,

$$-\frac{dC_i}{dt} = k_{O_3,i} C_{O_3} C_i \quad [5\text{-}32]$$

Through integration, the rate constant $k_{O3,i}$ is then obtained from the expression

$$k_{O_3,i} = \frac{\ln C_{i,up} - \ln C_{i,down}}{C_{O_3,ave} \frac{L_2 - L_1}{u_x}} \quad [5\text{-}33]$$

Since UV lamps, as an ozone producing source, are installed within the flow system, and the ozone production depends on the number of the VUV lamps, oxygen and moisture levels and airflow rate in duct, the traditional observation method for ozone decays in a closed system is not feasible in this study. In addition, the reaction time calculated from the airflow rate and the duct dimensions is very short (less than 2 seconds). It is reasonable to assume the ozone concentration continuously tested at downstream stands for the average ozone concentration throughout the reaction. Then, Eq. (5-33) turns into

$$k_{O_3,i} = \frac{\ln C_{i,up} - \ln C_{i,down}}{C_{O_3,L2} \frac{L_2 - L_1}{u_x}} \quad [5\text{-}34]$$

For the ozone-assisted UV-PCO, the downstream concentration of a challenge gas is estimated by combination of the UV-PCO model and the ozonation model.

5.3.5 PCO Reactor Model

With the above discussion, a Langmuir-Hinshelwood model combined with an irradiance field model, a mass transfer model as well as an optional ozonation model is developed to closely reflect the actuality of photocatalytic reaction. To make a model easy to run on a personal computer using readily available software such as Matlab, the PCO model is simplified to a 1-D model for a single contaminant with no competitions of intermediates. PCO dynamics of a single contaminant in fibrous TiO_2 film is described by

two equations, one representing the mass balance of the contaminant in the inter-fiber air-phase, and the other representing the mass balance at the surface of the TiO_2 catalyst. The summarized governing equations for the PCO reactor model as well as the ozonation model are:

Gas phase:

$$\frac{dC_{i,B}}{dt} = \frac{\varepsilon}{\tau} D_{i,m} \frac{d^2 C_{i,B}}{dx^2} - u_x \frac{dC_{i,B}}{dx} - k_{i,g} a (C_{i,B} - C_{i,S}) \quad [5\text{-}35]$$

Catalyst phase:

$$\frac{dC_{i,S}}{dt} = k_{i,g} a \left(C_{i,B} - C_{i,S}\right) - \frac{\int_0^{L_f} \left(exp^{-\mu L_f x}\right)^{\beta} dx}{L_f} I_f{}^{\beta} \frac{k_i K_i C_{i,S}}{1 + K_i C_{i,S}} \quad [5\text{-}36]$$

Ozonation (optional):

$$\ln C_{i,down} = \ln C_{i,out} - k_{O_3,i} C_{O_3} \frac{L_2 - L_1}{u_x} \quad [5\text{-}37]$$

Initial and boundary conditions:

$$C_B = C_S = 0 \text{ at } t = 0 \quad [5\text{-}38]$$

$$C_{B0} = C_{up} \text{ at } x = L_0 \quad [5\text{-}39]$$

$$C_{Bn} = C_{L_1} \text{ at } x = L_1 \quad [5\text{-}40]$$

5.4 PCO Model Parameters

The key parameters in the PCO model come from catalyst properties (porosity, tortuosity, surface area, and film thickness), mass transfer (molecular diffusion coefficient and mass transfer coefficient), kinetic parameter (PCO reaction rate constant, adsorption coefficient, and ozonation kinetic rate constant) and irradiance parameter (UV irradiance extinction coefficient, reaction order with respect to irradiance, and reflectivity). Once these parameters are obtained from experimental results or estimated from the existing

literature, the predicted performance of the PCO air cleaners can be evaluated for given values of the operational conditions.

5.4.1 Catalyst Properties

The effective diffusivity within a porous air cleaning filter considers the factor of porosity and tortuosity on the amendment of the free diffusion of reactants, which accounts for the effect of altered diffusion path length as well as different cross-sectional areas in constrictions. The porosity of 0.65 was determined based on the scanning electron microscopy (SEM) images of TiO_2/FGFs surfaces (see Figure 4-11 (a)) using OriginPro 8 (OriginLab Corporation) with two-dimensional volume integrated method. Figure 5-8 presents the three-dimensional surface of TiO_2/FGFs predicted by OriginPro 8 software, which provided the dimensions to calculate the volume beneath the sample's surface (V_{solid}) and the volume beneath the flat surface (V_{total}), and consequently to determine the porosity ($\varepsilon=1-V_{solid}/V_{total}$). For completely random pore orientations, the random pore model (Froment and Bischoff, 1979) predicted that the tortuosity depends only on the angle of the pores with the fibers axis and gave a value of 3 which is a common value for most catalyst materials (Satterfield, 1970). Also, for an isotropic medium, tortuosity factor should have a value of 3 (Dullien, 1992). Hence, this typical value was taken in this study. Table 5-1 shows the summarized physical properties of the TiO_2/FGFs filter.

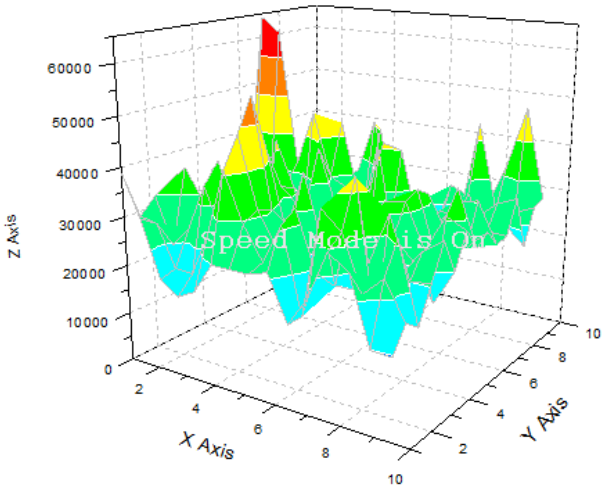

Figure 5-8 Three dimensional surface of TiO_2/FGFs predicted by OriginPro 8 software (x, y and z are the dimensions of the projected surface).

Table 5-1 Physical properties of TiO_2/FGFs air filters

Porosity, ε	Tortuosity, τ	Diameter, μm	BET, m^2/g	TiO_2 layer thickness, L_f (μm)
0.65	3	90	105.7	5

For the PCO reactor arranged in one bank, a value of 2.0 m^{-1}, apparent catalyst surface area per unit PCO reactor volume, was calculated on the basis of known geometrical size of the rectangular PCO reactor (Figure 3-2). A value of 4.0 m^{-1} was taken for the PCO reactor arranged in two banks.

5.4.2 Mass Transfer

5.4.2.1 Molecular Diffusion Coefficient

The method developed by Wilke and Lee (1955) (WL method) is commonly used to estimate gaseous diffusion coefficients for a wide range of compounds and temperature, and it is more accurate than the other reported methods (Lyman et al., 1990). WL method

described that the diffusion of gases by intermolecular collision is a function of temperature (T), the molecular weight (M_r), the collision integral (Ω), the pressure (P), and the characteristic length (σ_{AB}) of molecule A interacting with molecule B, according to the following equation:

$$D_{BA} = \frac{B' T^{3/2} \sqrt{M_r}}{P \sigma_{AB}^2 \Omega} \quad , \qquad [5\text{-}41]$$

where $B' = 0.00217 - 0.00050 \sqrt{\frac{1}{M_A} + \frac{1}{M_B}}$

$M_{r=} (M_A + M_B)/M_A M_B$, M_A= 28.97g/mol (A=air)

P = pressure (atm)

T = temperature (K)

The collision integral, Ω, is a function of molecular energy of attraction, ε, and the Boltzmann constant, k, as shown in following equations,

$$\Omega = \frac{a}{(T^*)^b} + \frac{c}{e^{T^* d}} + \frac{e}{e^{T^* f}} + \frac{g}{e^{T^* h}} \quad , \qquad [5\text{-}42]$$

where the values of a-h are as follows:

a=1.06036 c=0.19300 e=1.03587 g=1.76474

b=0.15610 d=0.47635 f=1.52996 h=3.89411

and $T^* = \frac{T}{(\varepsilon/k)_{AB}}$ $(\varepsilon/k)_{AB} = \sqrt{(\varepsilon/k)_A (\varepsilon/k)_B}$

where $(\varepsilon/k)_A = 78.6K$ and $(\varepsilon/k)_B = 1.15 T_b(k)$ T_b= boiling point of compound B

The characteristic length, σ_{AB}, is a function of the molar volume at the boiling point:

$$\sigma_{AB} = \frac{\sigma_A + \sigma_B}{2} \quad , \qquad [5\text{-}43]$$

where $\sigma_A = 3.711$Å and $\sigma_B = 1.18 (V_B')^{1/3}$

V_B'=LeBas molar volume of compound B, the value of V_B' is shown in Table 5-2

Table 5-2 Additive volume increments for calculating LeBas molar volume, V_B'

Atom	Increment (cm^3/mol)	Atom	Increment (cm^3/mol)
C	14.8	Br	27.0
H	3.7	Cl	24.6
O (except as noted below)	7.4	F	8.7
In methyl esters and ethers	9.1	I	37.0
In ethyl esters and ethers	9.9	S	25.6
In higher esters and ethers	11.0	Ring	
In acids	12.0	3-Membered	-6.0
Joined to S, P, N	8.3	4-Membered	-8.5
N		5-Membered	-11.5
Double bonded	15.6	6-Membered	-15.0
In primary amines	10.5	Naphthalene	-30.0
In secondary amines	12.0	Anthracene	-47.5

Based on the WL method described above, the calculations of the VOC diffusion coefficients at room temperature are shown in Table 5-3.

Table 5-3 Diffusion coefficients of VOCs (Molar mass and boiling point refer to NIOSH, 2010)

Name	Formula	M_B (g/mol)	T_b (K)	V_B' (cm^3/mol)	σ_B (Å)	σ_{AB} (Å)	$(\varepsilon/k)_B$ (K)	$(\varepsilon/k)_{AB}$ (K)	T*	B'	M_r	Ω	D_{BA} (cm^2/s)
Toluene	C_7H_8	92.14	383.75	118.2	5.79	4.75	441.31	186.24	1.60	0.00206	0.05	1.17	0.086
p-Xylene	C_8H_{10}	106.16	411.15	140.4	6.13	4.92	472.82	192.78	1.55	0.00207	0.04	1.18	0.078
Ethanol	C_2H_6O	46.07	351.55	59.2	4.60	4.15	404.28	178.26	1.67	0.00205	0.06	1.15	0.126
1-Butanol	$C_4H_{10}O$	74.122	107.89	103.6	5.54	4.63	438.15	185.58	1.61	0.00206	0.05	1.17	0.093
Acetone	C_3H_6O	58.08	329.68	74.0	4.95	4.33	379.13	172.63	1.73	0.00206	0.05	1.13	0.113
MEK	C_4H_8O	72.11	352.79	96.2	5.41	4.56	405.71	178.57	1.67	0.00206	0.05	1.15	0.098
n-Hexane	C_6H_{14}	86.18	342.15	140.6	6.14	4.92	393.47	175.86	1.69	0.00206	0.05	1.14	0.082
Octane	C_8H_{18}	114.23	399	185.0	6.72	5.22	458.85	189.91	1.57	0.00207	0.04	1.18	0.069

5.4.2.2 Mass Transfer Coefficient

Votruba et al. (1975) developed the Sherwood number (Sh) which is used to calculate the interphase mass transfer coefficient, k_g:

$$Sh = 0.705\left(Re\frac{D}{L_f}\right)^{0.43} Sc^{0.56} \quad , \qquad [5\text{-}44]$$

where Sc is the Schmidt number and Re is the Reynolds number, D is the characteristic length of fibrous media, and it was taken as the average diameter of fiberglass fibers of 9×10^{-5}(m). Considering Reynolds number is associated with the airflow rate, Sherwood number is a function of the airflow rate and characteristic length of TiO_2 particle. In addition, Sherwood number integrates the convective mass transfer coefficient in its definition, $Sh = k_g D/D_m$, then the convective mass transfer coefficient can be determined from the computed Sherwood number. The mass transfer coefficients of various compounds at the three airflow rates for TiO_2/FGFs are presented in Table 5-4.

Table 5-4 Mass transfer coefficients at different airflow rates for TiO_2/FGFs

Empirical estimation	Mass transfer coefficient, k_g (m/s)		
	0.26 m/s (50 cfm)	0.51 m/s (100 cfm)	0.76 m/s (150 cfm)
Toluene	0.47	0.62	0.74
p-Xylene	0.45	0.60	0.71
Ethanol	0.55	0.74	0.88
1-Butanol	0.48	0.65	0.77
Acetone	0.53	0.70	0.83
MEK	0.49	0.66	0.78
n-Hexane	0.46	0.61	0.72
Octane	0.42	0.57	0.67

5.4.3 Irradiance Parameters

Taking into account the fact that the irradiance distribution within the catalyst follows exponential decay, the extinction coefficient of catalyst was set to a typical value of 0.3 μm^{-1} (Hill, 1977; Changrani and Raupp, 2000).

In this study, the irradiance at the surface of the TiO_2 filter was always greater than 1-2 mW/cm^2. According to the empirical correlation between the reaction rate and the light intensity (Obee and Brown, 1995), the power exponent value of 0.5 was considered in the simulation.

The reflectivity of smooth aluminum surfaces is more than 90% for wavelengths from 0.9 to 12 μm. At wavelength below 200 nm, the reflectivity of smooth aluminum surfaces is about 70% (Totten and Mackenzie, 2003). Reflectivity is also affected by purity of aluminum. In this study, the 254 nm and 185 nm reflectivity of the aluminum reactor was taken as 85% and 70%, respectively.

5.4.4 Photocatalytic Reaction Rate

The photocatalytic reaction rate closely depends on the reactor configuration, the photocatalyst activity, RH, temperature, irradiance, as well as the challenge concentration since they significantly affect the PCO behavior. Considering the gas stream is diluted, KCs in Eq. (5-27) becomes <<1 and the reaction is of the apparent first order. Also, the inlet concentration of a VOC is an approximation to the concentration at the boundary layer of catalyst. Then Eq. (5-27) can be simplified as:

$$-r_i = \frac{\int_0^{L_f} (exp^{-\mu L_f x})^{\beta} dx}{L_f} I_f{}^{\beta} k_i K_i C_i \qquad [5\text{-}45]$$

For the assumed plug flow PCO reactor with a constant inlet concentration, photocatalytic reaction rate is experimentally determined by the difference between the inlet concentration and the outlet concentration with respect to the time to reach equilibrium. Figure 5-9 shows the relationships between inlet concentration and the reaction rate for all tested VOCs. Once the slope of the linear regression curve, the adsorption coefficient, and the inlet concentration are known, the reaction rate constant can be determined by Eq. (5-45). Since there were three inlet concentrations employed in this study, the average reaction rate constant was taken as the reaction rate constant for each chemical compound (Table 5-5). It should be noted the difference of k_i may not correctly reflect the ranking of photocatalytic activity among different VOCs. In fact, the value of $k_i \bullet K_i$ provides better indication of the synthetic effect of adsorption and photocatalytic oxidation, and more accurately specify the photocatalytic activity of different VOCs. Also, the value of $k_i \bullet K_i$ (2.616×10^{-4} s^{-1}) obtained in this study for toluene is close to 6.916×10^{-4} s^{-1} reported by Shiraishi and Ishimatsu (2009) and 0.8844×10^{-4} s^{-1} reported by Sleiman et al. (2009).

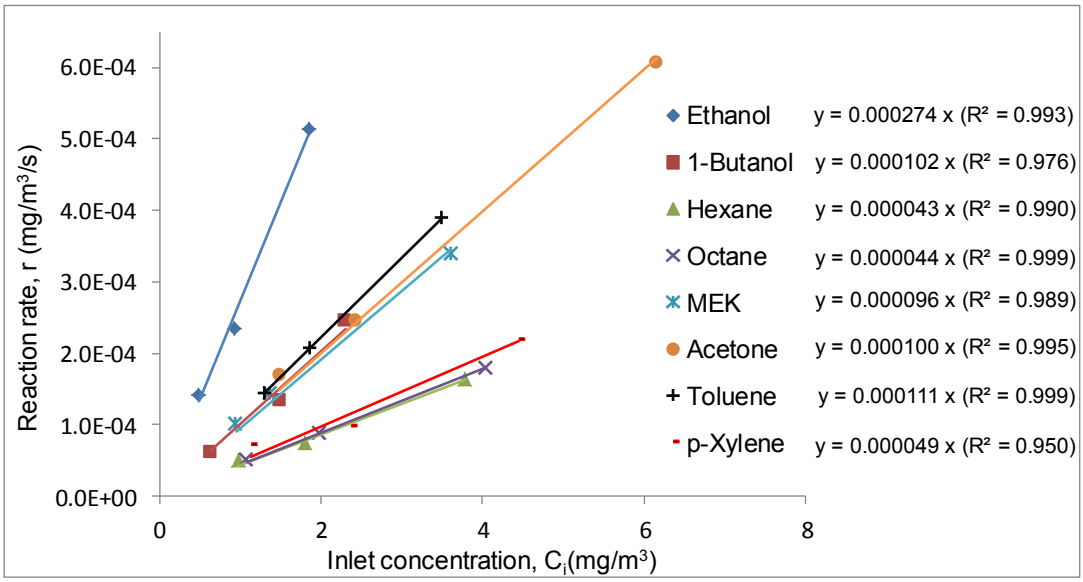

Figure 5-9 Estimation of kinetic parameters for PCO of various VOCs. (Experimental conditions: C_{in}= 0.25-2 ppm; air flow rate = 170 m^3/h; RH = 15.6%-44.7%; irradiance = 27-30 W/m^2)

Table 5-5 Kinetic parameters

VOC	RH	Adsorption coefficient K_i (m^3/mg)	PCO reaction rate constant k_i (mg/m^3/s)	$k_i \cdot K_i$ (s^{-1})
Ethanol	15.6%	1.04×10^{-4}	5.90±0.31	6.16×10^{-4}
1-Butanol	19.8%	4.38×10^{-4}	0.52±0.07	2.30×10^{-4}
n-Hexane	32.0%	1.20×10^{-6}	79.85±0.22	9.58×10^{-5}
Octane	43.0%	9.00×10^{-7}	109.31±0.30	9.84×10^{-5}
Acetone	43.2%	1.33×10^{-5}	16.86±0.63	2.25×10^{-4}
MEK	22.2%	1.24×10^{-4}	1.73±0.12	2.16×10^{-4}
Toluene	44.7%	2.41×10^{-6}	108.71±11.89	2.62×10^{-4}
p-Xylene	34.6%	8.92×10^{-6}	12.68±2.17	1.13×10^{-4}

5.4.5 Ozonation Parameters

The effect of the ozonation on removal of indoor air pollutants was examined by placing different numbers of VUV lamps in each duct of the four-parallel duct system. For each level of inlet concentration of various VOCs, the efficiency of ozonation was

explored by four levels of ozone concentrations and the corresponding ozonation rate constant was calculated by Eq. (5-34). Table 5-6 shows the summary of the average ozonation kinetic rate constant for different VOCs with various inlet concentrations. It should be noted that the rate reactions for acetone and MEK by O_3 were negligible. Hence, the ozonation effect on removal of acetone and MEK was insignificant and their ozonation rate constants were not discussed here.

Table 5-6 Ozonation kinetic parameter for the oxidation of VOCs

Inlet VOC concentration (ppm)	$k_{O3,i}$ (m^3/mg/s)$\times 10^{-2}$					
	ethanol	1-butanol	hexane	octane	toluene	p-xylene
0.25	3.48	4.15	4.75	4.20	2.91	4.34
0.5	2.38	3.66	3.10	3.02	1.95	3.29
1.0	1.58	2.94[(a)]	2.48	2.32	1.21	1.79

Note: (a) inlet concentration of 1-butanol was 0.8 ppm.

5.5 Model Implementation

To numerically solve the problem, the TiO_2 film is discretized into n elemental cells connected in series in the direction of the airflow (Figure 5-10). Since the fibrous diffusion inside the fibers is not considered in the modeling, only one fiber element is needed for each film node and the concentrations C_B and C_S are assumed to be uniform within a same cell. Considering each of the film cells as a mass transport component, the output concentration was solved by using the finite difference method with the aid of Matlab R2009B.

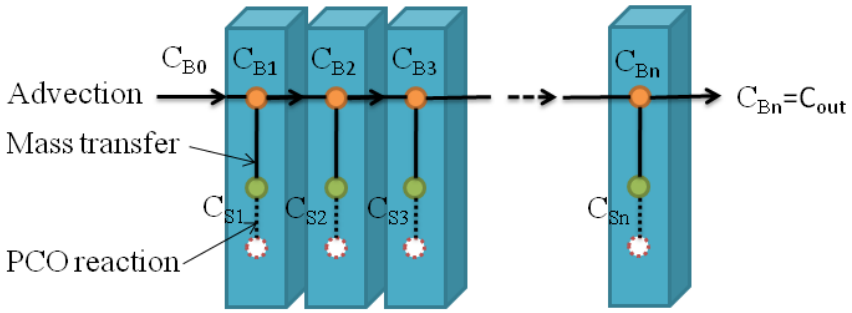

Figure 5-10 Discrete representation of TiO_2 filter

Figure 5-11 demonstrates the interrelationships between different influencing elements in the UV-PCO model. The inputs and outputs of the programming for the light scattering model and the UV-PCO model are described in Figure 5-12.

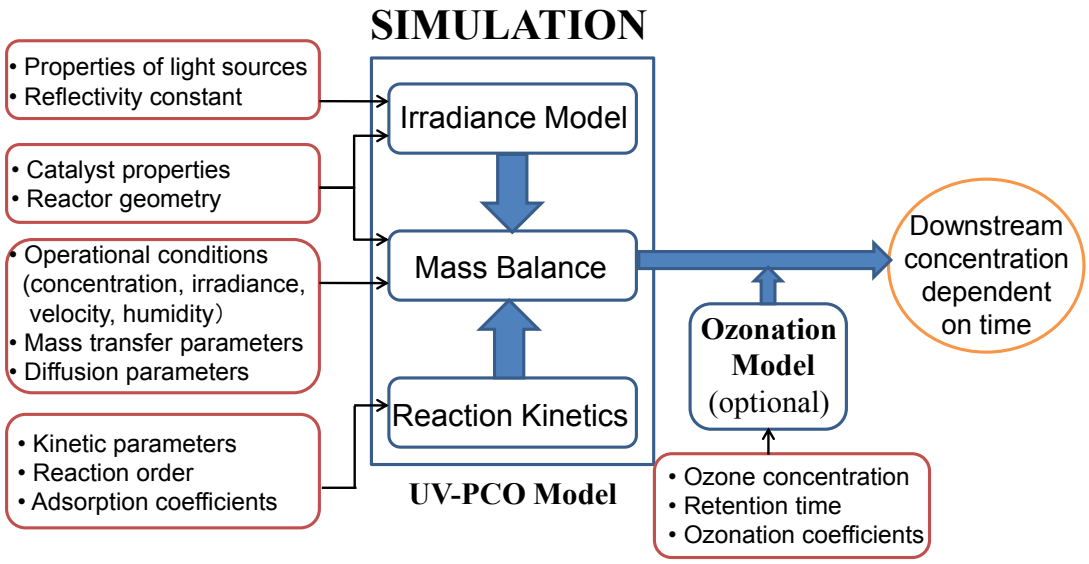

Figure 5-11 Structure of simulation program

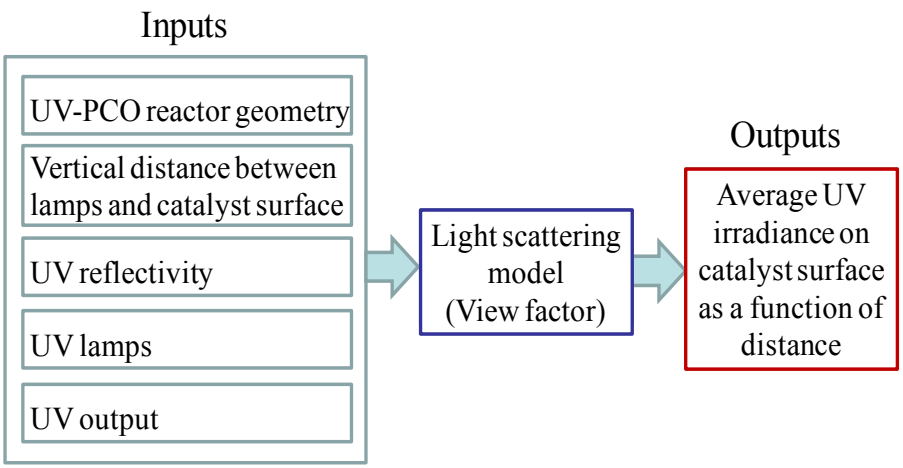

(a) Light scattering model

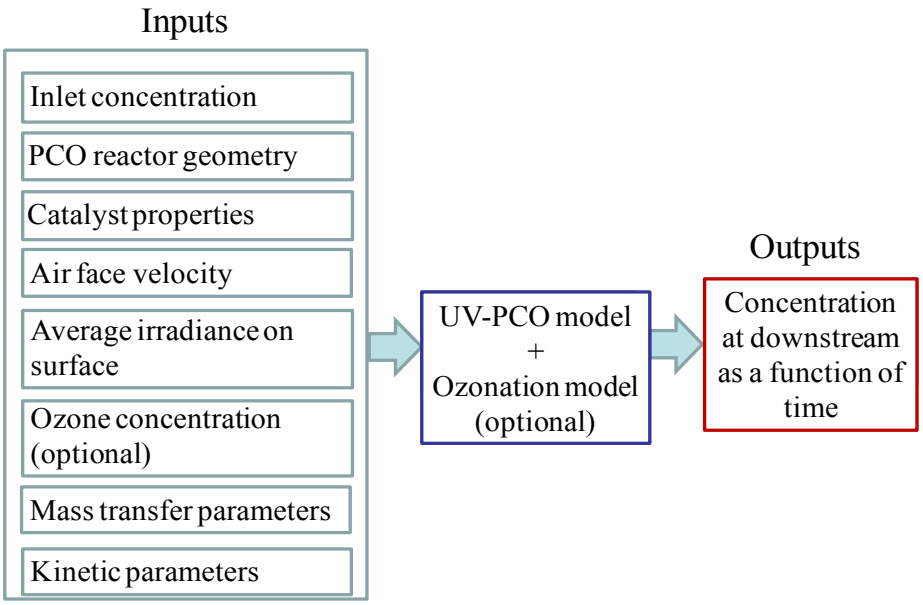

(b) UV-PCO model

Figure 5-12 Programming structure

5.6 Model Verification

5.6.1 Inter-model Comparison

To validate the PCO model prediction, simulation results are compared with the prediction made by an existing two-site kinetic model (Lewandowski and Ollis, 2003).

Two-site kinetic model is established on the basis of the presumed presence of two different types of adsorption sites, hydrophobic adsorption sites (type I) and hydrophilic adsorption sites (type II). For the reactant i, it is assumed to be only accessible to hydrophobic adsorption sites (type I). The site balance is given as follows:

$$\frac{d\theta_i}{dt} = k_{ads,i} P_i \theta_{S1} - k_{des,i} \theta_i - k_1 \theta_i \qquad [5\text{-}46]$$

Compared with the PCO model, the two-site kinetic model only considers the mass balance of a reactant at the fiber surface, but it gives a more detailed description (including the adsorption and the desorption) on mass transfer.

Figure 5-13 compares the PCO model simulation results with both experimental data and the two-site kinetic model simulation results for two cases. Two models provide reasonable fits for experimental data collected during the photocatalytic oxidation of toluene in a single-pass, powder layer PCO reactor under operational conditions of 20 mg/m^3 and 30 mg/m^3 of inlet concentration, 1000 mg/m^3 of water vapor concentration and 1×10^{-6} m^3/s (2 cfm) of airflow rate. In Lewandowski and Ollis (2003), a 100W blacklight was used as a UV energy provider, but no information about the irradiance was provided. So the value of irradiance is the only adjusted parameter in the simulation, and finally 16.5 mW/cm^2 is found to be a correct value to simulate the trend of the toluene concentration for both cases.

It is worthwhile to mention that in their experimental work, Lewandowski and Ollis (2003) did not turn on UV lights until the adsorption of toluene and water by the regenerated catalyst reached equilibrium. In other words, the first part of the experimental data reflects the adsorption process taking place, whereas the latter part shows the photochemical process being underway. This is the reason for the discrepancy between

experimental data and the PCO model predictions at the initial stage. After 60 minutes, however one can see that the exit concentration profile predicted by the PCO model for both cases seems to be more consistent with the experimental data than that predicted by the two-site kinetic model. The good agreement between the predictions from the proposed PCO model and previous experimental results indicates the PCO model can correctly capture the trend of efficiency as a function of time. Hence, the validated model can be applied to describe the behavior of a PCO for application in the in-duct UV-PCO air cleaners.

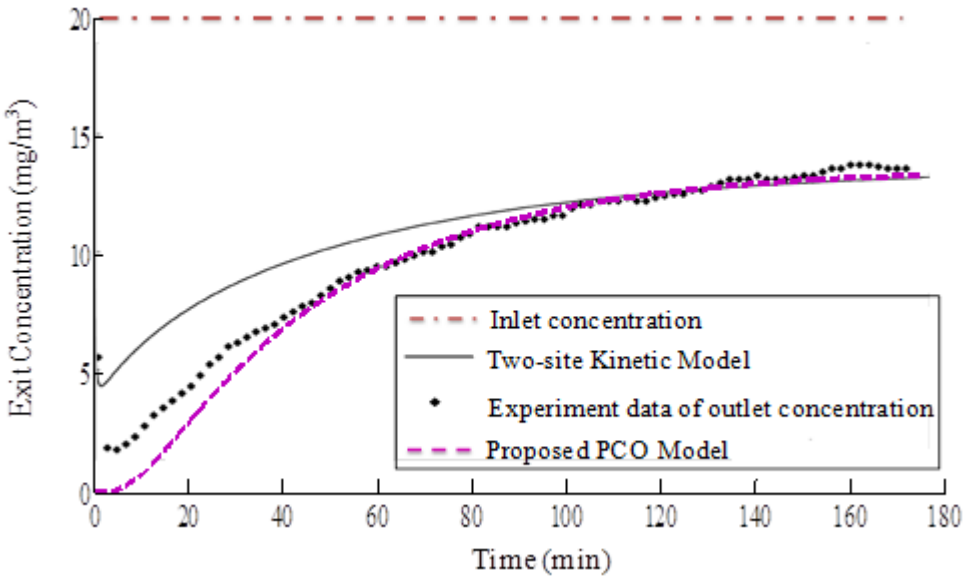

(a)

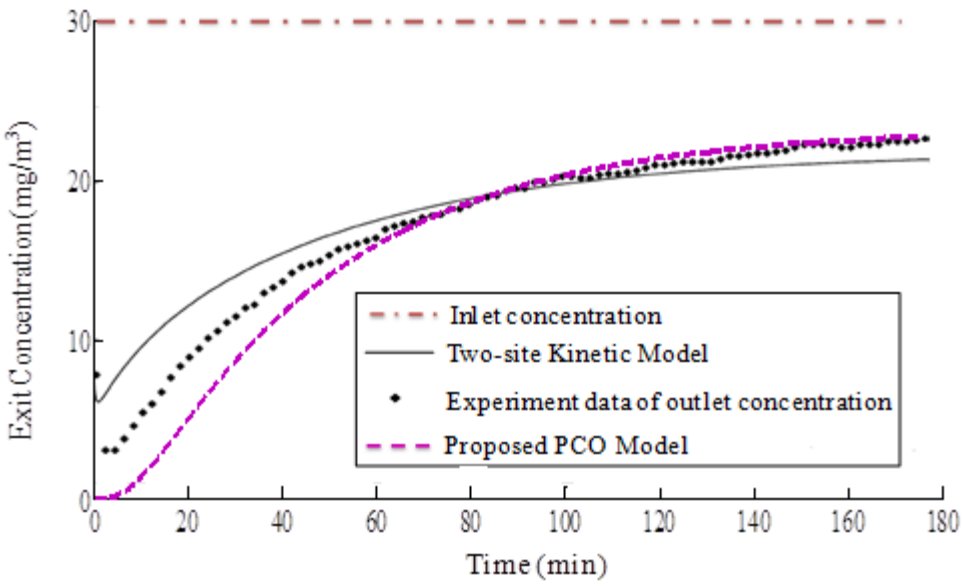

(b)

Figure 5-13 Comparison of model prediction with the prediction of two-site kinetic model (Lewandowski and Ollis, 2003) for toluene with inlet concentration of (a) 20mg/m^3 (b) 30mg/m^3. (Simulation conditions: C_{in}=20mg/m^3 and 30mg/m^3; C_{H2O}=1000mg/m^3; u=0.011m/s; I_f=16.5mW/cm^2)

5.6.2 Limiting Case Study

In order to further verify the model prediction, it is used to investigate the impact of limiting cases, which includes zero air velocity, zero reaction rate constant, zero adsorption coefficient, and zero mass transfer coefficient. These limiting cases are beyond the experimental possibility, but they still can be compared with theoretical analysis.

- Zero velocity (u). Airflow is mainly responsible for bringing the reactant into the filter bed. When the velocity is zero, the molecular diffusion is the only mechanism of mass transfer into the catalyst surface. Compared with flow fluid, molecular diffusion is much slower so that the VOCs molecules have more retention time on

the catalyst surface. Hence, the single-pass removal efficiency under molecular diffusion is higher than that with flow, as shown in Figure 5-14.

- Zero reaction rate constant (k) and/or zero absorption coefficient (K). In this case, the model is changed to account for the sorption dynamics of contaminants. Figure 5-14 shows that after the TiO_2 fibers adsorb pollutant molecules for some time, and then the fibers have no capacity to hold additional contaminant molecules, the removal efficiency curve will be close to zero due to the breakthrough.
- Zero mass transfer coefficient (k_g). Reagent species need to transport through the boundary layer surrounding the catalyst fibres before being absorbed and photochemical reaction takes place. So the mass transfer coefficient is an important parameter which determines the number of pollutant molecules reaching the PCO surface and being involved in the reaction. When the mass transfer coefficient is zero, there is no occurrence of external diffusion in the boundary layer, and thus no PCO reaction. Therefore, breakthrough happens after the contaminant flow passes through the bed depth, and the removal efficiency also soon drops to zero (Figure 5-14).

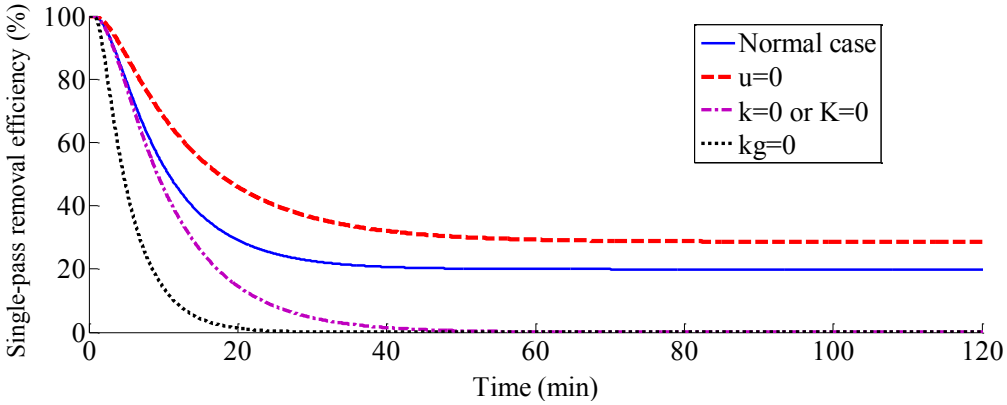

Figure 5-14 Single-pass efficiency-time profile modeled under different limiting cases for toluene (Simulation conditions: C_{in}=250 ppb; u=0 and 0.5 m/s; I_f=27.5 W/m^2; k_0=0 and 108.7 mg/m^3·s; K=0 and 2.087×10^{-3} m^3/mg; k_g=0 and 0.62 m/s)

The simulation results for aforementioned extreme cases are presented in Figure 5-14. It can be observed that the developed model is able to predict correctly the performance of the system for the extreme cases and the prediction follows the theory.

5.6.3 Comparison with Experimental Results

The light scattering model was validated by comparing the experimental results with the simulation results. Figure 5-15 shows the irradiance profiles with an increase of the measurement distance for the wavelength at 254 nm and 185 nm, respectively. For two different scenarios, two lamps and three lamps, the model predictions were in good agreement with the experimental data. Also for the simulation cases, all correlation coefficients were greater than 0.96, which indicates that the irradiance model can accurately predict the irradiance at the catalyst surface.

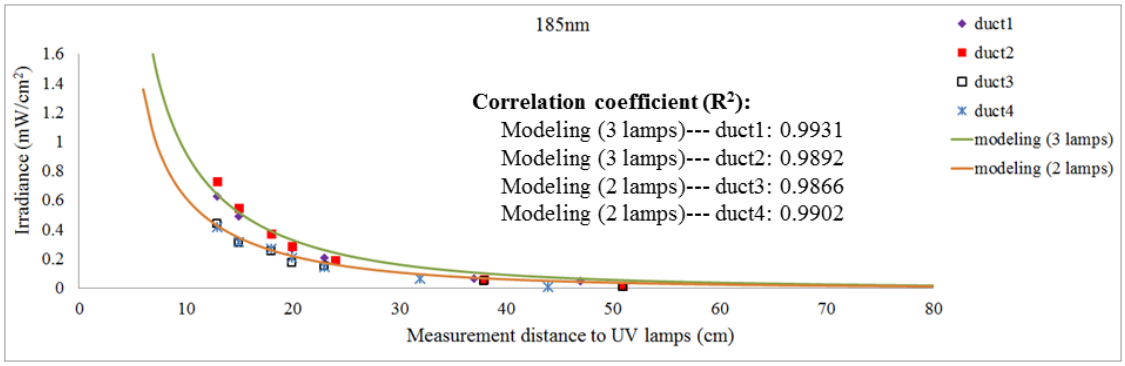

(a) Irradiance vs. distance for 185 nm

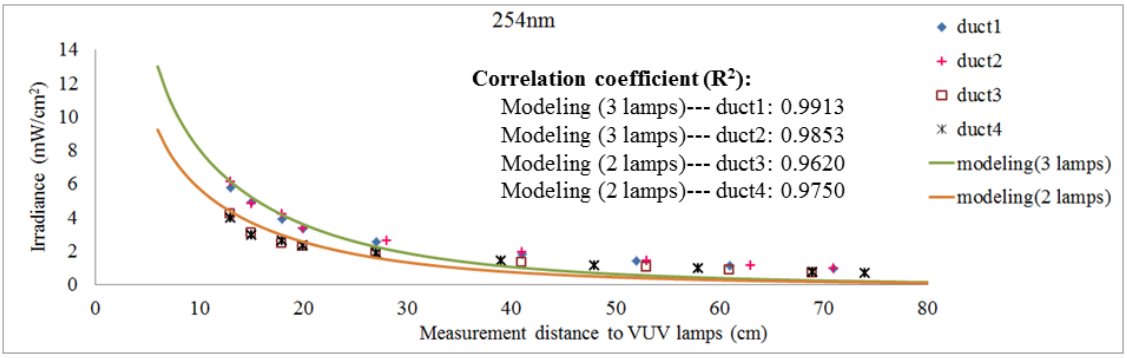

(b) Irradiance vs. distance for 254 nm

Figure 5-15 Model predictions vs. experimental results for relationship between irradiance and distance

Figure 5-16 (a) shows the single-pass removal efficiency predicted by the UV-PCO model versus the single-pass removal efficiency obtained from the experiments of TiO_2/FGFs under the illumination of UVC. Theoretically, the predictions from a perfect model should fall on the diagonal which has a slope of unity. The linear regression formula shows the slope of 0.939, which is very close to unity, with an R^2 of 0.952. This result indicates a satisfactory agreement between the model predictions and experimental results, and thus the validity of the UV-PCO model is verified.

For the ozone-assisted UV-PCO technology, Figure 5-16 (b) presents the efficiency of model predictions versus experimental results with a regression slope of 1.016 and a R^2 of 0.863. This outcome demonstrates the combination of the UV-PCO model and ozonation model is capable of correctly predicting the experimental results with high confidence.

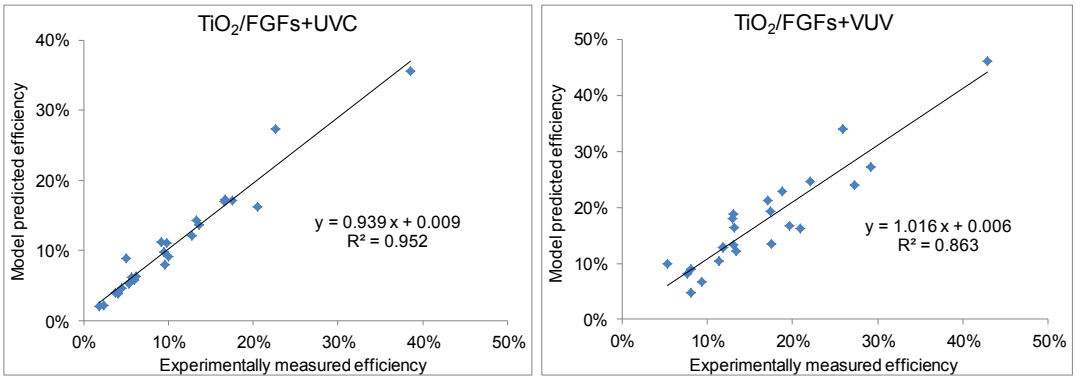

(a) (b)

Figure 5-16 Overall model predictions vs. experimental results for (a) TiO_2/FGFs + UVC, and (b) TiO_2/FGFs + VUV

A series of experiments were carried out to further assess the validity of the UV-PCO model or combination of the UV-PCO model and the ozonation model under various experimental conditions. The kinetic parameters, which were examined by both experiments and models, included inlet concentration, RH, airflow rate and light intensity. Figure 5-17 shows the results of single-pass efficiency as a function of time for various VOCs with an inlet concentration varying from 250 ppb to 2 ppm. According to Eq. (5-45), it is apparent that the PCO reaction rate, r, increases with the inlet concentration, resulting in a short time to reach equilibrium. While, the conversion rate decreases with the inlet concentration due to the fixed number of active sites on the surface of air filters. The model predictions correlate well with the experimental results.

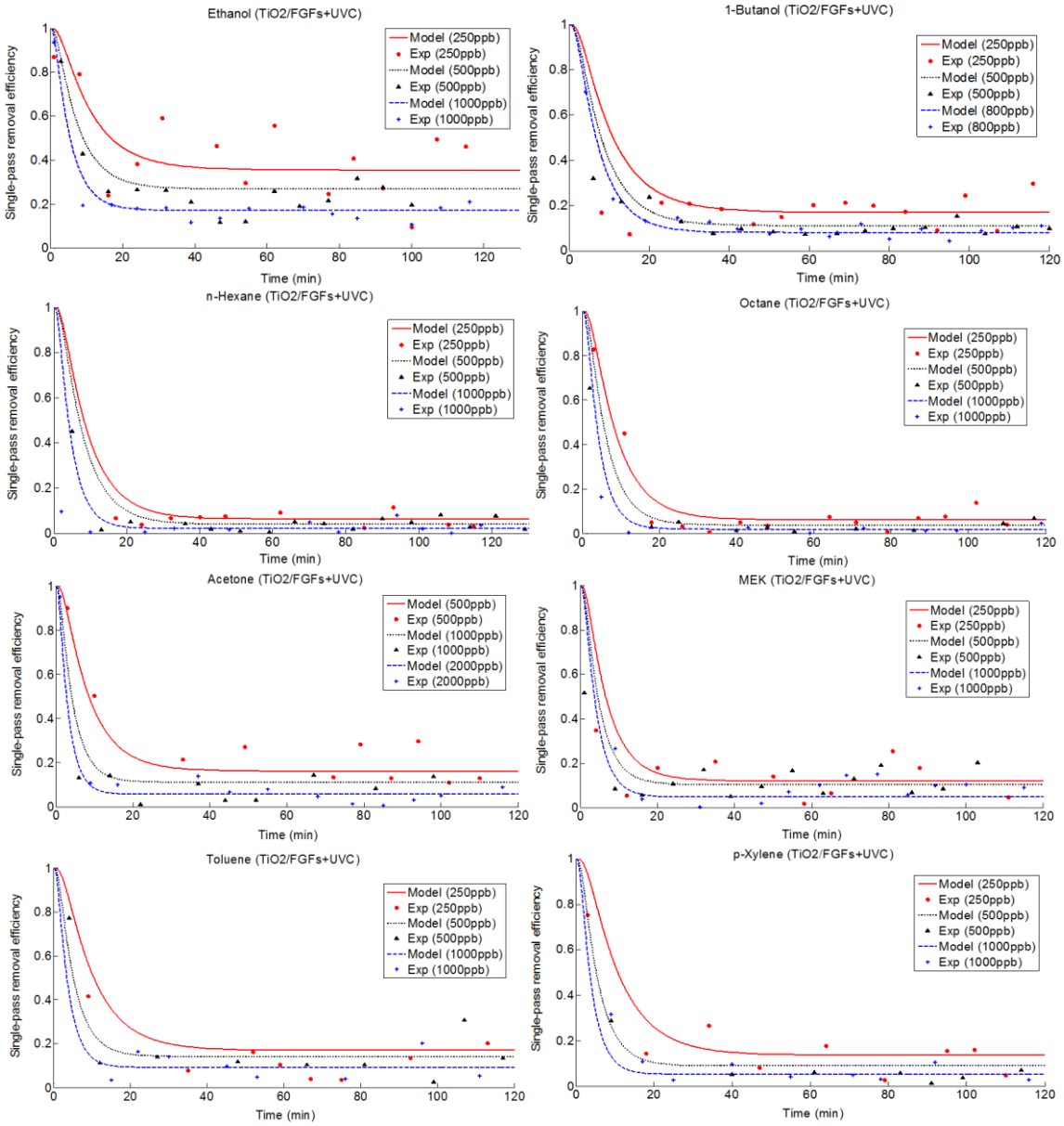

Figure 5-17 Comparison between model predictions (lines) and experimental results (symbols). Effect of initial concentration on UV-PCO of eight VOCs (C_{in}=250-2000 ppb, RH=15%-45%, flow rate=170 m^3/h, irradiance=27-30 W/m^2).

The results obtained at different RH are shown in Figure 5-18. Figures 5-18 (a) and 5-18 (b) show the model prediction and experimental results for PCO of ethanol with and without ozone. The model predictions satisfactorily fitted the experimental results obtained by varying humidity levels from 10% (2300 ppm) to 60% (16000 ppm). For toluene and acetone, there is good agreement between the predictions of the UV-PCO

model and the integrated model with the experimental results at different humidity levels. The simulation results further confirm the previous conclusion that the lowest relative humidity is the best condition for the PCO operation at indoor air environment (Zhong et al., 2010).

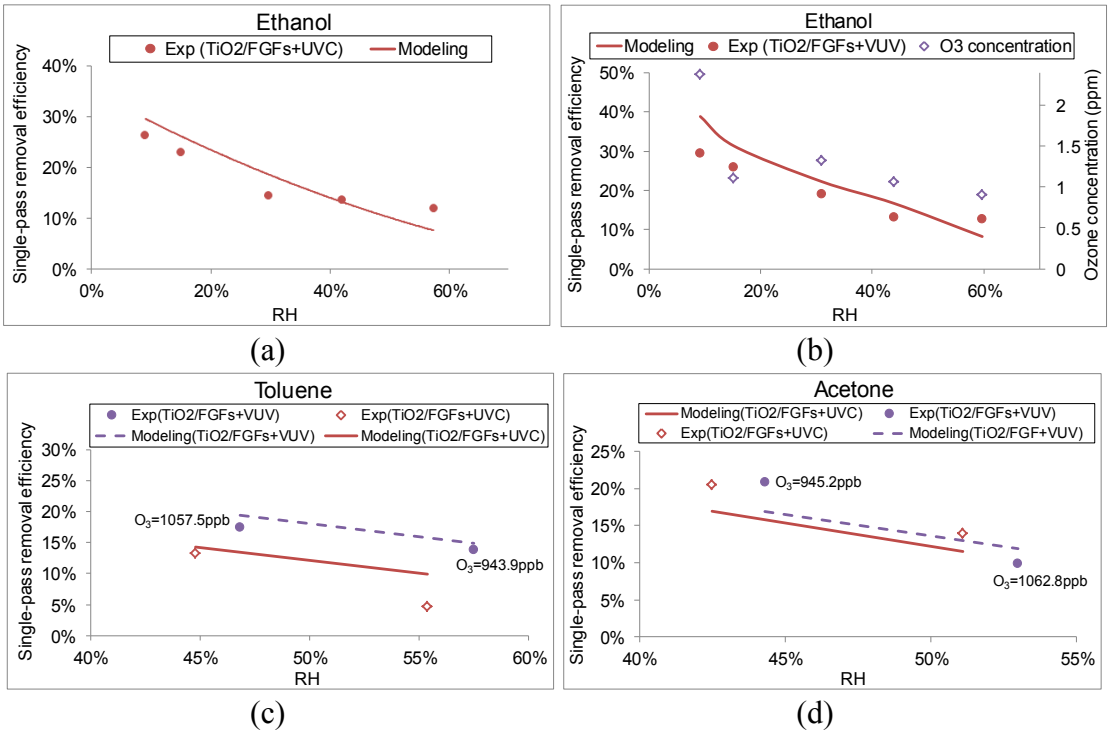

Figure 5-18 Comparison between model predictions (lines) and experimental results (symbols). Effect of RH on UV-PCO of (a) ethanol (UVC) (b) ethanol (VUV) (c) toluene, and (d) acetone (C_{in}=500 ppb, RH=10%-60%, flow rate=170 m^3/h, irradiance=24-36 W/m^2).

Figure 5-19 shows the single-pass removal efficiency of ethanol, toluene and hexane predicted by the UV-PCO model and the integrated model and the corresponding experimental data as a function of airflow rate. It clearly shows the model predictions and experimental results are in good agreement, which once again indicates the validity of the proposed models. The similar trends indicate that decreasing the airflow rate increases the residence time and thus enhances the surface PCO reaction.

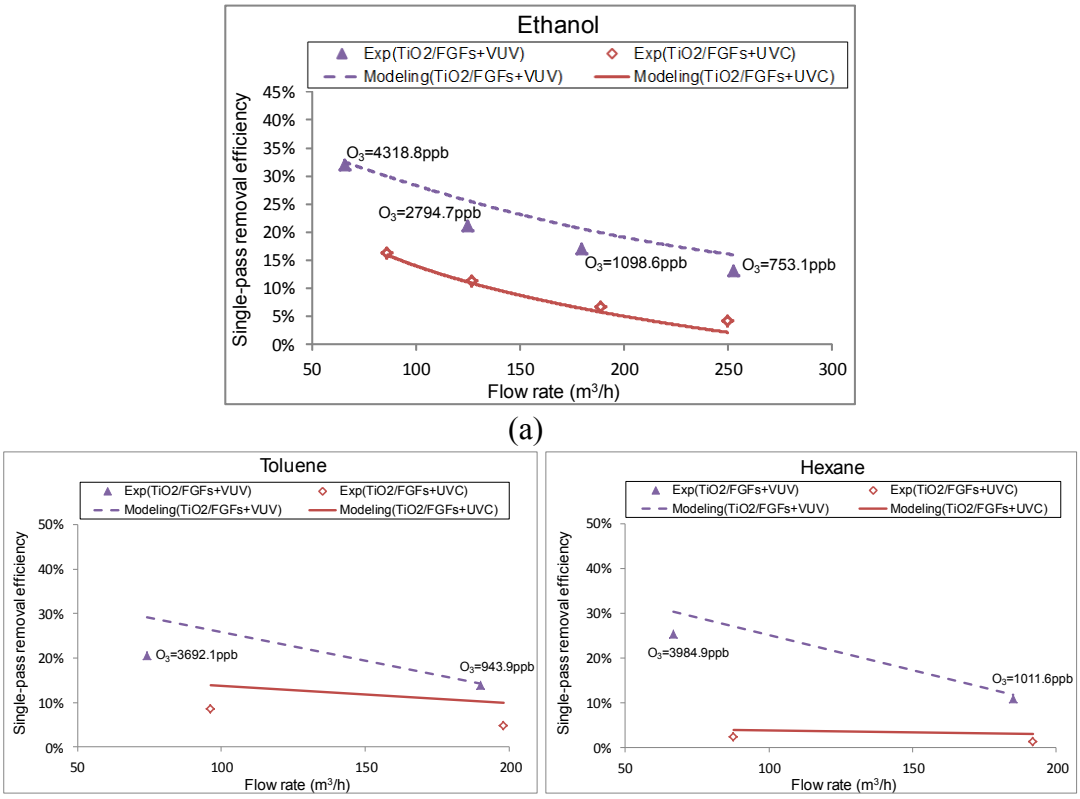

Figure 5-19 Comparison between model predictions (lines) and experimental results (symbols). Effect of air flow rate on UV-PCO of (a) ethanol (b) toluene and (c) hexane (C_{in}=500 ppb, flow rate=41-255 m^3/h, RH=40%-60%, irradiance=24-39 W/m^2).

As depicted in Figure 5-20, the conversion rates of ethanol, acetone, toluene, and hexane for both experimental results and model predictions increased as the light irradiance enhanced from 16-43 W/m^2. Good agreements between the experimental results and the model calculations further indicate that the UV-PCO model is adequate to predict irradiance effect on the UV-PCO performance. According to the predicted correlations between the reaction rate and the light intensity, for selected challenge gases the power exponent values are all close to 0.5, thus justifying the use of 0.5 as the kinetic order value in this study. It also agrees with the conclusions made by Obee and Brown (1995) that recombination of the partial electron-hole pairs leads to not all pairs

effectively participate in the chemical reactions.

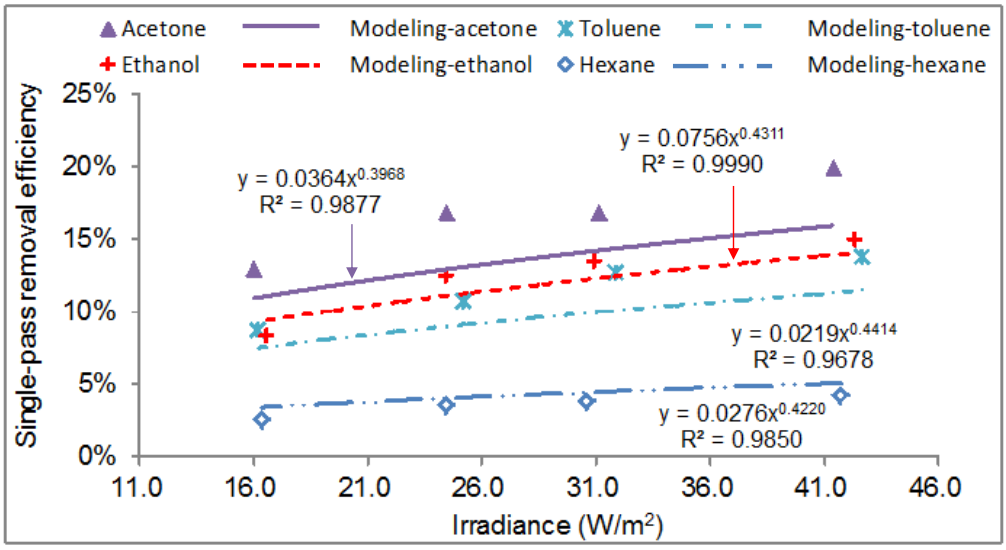

Figure 5-20 Comparison between model predictions (lines) and experimental results (symbols) for acetone, ethanol, toluene, and hexane (C_{in}=500 ppb, flow rate= 170 m^3/h, RH=55%-62%, irradiance= 16-43 W/m^2).

5.6.4 Parameter sensitivity analysis

The parameter sensitivity analysis has been performed in order to examine how the output can be apportioned to the different sources of input. In our study, the input can be characterized by the kinetic parameters, which includes the PCO reaction rate constant, adsorption coefficient, and ozonation kinetic rate constant. Each input parameter is increased individually while all the other parameters are kept at the same level in order to find out their effects to the output variation. Figure 5-21 presents the sensitivity analysis results using 250 ppb ethanol as an example. When the PCO reaction rate constant was doubled (an increase of 100%), the single-pass removal efficiency was enhanced around 20%, which exhibits the biggest variation compared with other simulation results. It indicates that the single-pass removal efficiency is more sensitive to the PCO reaction rate constant than the other parameters. As a result, the optimization of the PCO reaction

rate is a promising way to improve the performance of PCO technology.

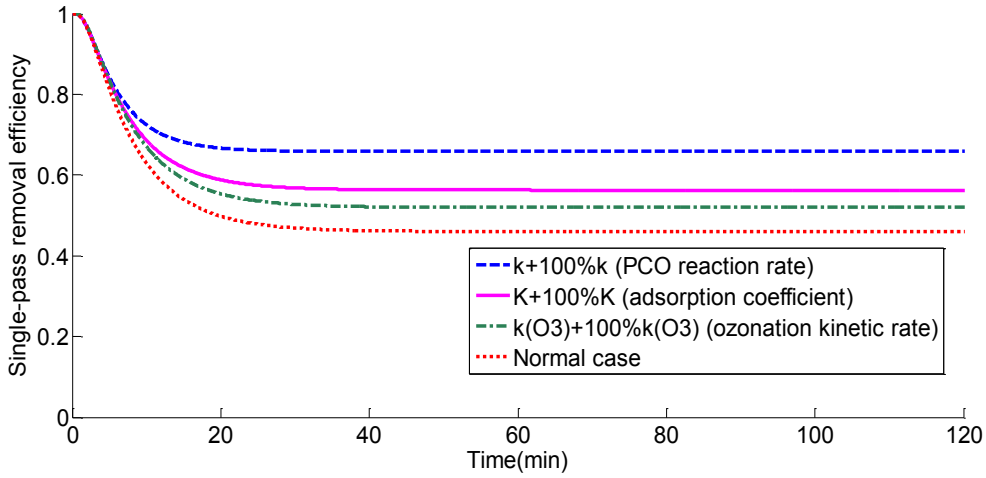

Figure 5-21 Parameter sensitivity analysis (Simulation conditions: Cin=250 ppb, irradiance=29.5 W/m^2, flow rate=170 m^3/h, RH=15%, ozone concentration=1181 ppb)

5.7 Application to Other Air Filter

To verify the applicability of the proposed model, more experiments were conducted with a carbon cloth fibers (CCFs) filter coated with TiO_2 using the same experimental set-up. Figure 5-22 shows three-dimensional surfaces predicted by OriginPro 8 software based on its SEM images. The porosity of 0.45 was obtained using the same method described in section 5.4.1. The summarized physical properties of the TiO_2/CCFs air filter are shown in Table 5-7.

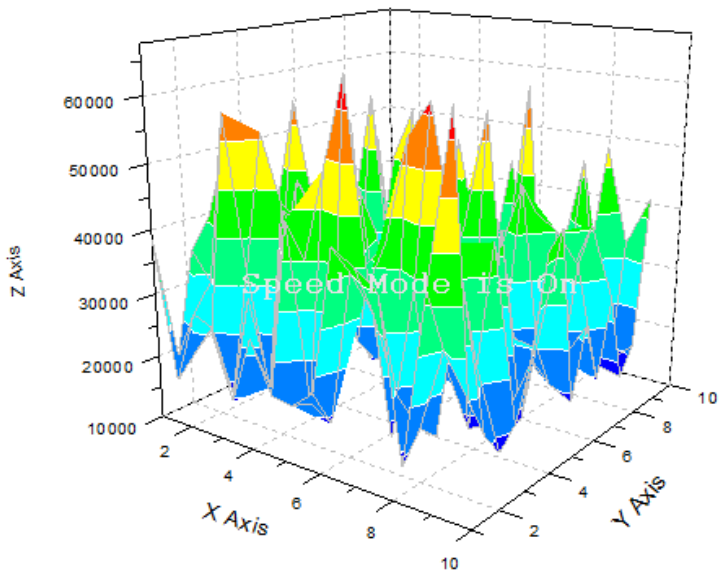

Figure 5-22 3D surface of TiO_2/CCFs predicted by OriginPro 8 software (x, y and z are the dimensions of the projected surface).

Table 5-7 Physical properties of TiO_2/CCFs air filters

Porosity, ε	Tortuosity, τ	Diameter, μm	BET, m^2/g	TiO_2 layer thickness, L_f (μm)
0.45	3	150	887.7	5

Ethanol and hexane, as a typical polar and a non-polar chemical compound, respectively, were employed to evaluate the performance of the PCO air cleaners supported by CCFs. Table 5-8 shows modeling parameters for ethanol and hexane. Since some parameters, such as the diffusion coefficient, $D_{m,i}$, and the ozonation rate constant, $k_{O3,i}$, are related to the gas properties rather than the supporting material, the same values as described earlier (Table 5-3 and Table 5-6) were used. The mass transfer coefficient, $k_{g,i}$, is a function of the characteristic length of fibers and porosity, and then the value of 0.80 m/s and 0.67 m/s was calculated for ethanol and hexane, respectively, when using CCFs as a substrate. The airflow rate was taken as 170 m^3/h. The adsorption coefficient, K_i, as a function of RH, was determined by the Langmuir isotherm method (see Section

4.5). The PCO reaction rate constant, k_i, was estimated by fitting the UV-PCO model with experimental results in the absence of ozonation effect. Since the irradiance applied in the tests was always higher than 10 W/m^2, the reaction order with respect to irradiance β was taken as 0.5.

Table 5-8 Modeling parameters for ethanol and hexane

Parameter	Ethanol	Hexane
$D_{m,i}$ (m^2/s)	12.6×10^{-6}	8.2×10^{-6}
$k_{g,i}$ (m/s) @ 170 m^3/h	0.80	0.67
K_i (m^3/g)	$\ln K_i$=-3.55RH-0.77	$\ln K_i$=-5.08RH+0.47
k_i (mg/m^3/s)	3.60	0.17
$k_{O3,i}$ (m^3/mg/s)$\times10^{-2}$	3.48 (0.25 ppm) 2.38 (0.5 ppm) 1.58 (1.0 ppm)	4.75 (0.25 ppm) 3.10 (0.5 ppm) 2.48 (1.0 ppm)
β	0.5	0.5

Figure 5-23 shows the comparison between model predictions and experimental results for ethanol and hexane removal with the TiO_2/CCFs filters illuminated with UVC or VUV setting up in a one bank configuration. The model predictions agree well with the experimental results, implying the values of kinetic parameters are reasonable, and the proposed model can be applied to describe the behavior of UV-PCO employing with various PCO air filters.

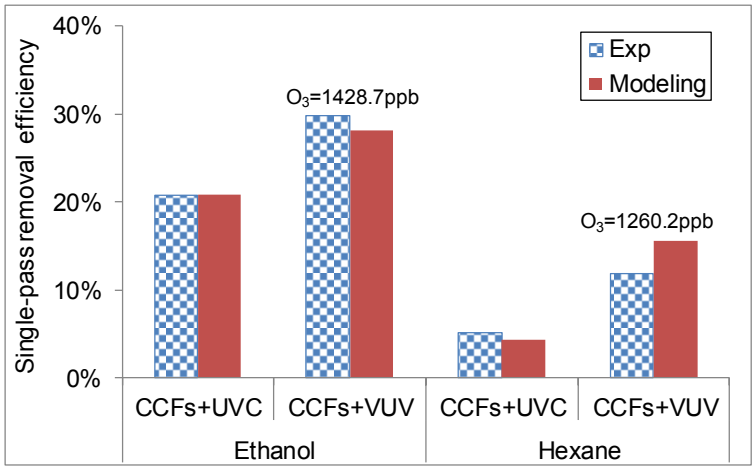

Figure 5-23 Comparison between model predictions versus experimental results for ethanol and hexane at two scenarios: TiO_2/CCFs+UVC and TiO_2/CCFs+VUV (C_{in}=500 ppb, flow rate=170 m^3/h, RH=40%-50%, irradiance=23-26 W/m^2).

To further validate the model, modeling results were compared with experimental data for ethanol and hexane as an individual pollutant under different experimental conditions (C_{in}=250, 500, 1000 ppb, flow rate=170 m^3/h, RH=15%-50%, irradiance= 23-36 W/m^2). Figure 5-24 indicates the UV-PCO model and the integrated model can predict the experimental efficiency with high confidence (slope=0.9528, R^2=0.9301). The good agreement of model-experiment results further demonstrates the broad applicability of the proposed models.

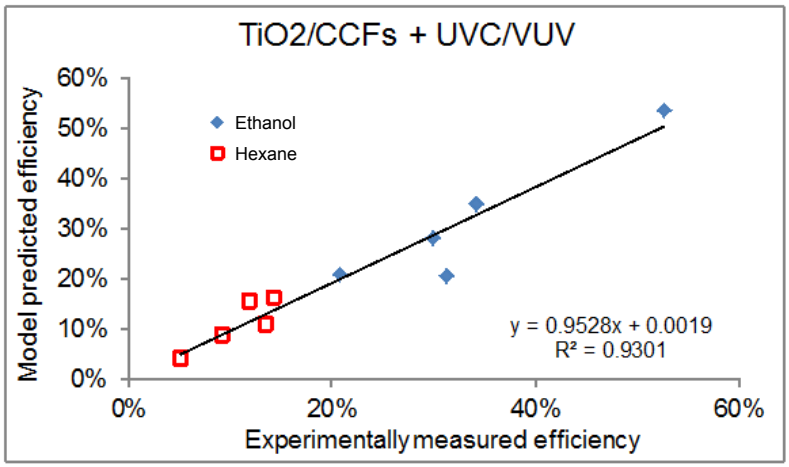

Figure 5-24 Overall model predictions vs. experimental results for TiO_2/CCFs illuminated by UVC or VUV with a challenge gas of ethanol or hexane (C_{in}=250, 500, 1000 ppb, flow rate= 170 m^3/h, RH=15%-50%, irradiance= 23-36 W/m^2)

5.8 Identify the Rate Limiting Process/Parameter

The simulation program is then used to study the PCO behavior under different operational conditions, as well as to account for the PCO performance resulting from the influencing design parameters. Utilization of the proposed UV-PCO model as a design tool, the dominating process/parameter to mainly control photocatalytic degradation efficiency could be obtained. The following simulation analysis was conducted using ethanol as an example.

Airflow Rate

Flow rate impacts the reaction rate in two ways: it influences heterogeneous mass transfer and kinetic reaction. Under a steady state condition, the adsorbed concentration at the solid surface is independent of time and thus, the mass transfer rate equals to the surface PCO reaction rate. The following equation can be established if competitions of by-products are not considered (Zhong and Haghighat, 2011):

$$k_g a(C_B - C_S) = \frac{\int_0^{L_f} \left(e^{-\mu L_f x}\right)^{\beta} dx}{L_f} (I_f)^{\beta} \frac{kKC_S}{1+KC_S} \quad [5\text{-}47]$$

where k_g is the inter-phase mass transfer coefficient (m/s), a is geometric surface area per unit reactor volume (m^{-1}), C_B is the concentration in the bulk fluid (mg/m^3), Cs is the concentration in the sorbed-phase (mg/m^3), L_f is the TiO_2 layer thickness (μm), μ is the UV irradiance extinction coefficient, β is the reaction order with respect to the UV light applied, k is the kinetic rate coefficient (s^{-1}), and K is the Langmuir's absorption parameter (m^3/mg).

$$\text{By setting } A = \frac{\int_0^{L_f} \left(e^{-\mu L_f x}\right)^{\beta} dx}{L_f} (I_f)^{\beta} \quad [5\text{-}48]$$

Considering the gas stream is much diluted, KCs in Eq. (5-47) becomes <<1 and the reaction is of the apparent first order. Then Eq. (5-47) changes to:

$$k_g a(C_B - C_S) = A \frac{kKC_S}{1+KC_S} \approx AkKC_S \quad [5\text{-}49]$$

Through transformation, Eq. (5-49) may be written

$$C_B = \left(\frac{AkK}{k_g a} + 1\right) C_S \quad [5\text{-}50]$$

If AkK is much smaller than $k_g a$, C_B will be similar to C_S, which indicates the surface PCO reaction is the controlling step. If AkK is far larger than $k_g a$, C_B will also be far larger than C_S, which indicates that the heterogeneous convective mass transfer limits the PCO process. Here, using toluene as an example and applying TiO_2/FGFs filters, the value of AkK is compared with that of $k_g a$. For the experimental conditions of airflow rate of 100 cfm, RH of 44.7% and irradiance of 30 W/m^2, kK and k_g is calculated to be 2.616×10^{-4} s^{-1} and 0.62 m/s, respectively, according to Table 5-5 and Table 5-4. Then the value of AkK is 1.18×10^{-4} s^{-1} based on the testing conditions, while the value of $k_g a$ is

2.48 s^{-1} which is much higher than AkK. Therefore, the result strongly supports the conclusion that the surface PCO reaction is the controlling step in this system.

Figure 5-25 shows the single-pass efficiency decays as a function of time. It also shows that as the airflow rate increases, the efficiency drops. In other words, as the airflow rate increases, the exposure time to PCO is so short that the decomposition of the pollutants is greatly compromised. More precisely, it means that the PCO reaction time is longer than the residence time and that the pollutants cannot fully participate in the PCO reaction. Therefore, the lower the airflow rate, the higher the single-pass efficiency. In addition, the method of decreasing the airflow rate to increase efficiency still shows its limitation: there is a negligible increase of efficiency when the velocity is less than 0.1 m/s. This observation indicates the physical mass transfer is not the rate-limiting process in our system. To be more specific, the photo-chemical process taking place on the limited active sites at the catalyst surface could be the dominating process in this system.

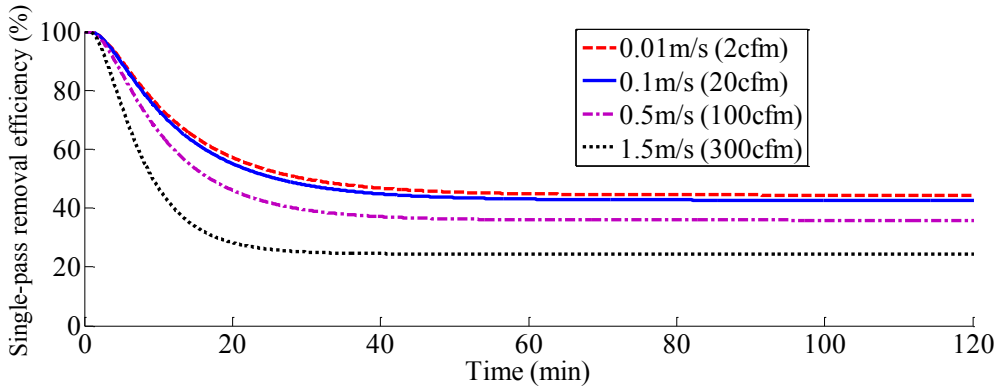

Figure 5-25 Effect of airflow rate (Simulation conditions: C_{in}=250 ppb; I_f=29.5 W/m^2; u=0.01, 0.1, 0.5, 1.5 m/s; RH=15%)

Inlet Concentration

Figure 5-26 shows the simulated result of single-pass efficiency as a function of time

for various inlet concentrations of ethanol; this shows that as the inlet concentration decreases the steady-state efficiency increases and the time to reach equilibrium is shorter. Theoretically, the single-pass efficiency can reach unity within the first few minutes. Then, it rapidly drops down as time elapses since the active sites on the catalyst surface are gradually blocked by reactants and/or intermediates. And the simulating results further demonstrate the fixed active sites, to some extent, limit photo-chemical reactions, especially when the challenge concentration is high. Hence, the single-pass removal efficiency increased from 20% to 60% when the inlet concentration of ethanol reduced from 1000 ppb to 10 ppb. It should be noted that in this study the change of the reaction rate constant due to gradually deactivated catalyst was not considered, which will be discussed later.

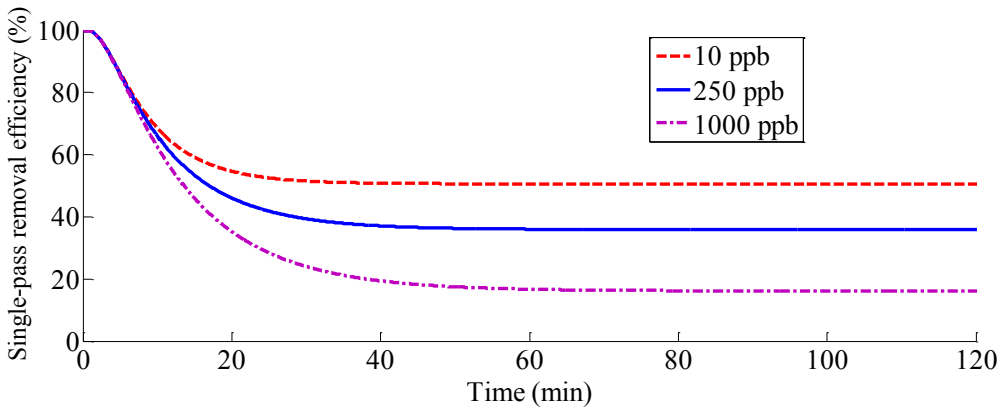

Figure 5-26 Effect of inlet concentration (Simulation conditions: C_{in}=10, 250, 1000 ppb; I_f=29.5 W/m^2; u=0.5m/s; RH=15%)

Light Intensity

UV irradiance has a pronounce impact on the performance UV-PCO since it determines the number of electron-hole pairs reacting with adsorbed water to form highly reactive hydroxyl radicals. Figure 5-27 shows the impacts of four levels of UV irradiance

on the PCO efficiency. This figure demonstrates that increasing the irradiance increases single-pass efficiency, and to be more specific, that the removal efficiency is nonlinear with UV irradiance. At low light intensity, electron-hole pairs effectively participate in the photochemical reactions, whereas recombination of the electron-hole pairs inhibits the rate of electron transfer at the high light intensity. Thus, not much hydroxyl groups expected are promoted by high irradiance. Hence, the single-pass removal efficiency depends nonlinearly on the light intensity.

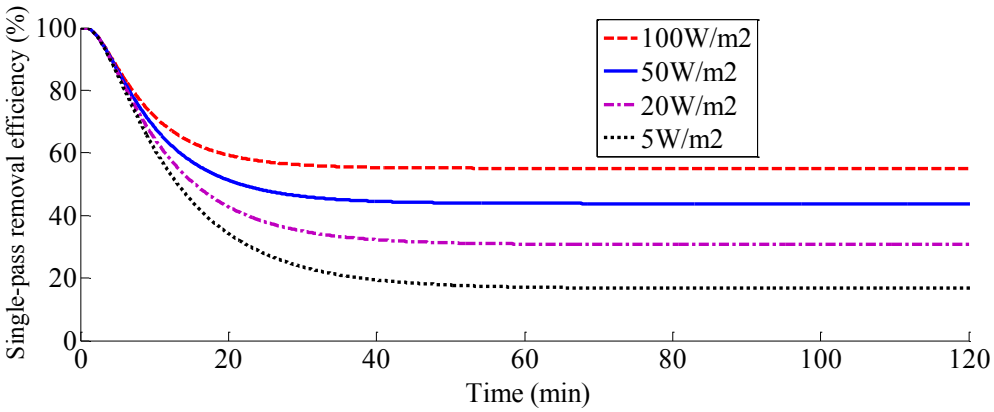

Figure 5-27 Effect of light intensity (Simulation conditions: C_{in}=250 ppb; I_f=5, 20, 50, 100 W/m^2; u=0.5 m/s; RH=15%)

Relative Humidity

Humidity has a dual role on the performance of the UV-PCO system: on one hand it supplies high-activity hydroxyl radicals, and on the other hand it competes with contaminants adsorbed on the catalyst surface. The optimal level of humidity needed in the PCO air cleaners is determined by contaminant concentrations. Figure 5-28 shows that decreasing the relative humidity leads to the increase of the single-pass efficiency, which indicates that the limiting factor is the adsorptive competition between moistures and pollutants under the case of photocatalytic oxidation of low concentration pollutants.

A decrease of RH before polluted gases entering in the UV-PCO units is an option for the optimal design in the application of the mechanically ventilated buildings.

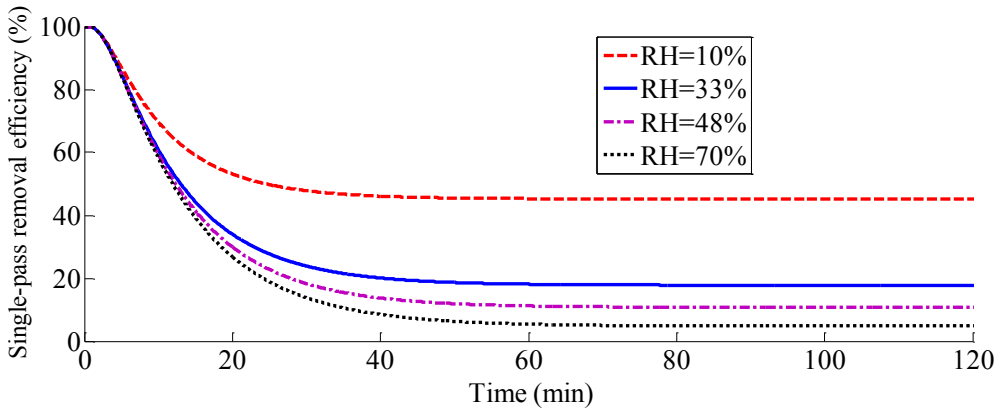

Figure 5-28 Effect of relative humidity (Simulation conditions: C_{in}=250 ppb; I_f=29.5 W/m^2; u=0.5 m/s; RH=10%, 33%, 48%, and 70%)

Catalyst Activities

Catalyst deactivation is a common phenomenon reported in previous work (d'Hennezel et al., 1998; Alberici and Jardim, 1997; Ameen and Raupp, 1999). The effect of assumed reaction rate constants on the efficiency of PCO was simulated to study the catalyst with different levels of deactivation. Figure 5-29 shows that single-pass efficiency is lower when the TiO_2 catalyst has a lower activity. The efficiency curves in the first 10 minutes have nearly identical slopes because the PCO process at initial stage is mainly controlled by advection and mass transfer, which bring reactants into the catalyst bed. After a certain amount of reactants accumulation at the surface of the TiO_2 fibers, the PCO reaction is the limiting process which controls all other PCO processes. Therefore, after the PCO air cleaners work for a certain period of time and reach equilibrium, the single-pass efficiency curve is closer to zero as the reaction rate constant becomes smaller. It should be mentioned that the kinetic rate coefficient, which is

assumed to be constant in this simulation, changes with time.

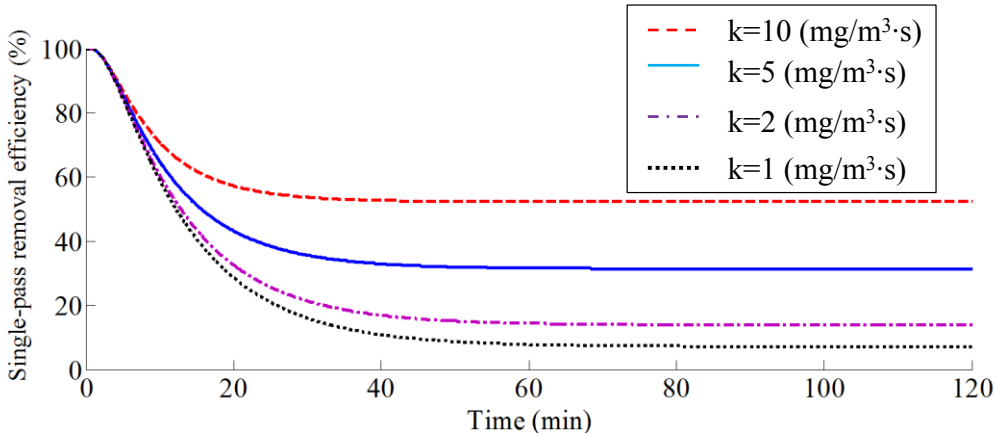

Figure 5-29 Effect of catalyst activities (Simulation conditions: C_{in}=250 ppb; I_f=29.5 W/m^2; u=0.5 m/s; RH=15%; k_0=1, 2, 5, 10 mg/m^3·s)

In summary, simulation results show the photochemical reaction, rather than the physical interactions, is the rate-limiting process in this system. And the photochemical reaction is greatly controlled by fixed active sites provided by the employed catalyst. In this case, the removal efficiency can be enhanced by increasing of irradiance, decreasing of RH, as well as improving the catalyst activity. Optimization of the catalyst configuration and/or development of a new supporting substrate with a large surface area are the possible directions of the optimal design in the UV-PCO reactor part.

5.9 Major Findings

(1) This section addresses a series of physico-chemical processes and the basic reaction mechanism involved in the heterogeneous PCO for the indoor air purification. In order to accelerate the widespread application of UV-PCO technology in HVAC systems, a reliable two-phase based time-dependent UV-PCO model was developed to describe the PCO behavior for eight VOCs removal. This model incorporated three sub-models: a

light scattering model, a reaction kinetic model and mass balance. All the influencing factors were taken into account in the development of the model. They included properties of light sources and catalyst, reactor geometry, mass transfer parameters, kinetic parameters, and operational conditions. All the inputs were obtained either experimentally or by using the existing empirical equations.

(2) In addition, for the case of ozone-assisted UV-PCO introduced by the VUV lamps, an ozonation model was proposed to describe the VOCs removal in the reaction with ozone followed by the UV-PCO model. The experimental results of UV-PCO of various VOCs for the TiO_2/FGFs air filters provided the required data for the validation of the UV-PCO model and the integrated model (VUV) under a wide range of experimental conditions. Moreover, the good agreement between the predictions made by the proposed models and the experimental results for the TiO_2/CCFs air filters further indicated the broad applicability of the proposed models.

(3) The validated model was used to carry out parametric studies to identify the influencing parameters. This exercise further verifies the validity of the model. The current model is therefore suitable for assessing the behavior of an in-duct UV-PCO air cleaner. Moreover, the hybrid model based on fundamental principles provides important insights into physical or photochemical processes involved in UV-PCO technology.

(4) The relative rate limiting process between physical interactions and photochemical interactions was fully discussed through a simulation analysis. Depending on the physical properties of the catalyst, reactor geometries, operation conditions, as well as environmental conditions, the photochemical reaction occurring on the fixed active sites at the catalyst surface is the dominating process for the PCO system.

6. CONCLUSIONS AND RECOMMENDATIONS

6.1 Summary and Conclusion

A pilot four-parallel duct system was set-up to equitably and thoroughly evaluate the performance of the UV-PCO air cleaners under the conditions relevant to the actual applications for a wide range of indoor air pollutants. This study employed two types of air filters: TiO_2/FGFs and TiO_2/CCFs, under the UVC or VUV illumination to examine the UV-PCO removal efficiency. A systematic parametric evaluation of the effects of various kinetic parameters, such as the types of chemical compounds, the inlet concentration, the airflow rate, the light intensity, and the relative humidity, that influence the PCO performance was conducted. In addition, gas-phase ozonation with a variety of compounds was first examined in a duct system where ozone was introduced by the VUV. Finally, the performance comparison of UVC-PCO and VUV-PCO was also discussed in detail due to the presence of ozone. Moreover, the formation of the by-products generated from an incomplete conversion was investigated to evaluate the impact of potential side effects for the application in mechanically ventilated buildings. The following section summarized the findings.

(1) The single-pass removal efficiency of the two types of air filters (TiO_2/FGFs and TiO_2/CCFs) in removing VOCs with various physical properties under the UVC or UVV illumination ranks as follows: alcohols > ketones > aromatics > alkanes.

(2) The conversion rate of different compounds was investigated as a function of various parameters: the inlet concentration, the airflow rate, the irradiance, and the RH, all of which have significant influence on the PCO removal performance. The trend of a

decrease in the inlet concentration, a decrease in the flow rate, an increase in the irradiance, or a decrease in the RH, resulting in high removal efficiency was distinctly observed. Competition for the adsorption sites, residence time and the number of effective hydroxyl radicals are logical interpretations of these observations.

(3) Except for ketones, the ozone removal efficiency of alkanes, alcohols, and aromatics was investigated for the three concentration levels and was significantly reduced with an increase in the inlet concentrations of the challenge compound. Additionally, the conversion rates of various VOCs increased with ozone concentrations. Furthermore, the conversion rates of VOCs by VUV-PCO were higher than those caused by UVC-PCO due to the presence of ozone.

This study also carried out a systematic evaluation of adsorption performance of TiO_2/FGFs, TiO_2/CCFs, and the original CCFs air filters at various humidity conditions for eight different pollutants. TiO_2/FGFs, TiO_2/CCFs, and CCFs were characterized by SEM for morphology and N_2 adsorption isotherm for BET surface area and pore structure. A bench-scale adsorption test was setup and constructed, and the adsorption tests were performed at various relative humidity conditions and the four different injection concentrations for each compound. More detailed findings are as follows:

(1) Adsorption capacity can be ranked as: CCFs > TiO_2/CCFs > TiO_2/FGFs, which is consistent with the order of measured BET surface areas of the three air filters. This shows that the adsorption performance is affected by the properties of substrates.

(2) The test results for the TiO_2/FGFs demonstrate that the TiO_2/FGFs air filter presents hydrophilic property, and that the compounds with a high polarity show a higher

affinity to the surface of the TiO_2/FGFs air filter due to the strong intermolecular forces. The adsorption capacity of the selected chemical classes ranks as follows: alcohols > ketones > aromatics > alkanes. Moreover, a larger compound in the same chemical class has a greater adsorption coefficient because of the van der Waals forces. The test results for the TiO_2/CCFs show that the CCFs belong to a non-polar substrate which prefers to adsorb non-polar compounds. Therefore, the adsorptive performance is the sum of the interactions between the surface constituents and a specific VOC.

(3) An increase in RH decreases the adsorption capacity for three tested media, which is attributable to the strong hydrogen bonding of water. In addition, the influence of RH on the adsorption behavior of the TiO_2/CCFs is less important than that on the TiO_2/FGFs.

(4) Due to the differences in adsorption performance, photocatalytic activity of the TiO_2/CCFs air filter is obviously higher than that of TiO_2/FGFs. High performance of TiO_2/FGFs provides a promising direction to explore other supporting substrates with a high adsorptive ability.

Finally, this research developed a time-dependent model for predicting the performance of an in-duct PCO air cleaner under the conditions relevant to the actual applications. The model was developed by integrating the light scattering model, the reaction kinetic model, the mass balance, as well as the optional ozonation model. The comprehensive model incorporates the influences of properties of light sources and the catalyst, the reactor geometry, the mass transfer parameters, the kinetic parameters, the operational conditions, as well as the ozonation effect. These parameters can be estimated

easily from the experiments and/or the empirical equations. The UV-PCO model and the UV-PCO model combined with the ozonation model were validated with experimental results for the TiO_2/FGFs air filters under different conditions. There was a good agreement between the prediction made by the model and the experimental results. It was also demonstrated that the developed model can be applied to predict the UV-PCO performance for the TiO_2/CCFs air filters. The dominating process in this system was the photochemical reaction occurring on the fixed catalyst active sites.

The main advantages of this model are:

(1) The model parameters can be measured independently.

(2) The time-dependent model can predict the single-pass removal efficiency of the UV-PCO air cleaners more accurately.

(3) This model can be used to investigate the effects of the key parameters, including the chemical compound types, inlet concentration, RH, irradiance, airflow rate, as well as ozonation, on the performance of UV-PCO.

(4) Optimization of the VOCs removal process in the PCO system can be carried out by analysing of the dominating process between the physical and photochemical interactions.

6.2 Recommendations for Further Research

The in-duct UV-PCO air cleaners to be incorporated into a building's HVAC system are still in the experimental phase. If future work is conducted in the wide commercialization of the in-duct UV-PCO air cleaners, the following section represents some possible suggested directions.

(1) Optimization of the design of the UV-PCO devices with a low-pressure drop, reasonable retention time, appropriate lamp configuration, low by-product generation, as well as acceptable removal efficiency.

(2) The composition of the indoor pollutants is quite complex and their concentrations can vary greatly. This research on the degradation characteristics of PCO is mainly focused on the removal of a single indoor pollutant. Future research could explore the degradation characteristics of PCO with a mixture of pollutants.

(3) Long-term experiments (duration of a test of around one month) of UV-PCO should be conducted in order to investigate the deactivation of the catalyst, as well as the effect of a gradual decline in irradiance. Effective regeneration method also needs to be developed to reduce the costs of the catalyst replacement.

(4) Developing a new catalyst with low band-gap energy can be done, so that the UV output can be efficiently used. Also, efforts can be put into developing a new supporting substrate with a large surface area. This, on the one hand, will allow the substrate to adsorb a large amount of the VOC molecules on the catalyst surface and thus cause subsequent photochemical reactions. On the other hand, it can relatively prolong the residence time of the VOC molecules within the catalysts.

(5) Due to the presence of the by-products inevitably generated during PCO, combining the PCO air cleaner with a chemisorbent system can be an effective solution for practical applications. The choice of chemical adsorbent and the replacement cycle need to be further studied on the basis of the completed research on the by-products.

References

Adamson, A.W. (1982) *Physical Chemistry of Surfaces*, fourth edition, Wiley, New York.

Ai, Z., Ho, W., Lee, S., Zhang, L. (2009) Efficient photocatalytic removal of NO in indoor air with hierarchical bismuth oxybromide nanoplate microspheres under visible Light. *Environmental Science & Technology*, 43, 4143-4150.

Alberici, R.M., Jardim, W.E. (1997) Photocatalytic destruction of VOCs in the gas-phase using titanium dioxide. *Applied catalysis B: Environmental*, 14, 55-68.

Alexiadis, A. (2006) 2-D radiation field in photocatalytic channels of square, rectangular, equilateral triangular and isosceles triangular sections. *Chemical Engineering Science*, 61, 516-525.

Ameen, M.M., Raupp, G.B. (1999) Reversible catalyst deactivation in the photocatalytic oxidation of dilute o-xylene in air, *Journal of catalysis*, 184, 112-122.

Ao, C.H., Lee, C.Y., Mak, C.L. and Chan, L.Y. (2003a) Photodegradation of volatile organic compounds (VOCs) and NO for indoor air purification using TiO_2: promotion versus inhibition effect of NO. *Applied Catalysis B: Environmental*, 42, 119-129.

Ao, C.H., Lee, C.Y. and Yu, J.C. (2003b) Photocatalyst TiO_2 supported on glass fiber for indoor air purification: effect of NO on the photodegradation of CO and NO_2. *Journal of Photochemistry and Photobiology A: Chemistry*, 156, 171-177.

Ao, C.H., Lee, S.C. (2003) Enhancement effect of TiO_2 immobilized on activated carbon filter for the photodegradation of pollutants at typical indoor air level, *Applied Catalysis B: Environmental*, 44, 191-205.

Ao, C.H., Lee, S.C., Yu, J.Z.and Xu, J.H. (2004) Photodegradation of formaldehyde by photocatalyst TiO_2: effects on the presences of NO, SO_2 and VOCs, *Applied Catalysis B: Environmental*, 54, 41-50.

Ao, C.H., Lee, S.C. (2005) Indoor air purification by photocatalyst TiO_2 immobilized on an activated carbon filter installed in an air cleaner, *Chemical Engineering Science*, 60, 103-109.

ASHRAE. (1999) ANSI/ASHRAE Standard 52.2: Method of Testing General Ventilation Air-Cleaning Devices for Removal Efficiency by Particle Size, American Society of Heating, Refrigerating, and Air-Conditioning Engineers, Inc., Atlanta.

ASHRAE. (2008) ANSI/ASHRAE Standard 145.1: Laboratory Test Method for Assessing the Performance of Gas-Phase Air-Cleaning Systems: Loose Granular Media, American Society of Heating, Refrigerating, and Air-Conditioning Engineers, Inc.,

Atlanta.

ASHRAE. (2010) ANSI/ASHRAE Standard 55 Thermal Environmental Conditions for Human Occupancy, Atlanta: American Society of Heating Refrigeration and Air Conditioning Engineers, Inc.

ASHRAE. (2011) ANSI/ASHRAE Standard 145.2 Laboratory Test Method for Assessing the Performance of Gas-Phase Air-Cleaning Systems: Air-Cleaning Devices. Atlanta: American Society of Heating Refrigeration and Air Conditioning Engineers, Inc.

Atkinson, R., Carter, W.P.L. (1984) Kinetics and mechanisms of the gas-phase reactions of ozone with organic compounds under atmospheric conditions. *Chemical Reviews*, 84, 437-470.

Barrett, E. P., Joyner, L.G., Halenda, P.P. (1951) The determination of pore volume and area distributions in porous substances. I. Computations from nitrogen isotherms. *Journal of the American Chemical Society*, 73, 373–380.

Bailey, P.S. (1982) *Ozonation in organic chemistry, Volume II Nonolefinic Compounds*. Academic press, Inc., New York.

Bastani, A., Lee, C-S., Haghighat, F., Flaherty, C., Lakdawala, N. (2010) Assessing the Performance of Air Cleaning Devices – A Full Scale Test Method. *Building and Environment*, 45, 143-149.

Becker, R. (1979) Window air tightness and its influence on energy saving and minimum required ventilation. *Building and Environment*, 14(3), 157-165.

Bekbolet, M., Ciner, Z., Kilic M., Uyguner, C.S., Minero, C., Pelizzetti, E. (2009) Photocatalytic oxidation of dinitroaphthalenes: Theory and experiment. *Chemosphere*, 75, 1008-1014.

Books, B.O., Utter, G.M., DeBroy, J.A., Schimke, R.D. (1991) Indoor Air Pollution: an edifice complex. *Journal of Toxicology: Clinical Toxicology*, 29, 315-374.

Boulamanti, A.K., Korologos, C.A., Philippopoulos, C.J. (2008) The rate of photocatalytic oxidation of aromatic volatile organic compounds in the gas-phase, *Atmospheric Environment*, 42, 7844-7850

Bouzaza, A., Vallet, C., Laplanche, A. (2006) Photocatalytic degradation of some VOCs in the gas phase using an annular flow reactor – determination of the contribution of mass transfer and chemical reaction steps in the photo-degradation process. *Journal of Photochemistry and Photobiology A: Chemistry*, 177, 212-217.

Brown, S.K., Sim, M.R., Abramson, M.J., and Gray, C.N. (1994) Concentrations of volatile organic compounds in indoor air - A review. *Indoor Air*, 4, 123-134.

Brucato, A., Grisafi, F., and Urso, R. (1997) Economic evaluation of photon sources

for photocatalytic applications by means of spectral distribution analysis, *Proceedings of the International Conference on TiO_2 Photocatalytic Treatment of Water and Air, Orlando, FL*, 48.

Cao, L., Gao, Z., Suib, S.L., Obee, T.N., Hay, S.O. and Freihaut, J.D. (2000) Photocatalytic oxidation of toluene on nanoscale TiO_2 catalysts: Studies of deactivation and regeneration. *Journal of Catalysis*, 196, 253-261.

Casado, J.,Herrmann, J.M. and Pichat, P. (1990) Photo-transformation of o-xylene over atmospheric solid aersols in the presence of molecular oxygen and water. *Proceedings of the 5th Symposium on Physical-Chemical Behavior Atmospherics Pollution*, 283-288.

Changrani, R.G., Raupp, G.B. (2000) Two-Dimensional Heterogeneous model for a Reticulated-Foam Photocatalytic Reactor. *American Institute of Chemical Engineers Journal*, 46 (4), 829-842.

Chen, J., Li, G., He, Z., An, T., (2011) Adsorption and degradation of model volatile organic compounds by a combined titania-montmorillonite-silica photocatalyst. *Journal of Hazardous Materials*, 190, 416-423.

Chen, W., Zhang, J.S., Zhang, Z. (2005) Performance of air cleaners for removing multiple volatile organic compounds in indoor air. *ASHRAE Transactions*, 1101-1114.

Cheng, M., Brown, S.K. (2003) VOCs identified in Australian indoor air and product emission environments. *Proceedings of National Clean Air Conference, Newcastle*, Nov, 23-27.

Coronado J.M., Zorn M.E., Tejedor I.T., Anderson M.A., (2003) Photocatalytic oxidation of ketones in the gas phase over TiO_2 thin films: a kinetic study on the influence of water vapor. *Applied Catalysis B: Environmental*, 43, 329-344.

Cozzoli, P.D, Fanizza, E., Comparelli, R., Curri, M.L., Agostiano, A., Laub, D. (2004) Role of metal nanoparticles in TiO_2/Ag nanocomposite-based microheterogeneous photocatalysis. *The Journal of Physical Chemistry B*, 108, 9623–9630.

Dawson, A., Kamat, P.V. (2001) Semiconductor-metal nanocomposites: photoinduced fusion and photocatalysis of gold-capped TiO_2 (TiO_2/gold) nanoparticles. *The Journal of Physical Chemistry B*, 105, 960–966.

Debono, O., Thevenet, F., Gravejat, P., Hequet, V., Raillard, C., Lecoq, L., Locoge, N., (2011) Toluene Photocatalytic oxidation at ppb levels: kinetic investigation and carbon balance determination. *Applied Catalysis B: Environmental*, 106, 600-608.

Delage, B.F., Pre, P., Cloirec, P.L. (1999) Effects of moisture on warning of activated carbon bed during VOC adsorption. *Journal of Environmental Engineering*, 125, 1160-1167.

Demeestere, K., Dewulf, J., Langenhove, H.V., Sercu, B. (2003) Gas-solid adsorption of selected volatile organic compounds on titanium dioxide Degussa P25. *Chemical Engineering Science*, 58, 2255-2267.

Devahasdin, S., Fan, C., Li, K.Y., Chen, D.H. (2003) TiO_2 photocatalytic oxidation of nitric oxide: transient behavior and reaction kinetics. *Photochemistry and Photobiology A: Chemistry*, 156, 161-170.

d'Hennezel, O., Pichat P., and Ollis D.F. (1998) Benzene and toluene gas-phase photocatalytic degradation over H_2O and HCL pretreated TiO_2: by-products and mechanisms. *Journal of Photochemistry and Photobiology A: Chemistry*, 118, 197-204.

Disdier, J., Pichat, P., and Mas, D. (2005) Measuring the effect of photocatalytic purifiers on indoor air hydrocarbons and carbonyl pollutants. *Journal of the Air & Waste Management Association*, 55, 88-96.

Doucet, N., Bocquillon, F., Zahraa, O., Bouchy, M. (2006) Kinetics of photocatalytic VOCs abatement in a standardized reactor. *Chemosphere*, 65, 1188-1196.

Du, E., Zhang, Y.X., Zheng, L. (2009) Photocatalytic degradation of dimethyl phthalate in aqueous TiO_2 suspension: a modified Langmuir-Hinshelwood model, *Reaction Kinetics and Catalysis Letters*, 97, 83-90.

Dullien, F. A. L. (1992) *Porous Media: Fluid Transport and Pore Structure*. Academic Press: New York.

Edwards, M.E., Villa, C.M., Hill, C.G., Chapman, T.W. (1996) Effectiveness factor for photocatalytic reactions occurring in planar membranes. *Industrial & Engineering Chemistry Research*, 35, 712-720.

Einaga, H., Futamura, S., Ibusuki, T. (2002) Heterogeneous photocatalysis of benzene, toluene, cyclohexene and cyclohexane in humidified air: comparison of decomposition behavior on photoirradiated TiO_2 catalyst. *Applied Catalysis B: Environmental*, 38, 215-225.

EPA Method TO-11A, (1999) Determination of Formaldehyde in Ambient Air Using Adsorbent Cartridge Followed by High Performance Liquid Chromatography (HPLC) [Active Sampling Methodology].

Froment, G. F., Bischoff, K. B. (1979) *Chemical Reactor Analysis and Design*. Wiley: New York.

Fu, X., Clark, L.A., Zeltner, W.A., Anderson, M.A. (1996b) Effects of reaction temperature and water vapor content on the heterogeneous photocatalytic oxidation of ethylene. *Journal of Photochemistry and Photobiology A: Chemistry*, 181-186.

Fujishima, A. and Honda, K. (1972) Electrochemical photolysis of water at a semiconductor electrode. *Nature*, 238, 37–38.

Gaya, V.I., Abdullah, A.H. (2008) Heterogeneous photocatalytic degradation of organic contaminants over titanium dioxide: A review of fundamentals, progress and problems. *Journal of Photochemistry and Photobiology C: Photochemistry Reviews*, 9, 1-12.

Geiss, O., Giannopoulos, G., Tirendi, S., Barrero-Moreno, J., Larsen, B.R., Kotzias, D. (2011) The AIRMEX study—VOC measurements in public buildings and schools/kindergartens in eleven European cities: Statistical analysis of the data. *Atmospheric Environment*, 45, 22, 3676-3684.

Ginestet, A., Pugnet, D., Rowley J., Bull K., and Yeomans H. (2005) Development of a new photocatalytic oxidation air filter for aircraft cabin. *Indoor Air*, 15, pp. 326-334.

Ginestet, A., Blondeau, P., Frochot, D., Kaluzny, P., Lefèvre M.C., Ott M., de Blay, F., Pepin, L., Pugnet, D., Ribot, B., Squinazi, F. (2008) A new test method for indoor air cleaner efficiency determination and harmlessness assessment. *Proceedings of the 11th international conference on Indoor Air quality and climate. CD Rom, Copenhagen*, August 17-22, 2008.

Guo, T., Bai, Z., Wu, C., Zhu, T. (2008) Influence of relative humidity on the photocatalytic oxidation (PCO) of toluene by TiO_2 loaded on activated carbon fibers: PCO rate and intermediates accumulation, *Applied Catalysis B: Environmental*, 79, 171-178.

Gupta, S., Khare, M., Goyal, R. (2007) Sick building syndrome- A case study in a multistory centrally air-conditioned building in the Delhi City. *Building and Environment*, 42(8), 2797-2809.

Hager, S., Bauer, R. (1999) Heterogeneous photocatalytic oxidation of organic for air purification by near UV irradiated titanium dioxide. *Chemosphere*, 38, 1549-1559.

Haghighat, F., Lee, C-S, Pant, B, Bolourani, G., Lakdawala, N., Bastani, A. (2008) Evaluation of activated carbon for gas-phase air cleaning – Toward design of an immune and sustainable buildings. *Atmospheric Environment*, 42, 8176-8184.

Haghighat, F. and De Bellis, L. (1998) Material emission rates: Literature review, and impact of indoor air temperature and relative humidity. *Building and Environment*, 33, 261-277.

Hansen, W. (1995) The IAQ challenge to facility management: healthy building through affordable indoor air quality programs. *Facilities*, 13(12), 12-20.

Hawthorn, R. D. (1974) Afterburner catalysts: Effect of heat and mass transfer between gas and catalyst surface. *AIChE Symposium Series*, 70, 428–438.

Health Canada, 93-EHD-166 (1995) Indoor Air Quality in Office Buildings: A Technical Guide.

Hedge, A., Sterling, E.M., Sterling, T.D. (1986) Building illness based on questionnaire responses. *ASHRAE Transactions*, 31-43.

Hedge, A., Burqe, P.S., Robertson, A.S., Wilson, S., Harris-Bass, J. (1989) Work-related illness in offices: A proposed model of the "Sick Building Syndrome". *Environment International*, 15(1-6), 143-158.

Henschel, D.B. (1998) Cost analysis of activated carbon versus photocatalytic oxidation for removing organic compounds from indoor air. *Journal of the Air & Waste Management Association*, 48, 985-994.

Hernandez-Alonso, M.D., Tejedor-Tejedor, I., Coronado, J.M., Anderson, M.A., Soria, J. (2009) Operando FTIR study of the photocatalytic oxidation of acetone in air over TiO2-ZrO2 thin films. *Catalysis Today*, 143, 364-373.

Herrmann, J.M., Disdier, J., and Pichat, P. (1981) Oxygen species ionosorbed on powder photocatalyst oxides from room-temperature photoconductivity as a function of oxygen pressure. *Journal of the Chemical Society*, Faraday Trans.1, 77, 2815-2826.

Hill, CG. (1977) *An Introduction to Chemical Engineering Kinetics and Reactor Design*. Wiley: New York.

Hodgson, A.T., Destaillats, H., Sullivan, D.P., Fisk, W.J. (2007) Performance of ultraviolet photocatalytic oxidation for indoor air applications. *Indoor Air*, 17, 305-316.

Hossain, M.M., Raupp, G.B. (1998) Radiation Field Modeling in a Photocatalytic Monolith Reactor. *Chemical Engineering Science*, 53, 3771-3780.

Hossain, M.M., Raupp, G.B. (1999) Polychromatic radiation field model for a honeycomb monolith photocatalytic reactor. *Chemical Engineering Science*, 54, 3027-3034.

Hossain, M.M., Raupp, G.B., Hay, S.O., Obee, T.N. (1999) Three-dimensional developing flow model for photocatalytic monolith reactor. *AIChE Journal*, 45, 1309-1321.

Hougen, O.A., and Watson, K.M. (1947) *Chemical process principles, part 3, Kinetics and Catalysis*. Wiley, New York, 906-907.

Huang, H., and Haghighat, F. (2003). Building materials VOC emissions- a systematic parametric study. *Building and Environment*, 38(8), 995-1005.

Huang, R.J., Demirel, T., Mcgee, T.D. (1973) Calculation and interpretation of surface free energy of wetting of E-glass by vapors. *Journal of the American Ceramic Society*, 56, 87-91.

Ibusuki, T., Takeuchi, K. (1986) Toluene oxidation on u.v.-irradiated titanium dioxide with and without O_2, NO_2 or H_2O at ambient temperature. *Atmospheric Environment*, 20,

1711–1715.

ISO 16000-6:2004(E) Indoor air---- Part 6: Determination of volatile organic compounds in indoor air and test chamber air by active sampling on Tenax-TA sorbent, thermal desorption and gas chromatography using MS/FID.

Jacoby, W.A. (1993) Destruction of trichloroethylene in air via semiconductor mediated gas–solid heterogeneous photocatalysis. PhD dissertation, Department of Chemical Engineering, University of Colorado, USA.

Jeong, J., Sekiguchi, K., Lee, W., Sakamoto, K. (2005) Photodegration of gaseous volatile organic compounds (VOCs) using TiO_2 photoirradiated by an ozone-producing UV lamp: decomposition characteristics, identification of by-products and water-soluble organic intermediates. *Journal of Photochemistry and Photobiology A: Chemistry*, 169, 279-287.

Jin, S.S., Sharpless C., Linden K., Kelly K., Ferran B. (2007) Aging evaluation of medium-pressure mercury lamps under typical operating conditions for drinking water disinfection applications. *Water Environment Federation, Disinfection*, 17, 276-292.

Jing, L., Xin B., Yuan F., Wang B., Shi K., Cai W., Fu H. (2004) Deactivation and regeneration of ZnO and TiO_2 nanoparticles in the gas phase photocatalytic oxidation of n-C_7H_{16} or SO_2. *Applied Catalysis A: General*, 275, 49-54.

Jo, W.K., Park, K.H. (2004) Heterogeneous photocatalysis of aromatic and chlorinated volatile organic compounds (VOCs) for non-occupational indoor air application. *Chemosphere*, 57, 555-565.

Kapoor, A., Ritter J.A., Yang R.T. (1990) An extended Langmuir Model for adsorption of gas mixtures on heterogeneous surfaces. *Langmuir*, 6, 660-664.

Khalifa, H.E. (2005) Effect of nonuniform UV irradiation on Photocatalytic Air purifier performance. *ASHRAE Transactions*, 111, 535-542.

Kholafaei, H., Lee, C.-S., and Haghighat, F. (2010) Full-Scale test method for the performance evaluation of in-duct filters with mixture of VOC. *Proceedings of the International Conference on Clima*, Turkey (9-12 May).

Kirchnerova, J., Herrera, Cohen M.-L., Guy, C., Klvana D. (2005) Photocatalytic oxidation of n-butanol under fluorescent visible light lamp over commercial TiO_2 (Hombicat UV 100 and Degussa P25). *Applied Catalysis A: General*, 282, 321-332.

Kolinko, P.A., Kozlov, D.V. (2008) Photocatalytic oxidation of tabun stimulant-diethyl cyanophosphate: FTIR in situ investigation. *Environmental Science and Technology*, 42, 4350-4355.

Kowalska, E., Remita, H., Colbeau-Justin, C., Hupka, J., Belloni, J. (c2008) Modification of Titanium Dioxide with Platinum Ions and Clusters: Application in

Photocatalysis. *Journal of Physical Chemistry*, 112: 1124–1131.

Krysa, J., Keppert, M., Jirkovsky, J., Stengl, V., Subrt J. (2004) The effect of thermal treatment on the properties of TiO_2 photocatalyst. *Materials Chemistry and Physics*, 86, 333–339.

Lewandowski, M., Ollis D.F. (2003) Extension of a two-site transient kinetic model of TiO_2 deactivation during photocatalytic oxidation of aromatics: concentration variations and catalyst regeneration studies. *Applied Catalysis B: Environmental*, 45, 223-238.

Litchin, N.N., Avudaithai, M., Berman, E., Grayfer, A. (1996) TiO_2-photocatalyzed oxidative degradation of binary mixtures of vaporized organic compounds. *Solar energy*, 56, 377-385.

Li, X.Z., Hou M.F., Li F.B., Chua H. (2006) Photocatalytic oxidation of methyl mercaptan in foul gas for odor control. *Industrial and Engineering Chemistry Research*, 45, 487-494.

Lin, C.Y., Li C.S. (2003) Effectiveness of titanium dioxide photocatalyst filter for controlling bioaerosols. *Aerosol Science and Technology*, 37, pp.162-170

Luo, Y., Ollis, D.F. (1996) Heterogeneous photocatalytic oxidation of trichloroethylene and toluene mixtures in air: kinetic promotion and inhibition, time-dependent catalyst activity. *Journal of Catalysis*, 163, 1–11.

Lyman, W. J., Reehl, W. F., Rosenblatt, D. H. (1990) *Handbook of Chemical Property Estimation Methods: Environmental Behavior of Organic Compounds*. American Chemical Society, Washington, DC.

Masel, R.I. (1996) *Principles of adsorption and reaction on solid surfaces*. New York: Wiley & Sons

Matejcik, S., Cicman, P., Kiendler, A., Skalny, J.D., Illenberger, E., Stamatovic, A., Mark, T.D. (1996) Low-energy electron attachment to mixed ozone/ oxygen clusters. *Chemical Physics Letters*, 261, 437-442.

Maudhuit, A., Raillard, C., Hequet, V., Coq, L.L., Sablayrolles, J., Molins, L., (2011) Adsorption phenomena in photocatalytic reactions: The case of toluene, acetone and heptane. *Chemical Engineering Journal*, 170, 464-470.

Mills, A., Hunte, S. L., (1997) An overview of semiconductor photocatalysis. *Journal of Photochemistry and Photobiology A: Chemistry*, 108, 1-35.

Morrison, G.C., Nazaroff W.W., Cano-Ruiz, J. A., Hodgson, A.T., Modera, M.P. (1998) Indoor air quality impacts of ventilation ducts: ozone removal and emissions of volatile organic compounds. *Journal of the Air & Waste Management Association*, 48, 941-952.

Nagda, N.L., Rector, H.E. (2003) A critical review of reported air concentrations of organic compounds in aircraft cabins. *Indoor Air*, 13, 292-301.

Namiesnik, J., Gorecki, T., Kozdronzabiegala, B., Lukasiak, J. (1992) Indoor air quality (IAQ), pollutants, their sources and concentration levels. *Building and Environment*, 27, 339-356.

NIOSH Pocket Guide to Hazardous Chemicals, National Institute of Occupational Safety and Health, (2010) http://www.cdc.gov/niosh/npg/, September 5, 2012 last accessed.

Noguchi, T., Fujishima, A, Sawunytama, P., Hashimoto, K. (1998) Photocatalytic degradation of gaseous formaldehyde using TiO2 film. *Environmental Science and Technology*, 32, 3831–3833.

Nq, A.H. (1992). Energy-efficient air-conditioning system design for better indoor air quality without energy penalty. *IES Journal*, 32(6), 41-49.

Obee, T.N., Brown, R.T. (1995) TiO_2 photocatalysis for indoor air applications: effects of humidity and trace contaminant levels on the oxidation rates of formaldehyde, toluene and 1,3-butadiene. *Environmental Science and Technology*, 29, 1223–1231.

Obee, T.N. (1996) Photooxidation of sub-parts-million toluene and formaldehyde levels on titania using a glass-plate reactor. *Environmental Science and Technology*, 30, 3578-3584.

Obee, T.N., Hay, S.O. (1997) Effects of moisture and temperature on the photooxidation of ethylene on titania. *Environmental Science and Technology*, 31, 2034–2038.

Obee, T.N. and Hay, S.O. (1999) The estimation of photocatalytic rate constants based on molecular structure: extending to multi-component systems. *Journal of Advanced Oxidation Technologies*, 4, 1–6.

Ortiz-Gomez A., Serrano-Rosales B., Salaices M., Lasa H. (2007) Photocatalytic oxidation of phenol: Reaction network, kinetic modeling, and parameter estimation. *Industrial and Engineering Chemistry Research*, 46, 7394-7409

Ozisik, M.N. (1973) *Radiative Transfer*, 1st ed. Wiley, New York.

Park, D.-R., Zhang, J., Ikeue, K., Yamashita, H., and Anpo, M. (1999) Performance of TiO_2 Powder Coated Packaging Film in Ethylene Removal. *Journal of Catalysis*, 185, 114–119.

Park, K-W. (2004) An illuminance ratio prediction method for daylighting control of buildings. PhD thesis, Concordia University, Quebec, Canada.

Pengyi, Z., Fuyan, L., Gang, Y., Qing, C., Wanpeng, Z. (2003) A comparative study

on decomposition of gaseous toluene by O_3/UV, TiO_2/UV and O_3/TiO_2/UV. *Journal of photochemistry and Photobiology A: Chemistry*, 156, 189-194

Puma, G.L., Estivill, I.S., Obee, T.N., Hay, S.O. (2009) Kinetics rate model of the photocatalytic oxidation of trichloroethylene in air over TiO_2 thin films. *Separation and Purification Technology*, 67, 226-232.

Restrepo, M.L., Mosquera, M.A. (2009) Accurate correlation, thermochemistry, and structural interpretation of equilibrium adsorption isotherms of water vapor in zeolite 3A by means of a generalized statistical thermodynamic adsorption model. *Fluid Phase Equilibria*, 283, 73-88.

Satterfield, C.N. (1970) *Mass Transfer in Heterogeneous Catalysis*, MIT Press, Cambridge, Mass.

Shang, J., Du, Y.G., Xu, Z.L. (2002) Photocatalytic oxidation of heptane in the gas-phase over TiO_2. *Chemosphere*, 46, 93-99.

Shiraishi, F., Ishimatsu, T., (2009) Toluene removal from indoor air using a miniaturized photocatalytic air purifier including a preceding adsorption/ desorption unit. *Chemical Engineering Science*, 64, 2466–2472.

Siegel, R., Howell, J.R. (1992) *Thermal Radiation Heat Transfer*, 3rd ed. McGraw-Hill, New York.

Silva, C.G., Faria, J.L. (2009) Effect of key operational parameters on the photocatalytic oxidation of phenol by nanocrystalline sol-gel TiO_2 under UV irradiation. *Molecular Catalysis A: Chemical*, 305, 147-154.

Sleiman M., Conchon P., Ferronato C., Chovelon J.M. (2009) Photocatalytic oxidation of toluene at indoor air levels (ppbv): Towards a better assessment of conversion, reaction intermediates and mineralization. *Applied Catalysis B: Environmental*, 86, 159-165.

Sundell, J. (1996). What we know, and don't know about sick building syndrome. *ASHRAE Journal*, 38(6), 6.

Tanaka, Y. and Suganuma, M. (2001) Effects of Heat Treatment on Photocatalytic Property of Sol-Gel Derived Polycrystalline TiO_2. *Journal of Sol-Gel Science and Technology*, 22, 83–89.

Thompson, T.L., Yates, J.T., (2006) Surface science studies of the photoactivation of TiO_2- new photochemical process. *Chemical Reviews*, 106, 4428-4453.

Tillman, Jr., Fred, D., Weaver, J.W. (2006). Uncertainty from synergistic effects of multiple parameters in the Johnson and Ettinger (1991) vapor intrusion model. *Atmospheric Environment*, 40(22), 4098-4112.

Tomasic, V., Jovic, F., Gomzi, Z. (2008) Photocatalytic oxidation of toluene in the gas phase: Modeling an annular photocatalytic reator. *Catalysis Today*, 137, 350-356.

Tomida, T., Okada N., Katoh, M., (2005) Adsorption and photocatalytic decomposition of volatile organic compounds on photocatalyst of TiO_2- Silica Beads. *Adsorption*, 11, 865-869.

Tomkiewics, M., Dagan, G., Zhu, Z. (1994) Morphology and photocatalytic activity of TiO2 Aerogels. *Research on Chemical Intermediates*, 20, 701-710.

Totten, G.E., Mackenzie D.S. (2003) *Handbook of Aluminum: Volume 2: Alloy Production and Materials Manufacturing*. CRC Press, New York.

Turchi, C.S., Rabago, R., Jassal, A. (1995) Destruction of volatile organic compound (VOC) emissions by photocatalytic oxidation (PCO): benchscale test results and cost analysis, Technology Transfer Report # 95082935A-ENG SEMATECH, Inc.

VanOsdell, D.W. (1994). Evaluation of test methods for determining the effectiveness and capability of gas-phase air filtration equipment for indoor air applications-phase I: literature review and test recommendations. *ASHRAE Transaction*. 100: 511-523.

Vincent, G., Marquaire, P.M., Zahraa, O. (2009) Photocatalytic degradation of gaseous 1-propanol using an annular reactor: Kinetic modeling and pathways. *Journal of Hazardous Materials*, 161, 1173-1181.

Vorontsov, A.V. (2007) Opposite effect of gas phase H2O2 on photocatalytic oxidation of acetone and benzene vapors. *Catalysis Communications*, 8, 2100-2104.

Votruba, J., Sinkule J., Hlavacek, V., Skrivanek. (1975) Heat and mass transfer in honeycomb catalysis II. *Chemical Engineering Science*, 30, 201-206.

Wang, K., Tsai, H., Hsieh, Y. (1998) A study of photocatalytic degradation of trichloroethylene in vapor phase on TiO_2 photocatalyst. *Chemosphere*, 36, 2763–73.

Wang, K.H., Hsieh, Y.H., Lin, C.H., Chang, C.Y. (1999) The study of the photocatalytic degradation kinetics for dichloroethylene in vapor phase. *Chemosphere*, 39, 1371-1384.

Wang, B., Mortazavi, R. and Haghighat, F. (2009) Evaluation of Modeling and Measurement Techniques of Ultraviolet Germicidal Irradiation Effectiveness – Towards Design of Immune Building. *Indoor and Built Environment*, 18, 101-113.

Worth, D.J., Spence, A., Crumpton, P.I. (1996) Radiative Exchange between Square Parallel Channels in a Concentric Monolith Structure. *International Journal of Heat Mass Transfer*, 39(7), 1463.

Wilke, C.R., Lee, C.Y. (1955) Estimation of diffusion coefficients for gases and vapors. *Industrial Engineering Chemistry*, 47, 1253–1257.

Yang, M., Zhang, J.S., Li, H., Dang, T.Q., Gao, X.F. (2005). Determination of building materials' transport properties for modeling VOC emissions. *ASHRAE Transactions*, 111 (part 1), 88-100.

Yi, Z., Liu, J., Wei, W., Wang, J., Lee, S.W. (2008) Photocatalytic performance and microstructure of thermal-sprayed nanostructured TiO_2 coatings. *Ceramics International*, 34, 351-357.

Yu, H.L., Zhang, K.L., Rossi C. (2007) Experimental study of the photocatalytic degradation of formaldehyde in indoor air using a nano-particulate titanium dioxide photocatalyst. *Indoor and Built Environment*, 16, 529-537.

Yu, K., Lee, G.W.M, Huang, W., Wu, C., Yang, S. (2006) The correlation between photocatalytic oxidation performance and chemical/physical properties of indoor volatile organic compounds. *Atmospheric Environment*, 40, 375-385.

Yu, Q.L., Brouwers, H.J.H. (2009) Indoor air purification using heterogeneous Photocatalytic oxidation. Part I: Experimental study. *Applied Catalysis B: Environmental*, 92, 454-461.

Yu, B., Deng, B.Q., Kim, C.N. (2008) Performance evaluation of P-1 model in a photocatalytic reactor. *Chemical Engineering Science*, 63, 5552-5558.

Zeltner, W.A., Tompkins, D.T. (2005) Shedding light on photocatalysis. *ASHRAE Transactions*, 111, 523-534.

Zhang, Y., Yang, R., Zhao, R. (2003) A model for analyzing the performance of photocatalytic air cleaner in removing volatile organic compounds. *Atmospheric Environment*, 37, 3395-3399.

Zhang, P., Liu, J. (2004) Photocatalytic degradation of trace hexane in the gas phase with and without ozone addition: kinetic study. *Journal of Photochemistry and Photobiology A: Chemistry*, 167, 87-94.

Zhang, P.Y., Liang, F.Y., Yu, G., Chen, Q., Zhu, W.P. (2003a) A comparative study on decomposition of gaseous toluene by O_3/UV, TiO_2/UV and O_3/TiO_2/UV. *Journal of Photochemistry and Photobiology A: Chemistry*, 156, 189–194.

Zhao, J., Yang, X. (2003) Photocatalytic oxidation for indoor air purification: a literature review. *Building and Environment*, 38, 645-654.

Zhong, L., Haghighat, F., Blondeau, P., Kozinski, J. (2010) Modeling and Physical Interpretation of Photocatalytic Oxidation Efficiency in Indoor Air Applications. *Building and Environment*, 45, 2689-2697.

Zhong, L., and Haghighat, F. (2011) Modeling and validation of a photocatalytic oxidation reactor for indoor environment applications. *Chemical Engineering Science*, 66, 5945-5954.

Zhong, L., Lee, C-S., Haghighat, F. (2012) Adsorption Performance of Titanium Dioxide (TiO_2) Coated Air Filters. *Journal of Hazardous Materials*, 243, 340-349.

APPENDIX A: Multi-gas Monitor Calibration

The photoacoustic multi-gas monitor (INNOVA 1312) was calibrated for selected chemicals: toluene, p-xylene, acetone, MEK, hexane, octane, ethanol, and 1-butanol. The schematic diagram of calibration setup is presented in Figure A-1. The laboratory compressed air was used as the carrier gas and its flow rate was controlled by a mass flow meter (Matheson Model 8274). The compressed air was then passing through a granular activated carbon (GAC) filter to removal potential contaminants in the air. Since INNOVA has highest sensitivity when relative humidity (RH) is around 50%, the humidity of the mixed stream was kept at 50% by adjusting the flow rate of the compressed air into the distilled water bottle. Moreover, the temperature of the distilled water bottle was maintained constant using a water bath so that it could provide water vapor with a steady concentration. The selected chemicals are liquid state at room temperature; they were automatically injected through a syringe pump (KD Scientific). The injected concentrations of selected chemicals were calculated on the basis of airflow rate, chemical injection rate and the chemical properties. Table A-1 shows the calculated concentration of different chemicals for each injection rate and readings of the gas analyzer for each challenge concentration. The calibration curves of detector readings versus actual concentrations for each compound are given in Figure A-2.

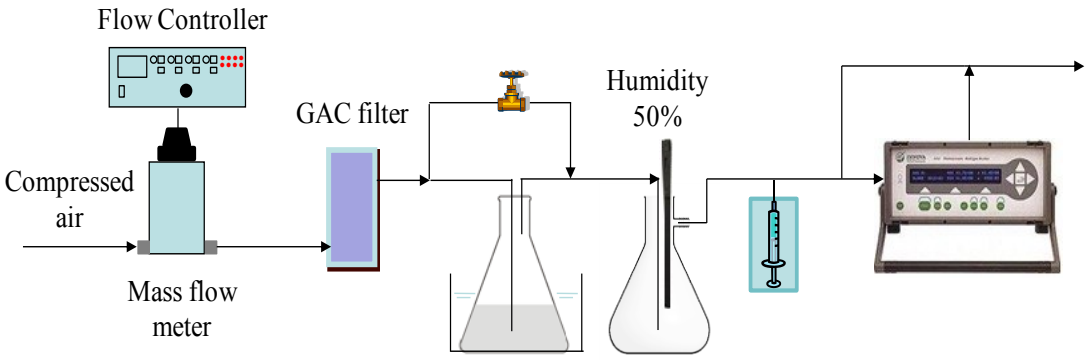

Figure A-1 Calibration setup for INNOVA 1312

Table A-1 Actual concentration and reading for each injection rate

Compound	Injection rate (uL/min)	C (mg/m^3)	C (ppm)	Reading (ppm)
Toluene (Compressed air: 10.16L/min)	0	0	0	0.965
	0.5	1.908	0.492	1.39
	1	3.816	1.006	2.01
	2	7.632	1.990	2.71
	3	11.448	2.996	3.68
	5	19.080	5.009	5.32
p-Xylene (Compressed air: 10.24L/min)	0	0	0	0.869
	0.5	2.148	0.499	1.59
	1	4.295	0.978	2.02
	2	8.591	1.937	3.63
	3	12.886	2.916	5.28
	5	21.477	4.872	8.21
MEK (Compressed air: 10.16L/min)	0	0	0	0.968
	0.5	1.494	0.504	1.82
	1	2.988	1.008	2.40
	2	5.975	1.989	3.99
	3	8.963	2.996	4.98
	5	14.938	5.012	7.91
Acetone (Compressed air: 10.24L/min)	0	0	0	0.935
	0.5	1.204	0.515	1.15
	1	2.409	0.997	1.37
	2	4.817	1.994	1.82
	3	7.226	2.991	2.34
	5	12.044	5.096	3.40
Ethanol (Compressed air: 10.45L/min)	0	0	0	1.06
	0.5	0.936	0.475	1.87
	1	1.872	0.989	2.49
	2	3.744	1.978	4.99

	3	5.617	2.927	6.89
	5	9.361	4.905	10.34
1-butanol (Compressed air: 10.60L/min)	0	0	0	1.01
	0.5	1.484	0.493	3.01
	1	2.969	0.961	4.65
	2	5.938	1.922	8.16
	3	8.906	2.908	11.86
	5	14.844	4.830	19.09
Hexane (Compressed air: 10.21L/min)	0	0	0	0.951
	0.5	1.792	0.503	4.01
	1	3.585	1.006	7.42
	2	7.169	2.012	12.79
	3	10.754	3.018	19.09
	5	17.923	5.011	31.12
Octane (Compressed air: 10.17L/min)	0	0	0	0.974
	0.5	2.385	0.511	4.99
	1	4.770	1.008	8.03
	2	9.540	2.016	15.39
	3	14.310	3.023	23.01
	5	23.850	5.039	39.25

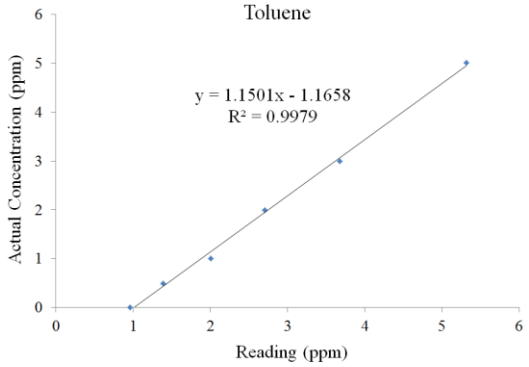

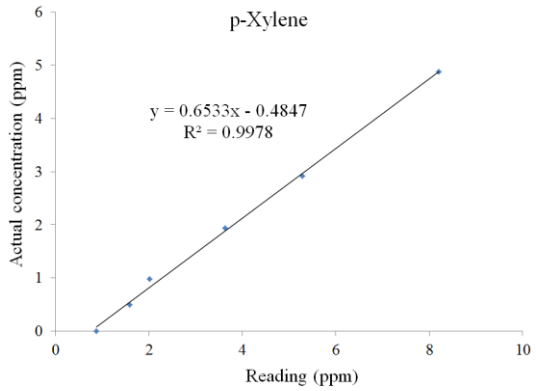

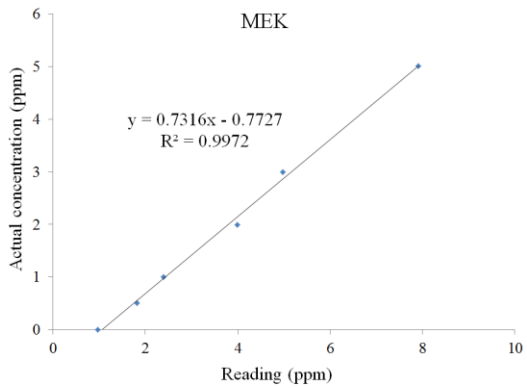

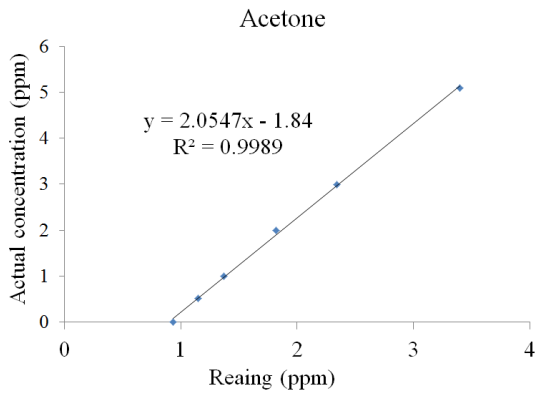

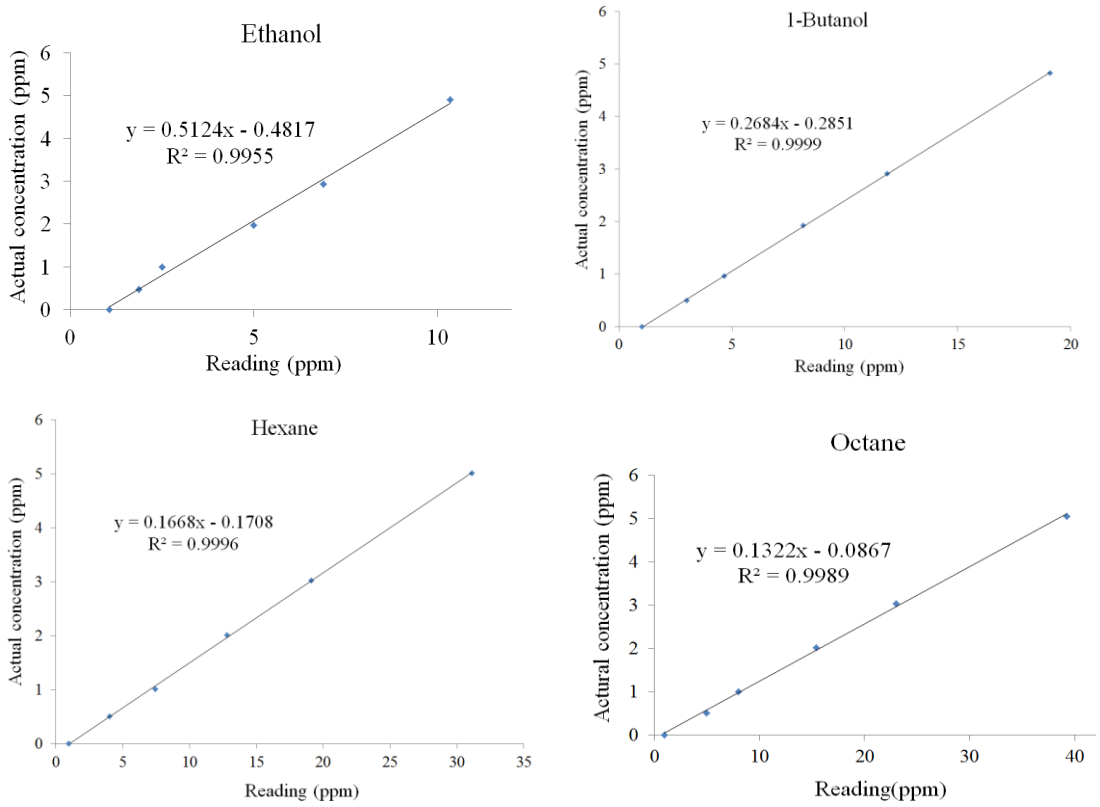

Figure A-2 INNOVA calibration curves for each compound

APPENDIX B: Determination of Aldehydes and Ketones in Air by High Performance Liquid Chromatography (HPLC)

B.1 Brief description of the HPLC method:

A pre-determined volume of air is sampled through a 2, 4-dinitro-phenylhydrazine (2, 4-DNPH)-silica cartridge to trap formaldehyde and other carbonyls (aldehydes and ketones), which are converted to the hydrazone derivatives. The derivatives are eluted from the cartridge in acetonitrile and are separated and analyzed by high performance liquid chromatography 6yu(HPLC) with ultraviolet (UV) detection.

B.2 Method Reference:

(1) USEPA compendium of methods for the determination of toxic organic compounds in ambient air, Compendium Method TO-11A "Determination of Formaldehyde in Ambient Air Using Adsorbent Cartridge Followed by High Performance Liquid Chromatography (HPLC)", EPA Document: EPA/625/R-96/010b, January 1999

B.3 Sampling Device:

Supelco LpDNPH S10L cartridge containing chromatographic grade silica coated with 2,4-DNPH.

- Adsorbent: chromatographic grade silica coated with 2,4 DNPH
- Particle size: 150-250µm (60/100 mesh)
- DNPH Loading: 0.29% (1mg/cartridge)
- Bed Weight: approx. 350mg
- Capacity: approx. 75µg total carbonyls

- Cartridge Length: 4.0cm
- Background: HPLC/UV @360nm

  Formaldehyde: 0.01μg/cartridge

  Acetaldehyde: 0.03μg/cartridge

  Acetone: 0.09μg/cartridge

  Other Aldehyde: 0.01μg/cartridge
- Pressure drop: <7kPa at 1.5L/min
- Storage: refrigerate (4°C); protect from light
- Shelf life: 12 months

B.4 Analytical System：

Instrument:

- HPLC system: Perkin Elmer Flexar HPLC
- HPLC column: Brownlee validated micro-bore column, C18, 5μm film thickness, 150 mm x 4.6 mm ID
- Data System: Perkin Elmer Chromera Manager version 2.1.0

Liquid Chromatographic Conditions:

- Mobile Phase (gradient program): 6min 70% acetonitrile/ 30% water

  3min 100% acetonitrile/ 0% water

  4min 70% acetonitrile/ 30% water
- Detector: ultraviolet, operating at 360nm, sampling rate 5pts/sec
- Flow Rate: 1.0 mL/min
- Run Time: 13min

- Injection Volume: 20uL

B.5 HPLC Calibration

The HPLC apparatus was calibrated with TO11/IP-6A aldehyde/ketone-DNPH mixtures, which included formaldehyde, acetaldehyde, acrolein, acetone, propionaldehyde, crotonaldehyde, butyraldehyde, benzaldehyde, isovaldehyde, valdehyde, o-tolualdehyde, m-tolualdehyde, p-tolualdehyde and hexanal with each analytical concentration of around 15 µg/mL. 2%, 5%, 20% and 50% dilute solutions were prepared from stock solution diluted by acetonitrile with corresponding volumes. For various dilute solutions, the injection volume was of 10 µL and 20 µL, respectively. Thus, the calibration was carried out at eight different mass levels: 3, 6, 7.5, 15, 30, 60, 75, and 150 ng. Each calibration standard was analyzed twice, and calibration curves were plotted of average area responses versus different levels of mass injected (Figure B-1).

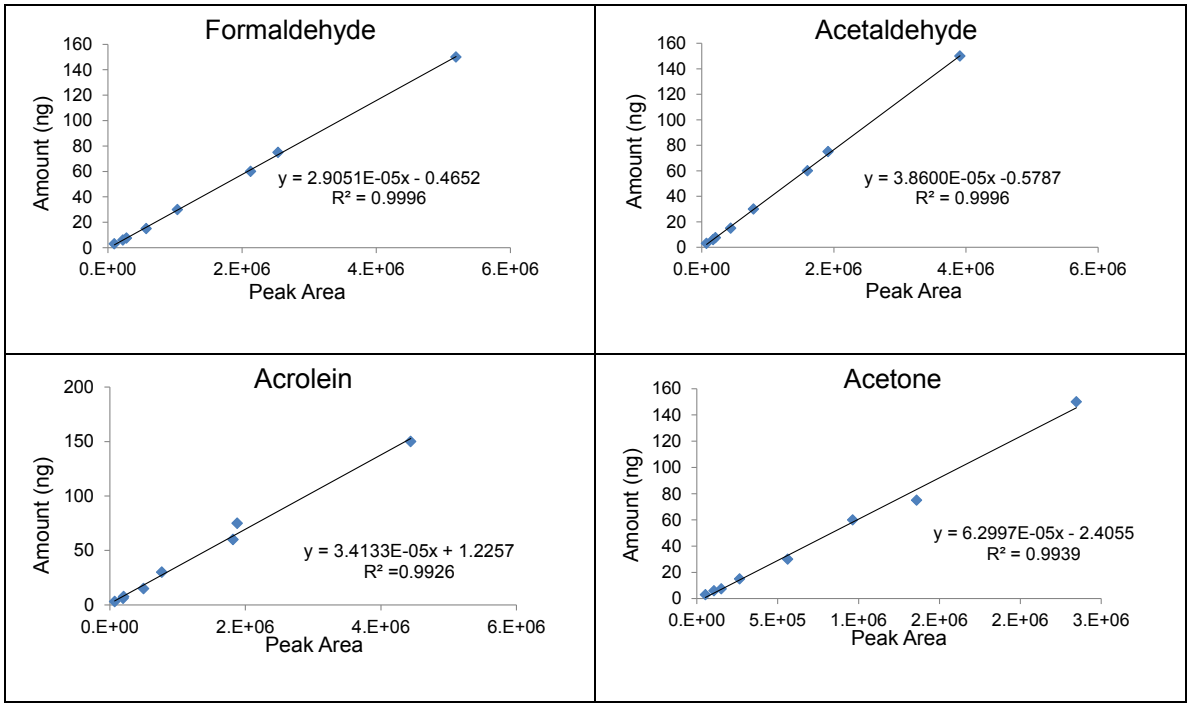

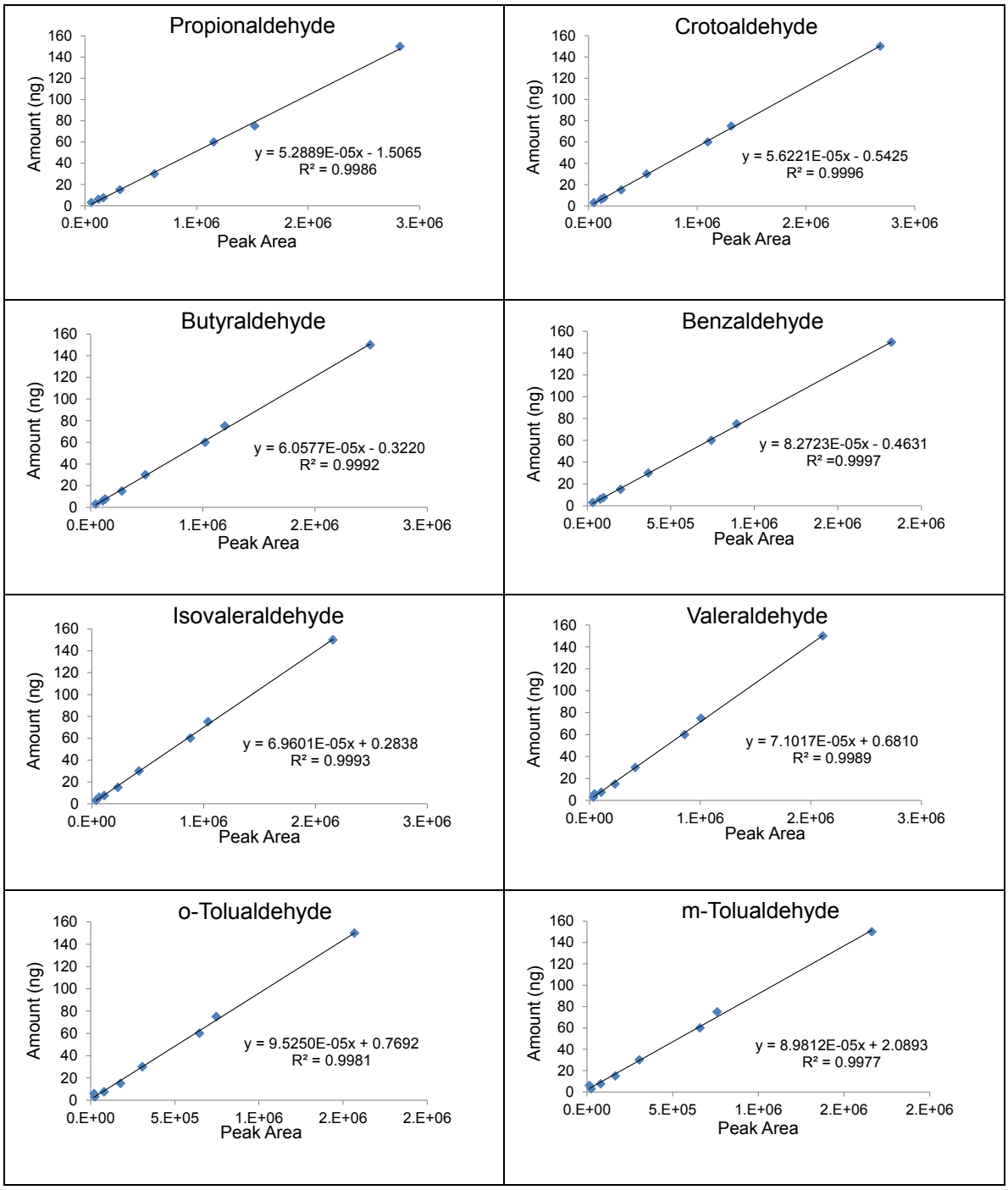
Propionaldehyde
y = 5.2889E-05x - 1.5065
R² = 0.9986
Amount (ng)
Peak Area
Crotoaldehyde
y = 5.6221E-05x - 0.5425
R² = 0.9996
Amount (ng)
Peak Area
Butyraldehyde
y = 6.0577E-05x - 0.3220
R² = 0.9992
Amount (ng)
Peak Area
Benzaldehyde
y = 8.2723E-05x - 0.4631
R² =0.9997
Amount (ng)
Peak Area
Isovaleraldehyde
y = 6.9601E-05x + 0.2838
R² = 0.9993
Amount (ng)
Peak Area
Valeraldehyde
y = 7.1017E-05x + 0.6810
R² = 0.9989
Amount (ng)
Peak Area
o-Tolualdehyde
y = 9.5250E-05x + 0.7692
R² = 0.9981
Amount (ng)
Peak Area
m-Tolualdehyde
y = 8.9812E-05x + 2.0893
R² = 0.9977
Amount (ng)
Peak Area

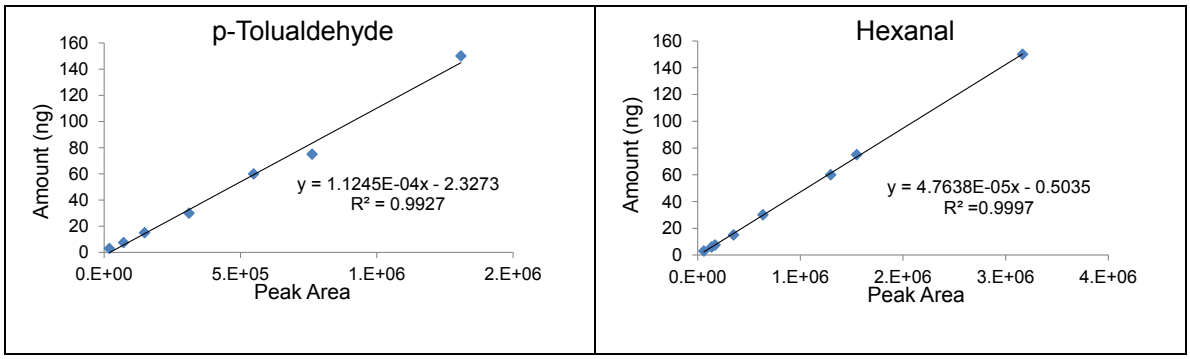

Figure B-1 HPLC calibration curves for formaldehyde, acetaldehyde, acrolein, acetone, propionaldehyde, crotonaldehyde, butyraldehyde, benzaldehyde, isovaldehyde, valdehyde, o-tolualdehyde, m-tolualdehyde, p-tolualdehyde and hexanal